UC Santa Barbara

UC Santa Barbara Electronic Theses and Dissertations

Title

Strain-Relaxed InGaN Buffer Layers for Long Wavelength Nitride Devices

Permalink

https://escholarship.org/uc/item/4413k5gx

Author

Chan, Philip

Publication Date

2022

Peer reviewed|Thesis/dissertation

UNIVERSITY of CALIFORNIA

Santa Barbara

Strain-Relaxed InGaN Buffer Layers for Long Wavelength Nitride Devices

A dissertation submitted in partial satisfaction of the

requirements for the degree of

Doctor of Philosophy

in

Electrical and Computer Engineering

by

Philip R. Chan

Committee in charge:

Shuji Nakamura, Chair

Steven P. DenBaars

Jonathan Klamkin

Stacia Keller

June 2022

The dissertation of Philip R. Chan is approved:

_____

Steven P. DenBaars

_____

Jonathan Klamkin

_____

Stacia Keller

_____

Shuji Nakamura, Chair

June 2022

Acknowledgements

My time at UCSB has undoubtedly changed my life and I have many people to thank for their guidance and support along the way. First and foremost is Professor Shuji Nakamura for giving me the opportunity to research at SSLEEC and for his continued support throughout my PhD. I also have to thank him for the many discussions filled with potential applications for the nitrides and world-changing ideas that always seemed one step away. Thanks to Professor Steven DenBaars for his many helpful suggestions, industry knowledge and MOCVD expertise. Dr. Stacia Keller was always willing to help with a wealth of MOCVD knowledge. Professor Jonathan Klamkin was kind enough to allow me to move things around his lab to try unsuccessfully to measure infrared emission from InN. While not on my committee, Professor Jim Speck always kept me grounded in science. Professor Michael Gordon allowed me use of his lab for both near-infrared and micro-LED measurements.

Next, I have to thank Dr. Daniel Cohen. Dan has been a constant source of knowledge, know-how and a healthy dose of realism. He always had his door open and was a constant advocate for the students.

Dr. Daniel Becerra mentored me and taught me much of what I know about MOCVD growth and processing. Dr. Haojun Zhang was a great office-mate as well as source of help and late-night conversation. Dr. Matthew Wong is an inspiration with his incredible work ethic. I have to especially thank him for his continued support, fabrication expertise and, of course, all the Korean BBQ. Norleakvisoth Lim, Vincent Rienzi and Hsun-Ming

Curriculum Vitæ

Philip R. Chan

Education

2022	Ph.D., Electrical and Computer Engineering University of California, Santa Barbara Shuji Nakamura, SSLEEC
2015	B.S., Electrical and Computer Engineering Rutgers University

Professional Experience

2022-Present	Sr. Process Development Engineer, Kyocera SLD Laser, Santa Barbara, CA
2016-2022	Graduate Student Researcher, University of California, Santa Barbara, Santa Barbara, CA
2015	Graduate Technical Intern, Northrop Grumman Corp., Electronic Systems, Linthicum, MD
2013-2015	Undergraduate Coop/Intern, Wireless Information Network Laboratory, Rutgers University, New Brunswick, NJ
2013	Undergratuate Aresty Research Intern, Integrated Systems & NeuroImaging Laboratory, Rutgers University, Piscataway, NJ

Publications

P. Chan, S. P. DenBaars, and S. Nakamura, "Growth of highly relaxed InGaN pseudo-substrates over full 2-in. wafers," *Appl. Phys. Lett.* 119, 131106 (2021)

P. Chan, V. Rienzi, N. Lim, H.-M. chang, M. J. Gordon, S. P. DenBaars, andS. Nakamura, "Demonstration of relaxed InGaN-based red LEDs grown with high active region temperature," *Appl. Phys. Express* 14, 101002 (2021)

P. Chan, C. E. Reilly, S. Keller, S. P. DenBaars, and S. Nakamura, "Growth by MOCVD and photoluminescence of semipolar (20-2-1) InN quantum dashes," *J. Cryst. Growth* 563, 126093 (2021)

M. S. Wong, **P. Chan**, N. Lim, H. Zhang, R. C. White, J. S. Speck, S. P. DenBaars, and S. Nakamura, "Low Forward Voltage III-Nitride Red Micro-Light-Emitting Diodes on a Strain Relaxed Template with an InGaN Decomposition Layer," *Crystals* 12, 721 (2022)

P. Li, H. Li, M. S. Wong, **P. Chan**, Y. Yang, H. Zhang, M. Iza, J. S. Speck, S. Nakamura, and S. P. DenBaars, "Progress of InGaN-Based Red Micro-Light Emitting Diodes," *Crystals* 12, 541 (2022)

M. S. Wong, N. C. Palmquist, J. Jiang, **P. Chan**, C. Lee, P. Li, J. H. Kang, Y. H. Baek, C. H. Kim, D. A. Cohen, T. Margalith, J. S. Speck, S. Nakamura, and S. P. DenBaars, "Effects of activation method and temperature to III-nitride micro-light-emitting diodes with tunnel junction contacts grown by metalorganic chemical vapor deposition," *Appl. Phys. Lett.* 119, 202102 (2021)

H. Zhang, D. A. Cohen, **P. Chan**, M. S. Wong, P. Li, H. Li, S. Nakamura, and S. P. DenBaars, "High performance of a semipolar InGaN laser with a phase-shifted embedded hydrogen silsesquioxane (HSQ) grating," *Opt. Lett.* 45, 5844 (2020)

H. Zhang, D. A. Cohen, **P. Chan**, M. S. Wong, S. Mehari, S. Nakamura, and S. P. DenBaars, "Semipolar group III-nitride distributed-feedback blue laser diode with indium tin oxide surface grating," *Proc. SPIE 11301*, Novel In-Plane Semiconductor Lasers XIX, 1130102 (2020)

G. Lheureux, S. Mehari, D. Cohen, **P. Chan**, H. Zhang, S. Hamdy, C. Reilly, R. Anderson, E. Zeitz, R. Seshadri, T. Margalith, C. Weisbuch, J. Speck, S. DenBaars, and S. Nakamura, "GaN High-Power Lasers for solid-state lighting," *OSA Advanced Photonics Congress 2019*, paper PT2C.1

H. Zhang, D. A. Cohen, **P. Chan**, M. S. Wong, S. Mehari, D. L. Becerra, S. Nakamura, and S. P. DenBaars, "Continuous-wave operation of a semipolar InGaN distributed-feedback blue laser diode with a first-order indium tin oxide surface grating," *Opt. Lett.* 44, 3106 (2019)

S. W. Hamdy, T. Hirokawa, **P. Chan**, W. Jin, V. M. Rosborough, E. J. Stanton, A. M. Netherton, M. Garza, W. Ibsen, D. D. John, J. E. Bowers, "Light-based educational outreach activities for pre-university students," *ETOP 2019* paper 11143_71 (2019)

Patents and pending applications

N. Palmquist, **P. Chan**, and S. Nakamura, "III-Nitride Based Tunnel Junction with P-Type Superlattice,", UC 2022-777-1 (2022)

P. Chan, M. S. Wong, and S. Nakamura, "Method to Improve the Performance of III-Nitride Tunnel Junctions,", UC 2022-779-1 (2022)

P. Chan, S. P. DenBaars, and S. Nakamura, "III-Nitride-Based High Efficiency and High-Power Devices Grown on or Above a Strain Relaxed Template,", U.S. Provisional Application Serial No. 63/305,441, UC 2022-755-1 (2022)

P. Chan, S. P. DenBaars, and S. Nakamura, "III-Nitride Based Devices Grown on a Thin Template on Thermally Decomposed Material,", U.S. Provisional Application Serial No. 63/186,749, UC 2021-888-1 (2021)

P. Chan, S. P. DenBaars, and S. Nakamura, "III-Nitride Based Devices Grown on a Thin Template on Thermally Decomposed Material,", U.S. Provisional Application Serial No. 63/230,205, UC 2021-888-2 (2021)

N. Lim, **P. Chan**, S. P. DenBaars, M. J. Gordon, and S. Nakamura, "III-Nitride-Based Device Grown with a Relaxed Active Region,", U.S. Provisional Application Serial No. 63/240,517, UC 2021-760-1 (2021)

P. Chan, S. P. DenBaars, and S. Nakamura, "Improvement of Surface Morphology of III-Nitride-Based Devices Grown on or Above a Strain Compliant Template,", U.S. Provisional Application Serial No. 63/245,105, UC 2021-763-1 (2021)

Abstract

Strain-Relaxed InGaN Buffer Layers for Long Wavelength Nitride Devices

by

Philip R. Chan

The InGaN material system spans from the ultraviolet (363 nm) to the near infrared (1.8 μm). It has found tremendous success in solid state lighting, leading to huge improvements in both lifetime and efficiencies of white light sources. InGaN-based light sources can be found in most households, automobiles and displays today. However, these successes are mostly limited to low In-fraction devices emitting in the violet and blue wavelengths. This dissertation focuses on long wavelength InGaN devices emitting in the red, far-red and near infrared.

Because of the large lattice mismatch between InN and GaN, high composition InGaN necessary for long wavelength devices is highly strained when grown on a GaN template. A novel method of biaxially strain-relaxing an InGaN buffer across a planar substrate is demonstrated by leveraging the temperature sensitivity of high composition InGaN layers. The thermal decomposition of an InGaN underlayer to form voids is shown to relax an InGaN buffer across the entire substrate. Quantum wells grown on these buffers show red-shifted emission and a decrease in the strain-state of the active region. We then optimize the growth conditions of the relaxed InGaN buffers to demonstrate smooth,

highly relaxed InGaN in a single MOCVD growth.

Next, we demonstrate devices on the strain-relaxed buffers that compare favorably with those using other relaxation methods. The devices show remarkably low forward voltage and high growth temperature compared to conventionally grown counterparts. Using this relaxation method, far-red LEDs emitting over $750\,\mathrm{nm}$ are achievable. We show red $5 \times 5\ \mathrm{\mu m^2}$ micro-LEDs emitting at $640\,\mathrm{nm}$ with $> 0.45\%$ EQE measured on-wafer.

Finally, we explore growth of InN quantum dots on semipolar $(2\,0\,\overline{2}\,\overline{1})$ and $(2\,0\,\overline{2}\,1)$ substrates, two orientations previously unexplored in InN or In-rich InGaN. We map out growth parameters and characterize the crystal growth on the two planes, demonstrating room temperature photoluminescence in the $1300\,\mathrm{nm}$ range. An unconventional p-down device structure is proposed and progress is shown towards a first electrically-injected InN LED with photoluminescence shown from a full device. Key challenges are identified, namely the temperature sensitivity of InN and poor crystal quality from the resulting low temperature growth.

Contents

Chapter 1

Introduction

The III-nitride material system, including GaN and it's In- and Al- ternaries and qua-
ternaries, has had far-reaching impacts on the world. In the early 1990s, Professor Shuji
Nakamura set out to develop the III-nitride system, a potential competitor to ZnSe blue
emitters. ZnSe, a II-VI semiconductor, was a more mature material system with blue
light emitting diodes (LEDs) demonstrated in 1985 by Nishizawa et al. [1] and first blue-
green laser diodes (LDs) demonstrated in 1991 by Haase et al.[2] Because of it's 14%
lattice mismatch with the sapphire substrates, GaN at the time suffered from extremely
poor crystal quality. In contrast, ZnSe was grown coherently with GaAs with just a 3%
lattice mismatch leading to high quality crystals. ZnSe devices, however, showed very
short lifetimes due to the formation of dark line defects.[3]

Nakamura quickly made his fundamental contributions to the field, bringing the III-
nitrides to the forefront. These contributions included the growth of a high quality

GaN buffer layer by metalorganic chemical vapor deposition (MOCVD) in 1991[4], the understanding of Mg-doped p-GaN compensation and use of a thermal anneal to activate it in 1992 [5], and the growth of high quality InGaN/GaN superlattices in 1993.[6] In 1994, InGaN LEDs achieved the brightest blue emission yet, with a one candela luminous intensity.[7] By 1996, InGaN LDs were achieved. [8]

Today, InGaN LEDs are ubiquitous and present in most household lighting and displays.

1.1 LED fundamentals

LEDs consist of a semiconductor p-n junction. The p-type material is a source of positively-charged holes and the n-type is a source of high-energy negatively-charged electrons. These carriers recombine in the active region to spontaneously emit light with a wavelength dependent on the bandgap of the active region material. The efficiency with which carriers are converted into light is called the *internal quantum efficiency* (IQE).

The emitted photon can then either travel outside of the LED where it is considered "useful," or it may get trapped in the LED by reflection and reabsorbed. The fraction of emitted light that makes it outside of the LED is called the *light extraction efficiency* (LEE). Together, the product of the IQE and LEE is referred to as the *external quantum efficiency* (EQE) of the LED and is considered a key metric. EQE will be used throughout this dissertation to evaluate devices. Finally, factoring in extra voltage applied to the device over the photon energy yields the *wall plug efficiency* (WPE) which is a complete
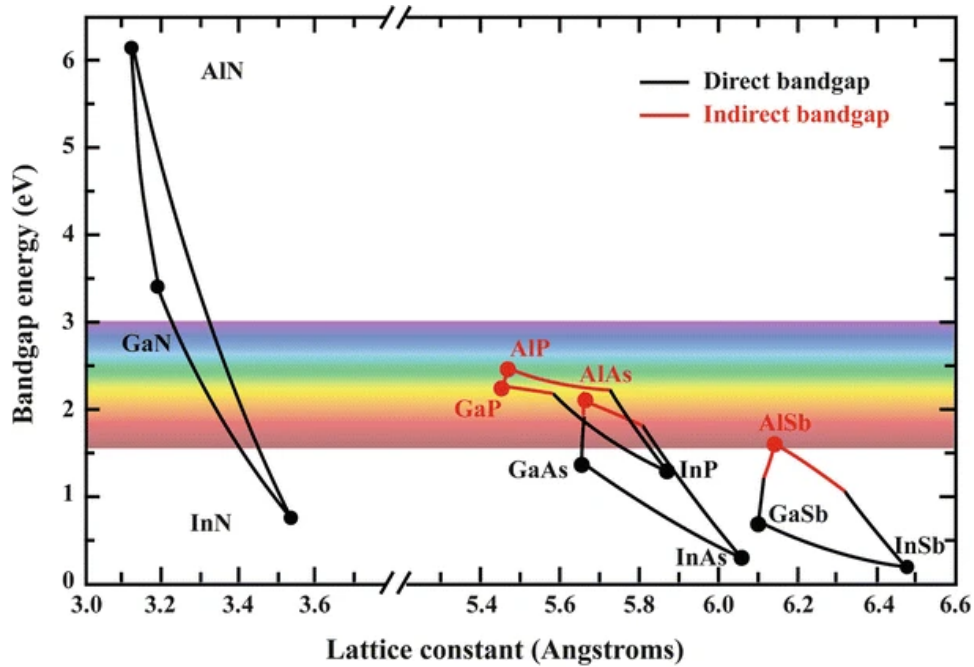
Figure 1.1: Band gap energy versus lattice constant of several III-V material systems. Reproduced with permission from Zhu et al. [9]

measure of LED efficiency.

In the case of III-nitride LEDs, the p- and n-type materials are typically GaN with the active region being $In_xGa_{1-x}N$. As seen in figure 1.1, the bandgap of the InGaN material system spans the visible spectrum of light. Because the wavelength is tuned by the bandgap of the active region, the wavelength of III-nitride LEDs can theoretically be shifted from the ultraviolet (corresponding with $x = 0$) to the near-infrared (corresponding with $x = 1$).

In practice, only violet, blue and, to a lesser extent, green LEDs show high efficiencies. This is partly due to the large lattice mismatch between GaN and InN, shown in figure 1.1 by the x-axis separation of the two points. Growing the active region on a relaxed InGaN buffer, rather than coherent to the GaN template, can help alleviate this lattice

mismatch. This technique will be discussed in more detail in chapter 2.

The addition of optical feedback into the device can stimulate coherent emission. In a Fabry-Perot laser, this feedback is from mirrors at either end of a length of semiconductor called the cavity. With feedback, some of the spontaneous emission from the device couples to the cavity and is amplified by stimulated emission to provide gain that overcomes the cavity losses.

1.2 InGaN device applications

Because InGaN-based devices emit in the visible spectrum, they enjoy a broad range of applications.

1.2.1 Solid state lighting

Efficient LEDs emitting at the short end of the visible spectrum, in violet and blue, enable energy efficient solid state lighting. These white light sources most commonly use LEDs emitting in blue along with a ceramic phosphor that down-converts a portion of the blue light to broad-band yellow emission. With commercial violet and blue LED wall plug efficiencies into the 80% range,[10] solid-state white light sources are able to achieve luminous efficacies over $250\,\mathrm{lm\,W^{-1}}$.[11], [12] This number is almost $3\times$ the luminous efficacy of compact fluorescent (around $90\,\mathrm{lm\,W^{-1}}$) and about $17\times$ that of incandescent lighting (around $15\,\mathrm{lm\,W^{-1}}$).

In 2015, 17% of the United States' total electricity usage went towards lighting. With

just 8% of lighting in the U.S. being LED-based at that time, the potential for energy saving is enormous.[13] With increased adoption of LED lighting, the U.S. saved an estimated 185 terawatt-hours of energy in 2020 from the use of LED lighting, corresponding to about 80 million metric tons of CO_2 emission.[14]

1.2.2 Display technologies

The current standard display technologies are liquid crystal display (LCD) and organic LED (OLED). LCDs work by controlling the polarization state of the backlight. Emission from the backlight is first passed through a polarization filter to obtain a single polarization. The polarized light is then passed through an array of color filters to produce red, green and blue pixels. The liquid crystal pixels can be switched to change the polarization of the light. A second, orthogonal polarization filter either rejects light from a pixel in the "off" state or passes light from a pixel in the "on" state based on polarization. LCDs start with a highly efficient LED backlight which then undergoes several stages of inefficient filtering, including two polarizers and a color filter.

OLED displays are self-emissive meaning each pixel is its own light source. Therefore, they do not need a backlight or color filtering as in the LCD. The OLEDs themselves are quite inefficient and have problems with lifetime and burn-in.[15] While the OLEDs are less efficient, they do not undergo the subtractive filtering of LCDs and can therefore achieve about $2\times$ the efficiency.

One of the most compelling applications for long-wavelength InGaN devices lies in

next-generation displays. As the demand for thin, high density, high brightness displays for cellphones and augmented/virtual reality increases, new display architectures are explored. One such next-generation display makes use of inorganic micro-LEDs. By keeping the self-emissive architecture of the OLED display and using efficient inorganic LEDs, high efficiency, brightness and density displays can be achieved.

While the blue and likely the green LEDs will be InGaN-based, red InGaN LEDs remain challenging and have a high efficiency competitor in the AlGaInP material system. AlGaInP red LEDs have been demonstrated with EQEs over 40%, about 10$\times$ more efficient than InGaN red LEDs.[16], [17]

Because high pixel density is critical for near-eye displays, the LEDs must be made very small, typically on the order of 1×1 µm^2. Compared to AlGaInP, InGaN has a much smaller surface recombination velocity and shows less size dependence. Blue InGaN micro-LEDs have shown size-independent efficiency down to 10×10 µm^2 [18] while green micro-LEDs have shown size-independent efficiency down to just a 1 µm radius.[19]

1.2.3   Near-infrared

In 2001, indium nitride had it's bandgap energy revised 1.97 eV to 0.7 eV, shifting its band-edge emission from about 630 nm in the red all the way to almost 1800 nm in the near-infrared. This large shift in the recognized bandgap energy for InN opened up many potential applications for the nitrides.

First, the InGaN system almost perfectly spans the solar spectrum, from near-infrared

to ultraviolet. Because of this and its inherent radiation hardness, it makes an attractive material for solar cells.[20], [21]

The application of near-infrared nitrides that has garnered the most attention are fast photodetectors. InN photodetectors are promising because of the material's measured low electron effective mass, high mobility and high drift velocities. Additionally, high absorption coefficients promise high photoresponsitivity. While there is a significant body of work towards efficient, fast InN detectors, they lag conventional InGaAs detectors significantly due to issues with MOCVD growth of InN in a p-i-n structure as discussed in chapter 5.[22]–[25]

Finally, electrically-injected In-rich InGaN or InN emitters have potential applications in telecommunications. If the InN is embedded in a GaN matrix, the wide-bandgap barriers could provide a higher degree of temperature stability than conventional narrow-bandgap III-Vs. While optically pumped lasing of InN has been demonstrated,[26] electrically-injected InN-based emitters have remained out of reach.

1.3 Contributions of this dissertation

This dissertation focuses on LEDs emitting in the red and near-infrared.

A novel method to grow a strain-relaxed InGaN buffer layer by MOCVD in a single growth is proposed and demonstrated. Relaxed InGaN buffers, discussed in detail in chapter 2, are used to reduce the strain in the active region of a device, leading to higher quality crystal growth. Highly strain-relaxed buffers over full, planar substrates

Authors	Report	λ (nm)	Peak EQE (%)	Device size (µm²)	V_F at 50 A cm^{-2}	Relaxed InGaN	a (Å)
Chan et al.	–	643	0.46 (W)	5×5	4.1	Yes*	3.211
Chan et al.	–	643	0.31 (W)	10×10	3.0	Yes*	3.211
Wong et al.	2022[28]	637	0.25 (P)	20×20	2.2	Yes*	3.211
Chan et al.	2021[29]	633	0.05 (W)	10^5	2.6	Yes*	3.213
Pasayat et al.	2021[27]	632	0.2 (W)	6×6	3.5	Yes†	3.197
White et al.	2021[30]	610	0.83 (P)	80×80	3.8	Yes‡	3.205
Dussaigne et al.	2021[31]	625	0.14 (W)	25π	6.8	Yes‡	3.205
Dussaigne et al.	2020[32]	616	0.09 (W)	50×50	–	Yes‡	3.207

(W) EQE measured on wafer

(P) EQE measured from packaged LED

* Buffer relaxed using decomposition layer

† Buffer relaxed using a nanoporous layer

‡ Device grown on Soitec InGaNOS substrate

Table 1.1: Reports presented here and other recent reports of red InGaN-based LEDs on relaxed InGaN buffers.

are demonstrated, characterized and optimized. A 70% biaxially relaxed $In_{0.046}Ga_{0.954}N$ buffer layer with under 2 nm RMS roughness is achieved.

Next, red devices are demonstrated on these relaxed buffer layers. Red micro-LEDs show superior peak EQE and longer wavelength than those achieved with other relaxed InGaN methods. A peak EQE of 0.46% was shown with an on-wafer measurement and without the use of an omni-directional reflector. Packaging and adding a dielectric reflector under the pad metal is expected to increase the peak EQE significantly, at least a factor of 3x.[27] Additionally, the forward voltage of devices using this method are strikingly low. Results are tabulated on table 1.1 in comparison with recent reports of red LEDs on relaxed InGaN buffers.

Finally, we move past red and explore InN quantum dot growth on semipolar $(2\,0\,\bar{2}\,\bar{1})$ and $(2\,0\,\bar{2}\,1)$ planes. We characterize the InN growth, demonstrate room temperature

near-infrared photoluminescence and propose a structure for an electrically-injected InN-based device. While no emission is seen from the electrically-injected device, progress is made towards an emitter and key challenges are identified.

References

[1] J.-i. Nishizawa, K. Itoh, Y. Okuno, and F. Sakurai, "Blue light emission from znse p-n junctions," *J. Appl. Phys.*, vol. 57, no. 6, pp. 2210–2216, 1985. DOI: `10.1063/1.334364`.

[2] M. A. Haase, J. Qiu, J. M. DePuydt, and H. Cheng, "Blue-green laser diodes," *Appl. Phys. Lett.*, vol. 59, no. 11, pp. 1272–1274, 1991. DOI: `10.1063/1.105472`.

[3] T. Matsuoka, A. Ohki, T. Ohno, and Y. Kawaguchi, "Comparison of gan- and znse-based materials for light emitters," *J. Cryst. Growth*, vol. 138, no. 1, pp. 727–736, 1994. DOI: `https://doi.org/10.1016/0022-0248(94)90898-2`.

[4] S. Nakamura, "Gan growth using gan buffer layer," *Jpn. J. Appl. Phys.*, vol. 30, no. Part 2, No. 10A, pp. L1705–L1707, 1991. DOI: `10.1143/jjap.30.l1705`.

[5] S. Nakamura, T. Mukai, M. Senoh, and N. Iwasa, "Thermal annealing effects on p-type mg-doped GaN films," *Jpn. J. Appl. Phys.*, vol. 31, no. Part 2, No. 2B, pp. L139–L142, 1992. DOI: `10.1143/jjap.31.l139`.

[6] S. Nakamura, T. Mukai, M. Senoh, S.-i. Nagahama, and N. Iwasa, "Inxga(1-x)n/inyga(1-y)n superlattices grown on gan films," *J. Appl. Phys.*, vol. 74, no. 6, pp. 3911–3915, 1993. DOI: `10.1063/1.354486`.

[7] S. Nakamura, T. Mukai, and M. Senoh, "Candela-class high-brightness ingan/algan double-heterostructure blue-light-emitting diodes," *Appl. Phys. Lett.*, vol. 64, no. 13, pp. 1687–1689, 1994. DOI: `10.1063/1.111832`.

[8] S. Nakamura, M. Senoh, S.-i. Nagahama, N. Iwasa, T. Yamada, T. Matsushita, H. Kiyoku, and Y. Sugimoto, "InGaN-based multi-quantum-well-structure laser diodes," *Jpn. J. Appl. Phys.*, vol. 35, no. Part 2, No. 1B, pp. L74–L76, 1996. DOI: `10.1143/jjap.35.l74`.

[9] D. Zhu and C. J. Humphreys, "Solid-state lighting based on light emitting diode technology," in *Optics in Our Time*, M. D. Al-Amri, M. El-Gomati, and M. S. Zubairy, Eds. Cham: Springer International Publishing, 2016, pp. 87–118, ISBN: 978-3-319-31903-2. DOI: `10.1007/978-3-319-31903-2_5`.

[10] C. A. Hurni, A. David, M. J. Cich, R. I. Aldaz, B. Ellis, K. Huang, A. Tyagi, R. A. DeLille, M. D. Craven, F. M. Steranka, and M. R. Krames, "Bulk gan flip-chip violet light-emitting diodes with optimized efficiency for high-power operation," *Appl. Phys. Lett.*, vol. 106, no. 3, p. 031 101, 2015. DOI: `10.1063/1.4905873`.

[11] D. Feezell and S. Nakamura, "Invention, development, and status of the blue light-emitting diode, the enabler of solid-state lighting," *C R Phys.*, vol. 19, no. 3, pp. 113–133, 2018. DOI: `https://doi.org/10.1016/j.crhy.2017.12.001`.

[12] Y. Narukawa, M. Ichikawa, D. Sanga, M. Sano, and T. Mukai, "White light emitting diodes with super-high luminous efficacy," *J. Phys. D: Appl. Phys.*, vol. 43, no. 35, p. 354 002, 2010. DOI: `10.1088/0022-3727/43/35/354002`.

[13] N. Buccitelli, C. Elliott, S. Schober, and M. Yamada, "2015 u.s. lighting market characterization," U.S. Department of Energy, 2015. [Online]. Available: `https://www.energy.gov/eere/ssl/2015-us-lighting-market-characterization`.

[14]   M. Pattison, M. Hansen, N. Bardsley, G. Thomson, K. Gordon, A. Wilkerson, K. Lee, V. Nubbe, and S. Donnely, "2022 solid-state lighting r&d opportunities," U.S. Department of Energy, 2022. [Online]. Available: https://www.energy.gov/eere/ssl/articles/doe-publishes-2022-solid-state-lighting-rd-opportunities.

[15]   S. Sudheendran Swayamprabha, D. K. Dubey, Shahnawaz, R. A. K. Yadav, M. R. Nagar, A. Sharma, F. C. Tung, and J. H. Jou, "Approaches for Long Lifetime Organic Light Emitting Diodes," *Adv. Sci.*, vol. 8, no. 1, pp. 1–29, 2021. DOI: 10.1002/advs.202002254.

[16]   W. C. Cheng, S. Y. Huang, Y. J. Chen, C. S. Wang, H. Y. Lin, T. M. Wu, and R. H. Horng, "AlGaInP Red LEDs with Hollow Hemispherical Polystyrene Arrays," *Sci. Rep.*, vol. 8, no. 1, pp. 4–10, 2018. DOI: 10.1038/s41598-018-19405-y.

[17]   P. Li, H. Li, H. Zhang, Y. Yang, M. S. Wong, C. Lynsky, M. Iza, M. J. Gordon, J. S. Speck, S. Nakamura, and S. P. DenBaars, " Red InGaN micro-light-emitting diodes (>620 nm) with a peak external quantum efficiency of 4.5% using an epitaxial tunnel junction contact," *Appl. Phys. Lett.*, vol. 120, no. 12, p. 121 102, 2022. DOI: 10.1063/5.0086912.

[18]   M. S. Wong, C. Lee, D. J. Myers, D. Hwang, J. A. Kearns, T. Li, J. S. Speck, S. Nakamura, and S. P. Denbaars, "Size-independent peak efficiency of III-nitride micro-light-emitting-diodes using chemical treatment and sidewall passivation,"

Appl. Phys. Express, vol. 12, no. 9, p. 097 004, 2019. DOI: `10.7567/1882-0786/ab3949`.

[19] J. M. Smith, R. Ley, M. S. Wong, Y. H. Baek, J. H. Kang, C. H. Kim, M. J. Gordon, S. Nakamura, J. S. Speck, and S. P. Denbaars, "Comparison of size-dependent characteristics of blue and green InGaN microLEDs down to 1 μ m in diameter," *Appl. Phys. Lett.*, vol. 116, no. 7, p. 071 102, 2020. DOI: `10.1063/1.5144819`.

[20] E. Trybus, G. Namkoong, W. Henderson, S. Burnham, W. A. Doolittle, M. Cheung, and A. Cartwright, "InN: A material with photovoltaic promise and challenges," *J. Cryst. Growth*, vol. 288, no. 2, pp. 218–224, 2006. DOI: `10.1016/j.jcrysgro.2005.12.120`.

[21] J. Wu, W. Walukiewicz, K. M. Yu, W. Shan, J. W. Ager, E. E. Haller, H. Lu, W. J. Schaff, W. K. Metzger, and S. Kurtz, "Superior radiation resistance of In 1-xGa xN alloys: Full-solar-spectrum photovoltaic material system," *J. Appl. Phys.*, vol. 94, no. 10, pp. 6477–6482, 2003. DOI: `10.1063/1.1618353`.

[22] W. J. Lai, S. S. Li, C. C. Lin, C. C. Kuo, C. W. Chen, K. H. Chen, and L. C. Chen, "Near infrared photodetector based on polymer and indium nitride nanorod organic/inorganic hybrids," *Scr. Mater.*, vol. 63, no. 6, pp. 653–656, 2010. DOI: `10.1016/j.scriptamat.2010.05.035`.

[23] S. Krishna, A. Sharma, N. Aggarwal, S. Husale, and G. Gupta, "Ultrafast photoresponse and enhanced photoresponsivity of Indium Nitride based broad band

photodetector," *Sol. Energy Mater. Sol. Cells*, vol. 172, no. April, pp. 376–383, 2017. DOI: `10.1016/j.solmat.2017.08.017`.

[24] L.-H. Hsu, C.-C. Lin, H.-V. Han, D.-W. Lin, Y.-H. Lo, Y.-C. Hwang, and H.-C. Kuo, "Enhanced photocurrent of a nitride–based photodetector with InN dot-like structures," *Opt. Mater. Express*, vol. 4, no. 12, p. 2565, 2014. DOI: `10.1364/ome.4.002565`.

[25] B. Tekcan, S. Alkis, M. Alevli, N. Dietz, B. Ortac, N. Biyikli, and A. K. Okyay, "A near-infrared range photodetector based on indium nitride nanocrystals obtained through laser ablation," *IEEE Electron Device Lett.*, vol. 35, no. 9, pp. 936–938, 2014. DOI: `10.1109/LED.2014.2336795`.

[26] B. A. Andreev, K. E. Kudryavtsev, A. N. Yablonskiy, D. N. Lobanov, P. A. Bushuykin, L. V. Krasilnikova, E. V. Skorokhodov, P. A. Yunin, A. V. Novikov, V. Y. Davydov, and Z. F. Krasilnik, "Towards the indium nitride laser: Obtaining infrared stimulated emission from planar monocrystalline InN structures," *Sci. Rep.*, vol. 8, no. 1, pp. 1–8, 2018. DOI: `10.1038/s41598-018-27911-2`.

[27] S. S. Pasayat, C. Gupta, M. S. Wong, R. Ley, M. J. Gordon, S. P. Denbaars, S. Nakamura, S. Keller, and U. K. Mishra, "Demonstration of ultra-small (<10 μm) 632 nm red InGaN micro-LEDs with useful on-wafer external quantum efficiency (>0.2%) for mini-displays," *Appl. Phys. Express*, vol. 14, no. 1, p. 011 004, 2021. DOI: `10.35848/1882-0786/abd06f`.

[28] M. S. Wong, P. Chan, N. Lim, H. Zhang, R. C. White, J. S. Speck, S. P. Denbaars, and S. Nakamura, "Low Forward Voltage III-Nitride Red Micro-Light-Emitting Decomposition Layer," *Crystals*, pp. 4–9, 2022.

[29] P. Chan, V. Rienzi, N. Lim, H. M. Chang, M. Gordon, S. P. DenBaars, and S. Nakamura, "Demonstration of relaxed InGaN-based red LEDs grown with high active region temperature," *Appl. Phys. Express*, vol. 14, no. 10, pp. 3–7, 2021. DOI: `10.35848/1882-0786/ac251d`.

[30] R. C. White, H. Li, M. Khoury, C. Lynsky, M. Iza, S. Keller, D. Sotta, S. Nakamura, and S. P. DenBaars, "Ingan-based microled devices approaching 1% eqe with red 609 nm electroluminescence on semi-relaxed substrates," *Crystals*, vol. 11, no. 11, 2021. DOI: `10.3390/cryst11111364`.

[31] A. Dussaigne, P. Le Maitre, H. Haas, J. C. Pillet, F. Barbier, A. Grenier, N. Michit, A. Jannaud, R. Templier, D. Vaufrey, F. Rol, O. Ledoux, and D. Sotta, "Full InGaN red (625 nm) micro-LED (10 μm) demonstration on a relaxed pseudo-substrate," *Appl. Phys. Express*, vol. 14, no. 9, 2021. DOI: `10.35848/1882-0786/ac1b3e`.

[32] A. Dussaigne, F. Barbier, B. Damilano, S. Chenot, A. Grenier, A. M. Papon, B. Samuel, B. Ben Bakir, D. Vaufrey, J. C. Pillet, A. Gasse, O. Ledoux, M. Rozhavskaya, and D. Sotta, "Full ingan red light emitting diodes," *J. Appl. Phys.*, vol. 128, no. 13, p. 135 704, 2020. DOI: `10.1063/5.0016217`.

Chapter 2

Relaxed InGaN buffers

As shown in figure 1.1, InN and GaN have a large lattice mismatch of about 10%. This large lattice mismatch leads to high strain in InGaN active regions grown coherent with GaN. As the wavelength of InGaN devices is pushed longer, the indium composition increases, increasing the strain in the active region.

This high strain leads to a degradation in crystal quality during growth from the formation of misfit dislocations.[1], [2] Additionally, the strain leads to a reduction in indium incorporation into the film, a consequence of an effect know as compositional pulling.[3], [4] Initially, when growing InGaN coherent to a larger lattice constant material such as GaN, the InGaN composition remains lower than expected for a given growth condition. As the InGaN layer thickness increases, the composition increases and the morphology and crystal quality degrade.

This effect can prove detrimental to growth of long wavelength active regions. Typi-

cally, a III-nitride LED contains an n-GaN layer with a multiple quantum well (MQW) active region grown coherent to the GaN. During the thin quantum well growth, the strain is high leading to a reduction in initial indium incorporation as defined by compositional pulling. To combat this, the MQW growth conditions must be modified, typically by reducing the growth temperature. This is concerning because a reduction in temperature leads to lower adatom mobilities. This in turn can decrease crystal quality and increase unwanted impurities.[5]

Because of this, it would be beneficial to have a substrate, or pseudosubstrate, that can reduce this lattice mismatch and alleviate strain. This concept is depicted in figure 2.1. Without the use of a relaxed InGaN buffer, the red InGaN QW is grown strained to the GaN template. This results in a high strain indicated by the in-plane lattice constant mismatch of Δa shown in figure 2.1(a). With a relaxed InGaN buffer, the QW is grown coherent to a layer with larger lattice constant than GaN, reducing the strain and lattice constant mismatch as shown in figure 2.1(b). This reduction in strain combats the compositional pulling effect and allows high composition InGaN to be grown hotter than otherwise possible.[6]–[8]

2.1 Alternate substrates

Many methods of creating relaxed InGaN buffer layers have been demonstrated. One way to produce relaxed InGaN is to grow it directly on a compatible substrate with similar lattice constant. The two substrates that have been heavily studied are ZnO and
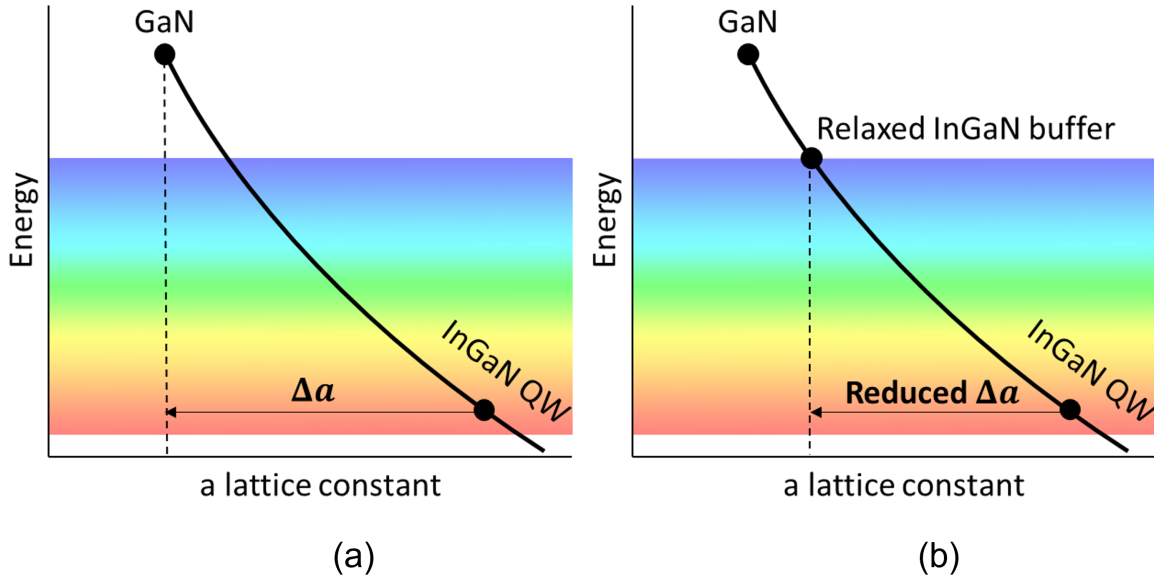
Figure 2.1: Band gap energy versus lattice constant plot of a red InGaN QW grown without (a) and with (b) the use of a relaxed InGaN buffer.

$ScAlMgO_4$.

ZnO has just a 1.9% lattice mismatch with GaN and a 9.3% lattice mismatch with InN. Using Vegard's law, it is lattice matched with $In_{0.18}Ga_{0.82}N$, a composition corresponding with blue emission. While this seems ideal for growth of longer wavelength nitrides, ZnO as a substrate has severe drawbacks.

The primary issue is the poor thermal stability of ZnO. Typically, oxide materials are flattened and smoothed with a high temperature anneal which cannot be done with ZnO. Secondly, MOCVD growth of GaN and InGaN are typically done at relatively high temperatures, which leads to a thick, poor quality interface layer of Ga_2ZnO_4. Both issues were overcome by Kobayashi et al.[9] First, the substrate was flattened and smoothed with an anneal in a ZnO-lined box to suppress sublimation. Second, the relaxed

In$_{0.25}$Ga$_{0.75}$N buffer layer was grown using a room temperature pulsed laser deposition technique, rather than the more traditional MOCVD.

Some success has been found growing films and LEDs by MOCVD using a low temperature GaN buffer layer to prevent Zn and O diffusion into the n-GaN.[10], [11] However, diffusion remains a constant issue that leads to cracks, pinholes and defects in the epitaxial growth.

Similarly to ZnO, ScAlMgO$_4$ is lattice matched to In$_{0.17}$Ga$_{0.83}$N. ScAlMgO$_4$ shows good lattice matching as well as thermal stability. Additionally, it matches the coefficient of thermal expansion with GaN very closely. Because of this, it is a promising path forward, but both crystal and device quality lag conventional growth on sapphire significantly. [12], [13]

2.2 Growth over patterned substrates

One method to obtain a larger lattice constant is through etched nanoscale features. Keller et al. reported partially relaxed In$_{0.1}$Ga$_{0.9}$N layers exhibiting strong photoluminescence using this technique.[14] In this report, nanostripes were patterned and etched into an InGaN/GaN superlattice to obtain partial, uniaxially, elastic relaxation of the superlattice. These features were then overgrown with a 7 nm GaN capping layer and 250 nm of In$_{0.1}$Ga$_{0.9}$N.

While uniaxial relaxation was demonstrated by Keller et al., this structure can be further extended to mesas to obtain biaxial relaxation. However, significant processing
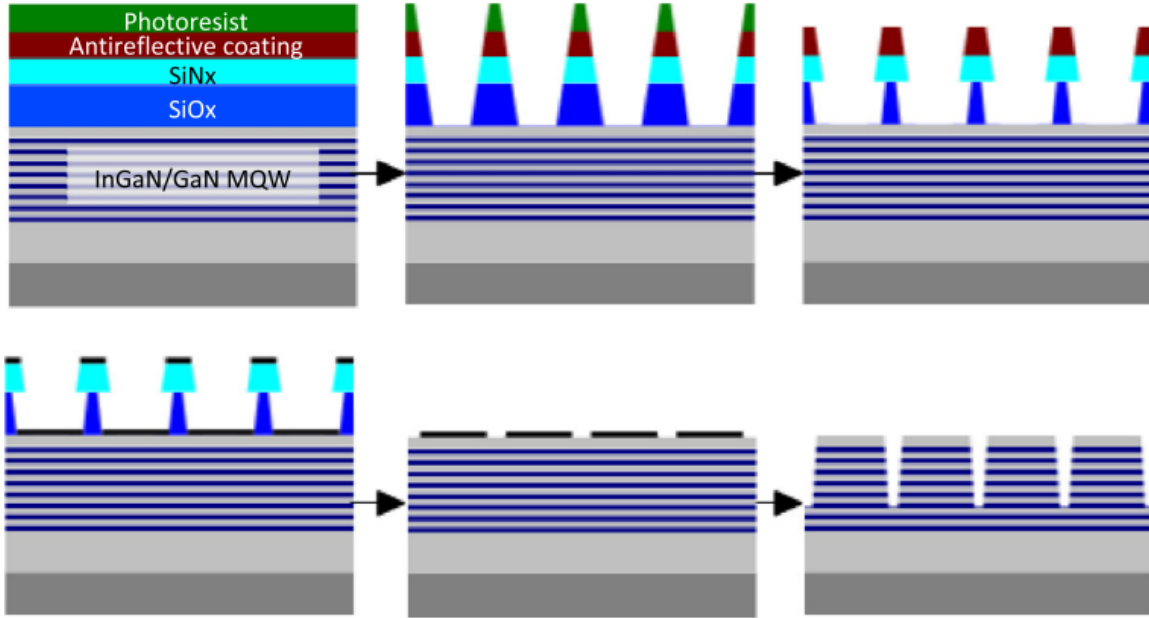
Figure 2.2: Schematic process flow for nanostripe array fabrication. Reproduced from Keller et al. with permission.[14]

is required to achieve this relaxation. The stripes used by Keller et al. were 180-200 nm in width in order to achieve relaxation, and had to be defined holographically. This lithography required a bottom antireflective coating be used. Additionally, to achieve narrow etched trenches to overgrow, a bi-layer lift-off with SiO_x and SiN_x was used to define a Ni hard mask. This process is shown in figure 2.2.

2.2.1 Nanoporous GaN

The same concept can be scaled to larger mesa or stripe sizes by reducing the mechanical stiffness of the material. This was demonstrated by Pasayat et al. using an electrochemical etch to porosify a GaN underlayer.[8], [15], [16] In this process, first, 800 nm of n-type GaN was grown and capped with 200 nm of uid-$In_{0.08}Ga_{0.92}N$. Next, 10×10 µm^2 mesas

were etched and porosified using a doping-selective electrochemical etch to reduce the mechanical stiffness. After porosification, the InGaN layers showed 45% biaxial relaxation. Quantum wells regrown on this material showed a 45 nm red-shift when compared to a co-loaded planar reference.[15] This red-shifting of emission was attributed to a reduction in strain in the active region. As discussed previously, the reduced strain allows for higher initial indium uptake during the thin QW growth.

Later, Pasayat et al. extended the use of this method to red micro-LEDs.[8] The relaxation structure was similar, but the capping layer was GaN rather than InGaN in order to maintain good morphology. After the mesas were porosified, an all-InGaN LED structure was grown with n- and p-$In_{0.04}Ga_{0.96}N$. These layers were shown by high resolution x-ray diffraction (HRXRD) reciprocal space map (RSM) to be 56% relaxed. The structure and RSM are shown in figure 2.3

Fabricated 6×6 µm^2 micro-LEDs showed a 56 nm red-shift as compared to an non-porous reference. The peak EQE as measured on-wafer was 0.2% at a wavelength of 632 nm.

While the device results are impressive, this method has similar shortcomings to that reported by Keller et al. Extensive pre-processing is required to obtain relaxation. Additionally, the relaxed mesas are on the order of 10×10 µm^2, reducing the useable area of the substrate and restricting the use of the technique to micro-LEDs.
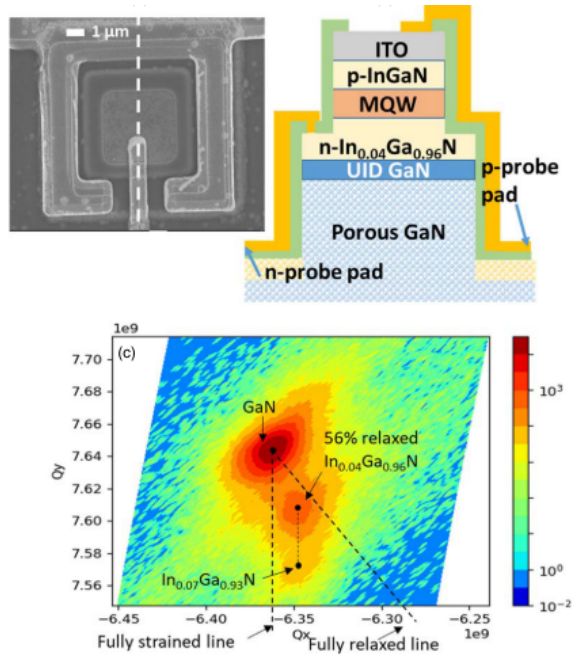
Figure 2.3: The top-view SEM image of the red micro-LED with porous underlayers (top-left), the cross-sectional schematic of the device (top-right) and the HRXRD RSM arround the $(\bar{1}\,\bar{1}\,2\,4)$ peak (bottom). Reproduced from Pasayat et al. with permission.[8]

2.3 InGaNOS

Soitec has produced an InGaN pseudo-substrate, referred to as InGaNOS. This product leverages their Smart Cut^{TM} technology to relax an InGaN layer by film transfer, patterning and annealing. Smart Cut^{TM} is a method by which a film on a donor wafer is hydrogen implanted, bonded to a secondary substrate by SiO_2-SiO_2 bonding, and then removed from the original donor along the implantation by a thermal anneal.

While the details remain proprietary, an InGaN layer is first grown on a GaN template on a sapphire substrate. The InGaN layer is then transferred to a second substrate using the Smart Cut^{TM} method. The InGaN layer is then patterned and etched into mesas of 500×500 or 800×800 µm^2 and then relaxed by a thermal treatment. Finally, the layers

are transferred once more to expose the Ga-polar surface. InGaNOS was produced in three different in-plane lattice constants: 3.190, 3.200, and 3.205 Å.[6]

Producing these pseudo-substrates is a complicated process including two implants, wafer bonds and substrate removals along with patterning, etching and thermal treatments. Additionally, according to a report from White et al., the resulting films show surface undulations up to 60 nm in height and an abundance of point defects leading to an $(0\,0\,2)$ x-ray rocking curve FWHM of 2600 arcsec.[17] In order to achieve bright devices, White et al. buried the interface with nearly 3 µm (135 periods) of lattice-matched $In_{0.04}Ga_{0.96}N$ with GaN interlayers grown at high temperature.[17], [18] This leads to extremely long growth times as well as risk – such a thick InGaN layer must be well calibrated to the pseudo-substrate or risk cracking or dislocation formation.

Using InGaNOS substrates, Dussaigne et al. reported 25π µm^2 micro-LEDs emitting at 625 nm with 0.14% EQE measured on-wafer. White et al. reported packaged 80×80 µm^2 micro-LEDs with 0.83% EQE emitting at 610 nm.

2.4 Other techniques

The previous sections were not comprehensive – other techniques for relaxed InGaN emitters exist in literature. These include growing a thick, compositionally graded layer by MBE to obtain smooth, plastically relaxed InGaN by dislocation formation.[19] Ohkawa et al. showed plastic strain relaxation of an active region by growing 16x MQW and a corresponding red-shift in emission.[20]

Elastic relaxation can also be achieved by nanopillar formation. These are either selectively grown using a mask during molecular beam epitaxy (MBE) or MOCVD growth[21] or are etched into planar epitaxial layers.[22] By using the pillar diameter to control the strain state of the InGaN active region, the wavelength of devices can be tuned from blue to red with the same epitaxial layers. While highly attractive for display applications, this comes at the cost of growth and fabrication complexity as well as emission uniformity. Recent reports of nanopillar-based micro-LED displays show FWHMs of more than 70 nm for the blue pixels and more than 100 nm for the red pixels.[23]

2.5   Chapter summary

In this chapter, we first motivated the use of relaxed InGaN buffer layers for long wavelength III-nitride devices. We then explored the major literature on relaxed InGaN buffer growth including overgrowth of nanopatterned features, use mechanically flexible nanoporous GaN, Soitec's Smart Cut$^{\text{TM}}$ technology and nanopillars.

References

[1]   J. Matthews and A. Blakeslee, "Defects in epitaxial multilayers: I. misfit disloca-
      tions," *J. Cryst. Growth*, vol. 27, pp. 118–125, 1974. DOI: `https://doi.org/10.`
      `1016/S0022-0248(74)80055-2`.

[2]   D. Holec, P. Costa, M. Kappers, and C. Humphreys, "Critical thickness calculations
      for ingan/gan," *J. Cryst. Growth*, vol. 303, no. 1, pp. 314–317, 2007. DOI: `https:`
      `//doi.org/10.1016/j.jcrysgro.2006.12.054`.

[3]   K. Hiramatsu, Y. Kawaguchi, M. Shimizu, N. Sawaki, T. Zheleva, R. Davis, H.
      Tsuda, W. Taki, N. Kuwano, and K. Oki, "The compositional pulling effect in
      movpe grown ingan on gan and algan and its tem characterization," *MRS Internet
      J. of Nitride Semicond. Res.*, vol. 2, no. 11, 1997.

[4]   S. Pereira, M. R. Correia, E. Pereira, K. P. O'Donnell, C. Trager-Cowan, F. Sweeney,
      and E. Alves, "Compositional pulling effects in ingan/gan layers: A combined
      depth-resolved cathodoluminescence and rutherford backscattering/channeling study,"
      Phys. Rev. B, vol. 64, p. 205 311, 20 2001. DOI: `10.1103/PhysRevB.64.205311`.

[5]   R. A. Oliver, M. J. Kappers, C. J. Humphreys, and G. A. D. Briggs, "Growth
      modes in heteroepitaxy of ingan on gan," *J. Appl. Phys.*, vol. 97, no. 1, p. 013 707,
      2005. DOI: `10.1063/1.1823581`.

[6]   A. Even, G. Laval, O. Ledoux, P. Ferret, D. Sotta, E. Guiot, F. Levy, I. C. Robin,
      and A. Dussaigne, "Enhanced in incorporation in full InGaN heterostructure grown

on relaxed InGaN pseudo-substrate," *Appl. Phys. Lett.*, vol. 110, no. 26, p. 262 103, 2017. DOI: 10.1063/1.4989998.

[7]   P. Chan, V. Rienzi, N. Lim, H. M. Chang, M. Gordon, S. P. DenBaars, and S. Nakamura, "Demonstration of relaxed InGaN-based red LEDs grown with high active region temperature," *Appl. Phys. Express*, vol. 14, no. 10, pp. 3–7, 2021. DOI: 10.35848/1882-0786/ac251d.

[8]   S. S. Pasayat, C. Gupta, M. S. Wong, R. Ley, M. J. Gordon, S. P. Denbaars, S. Nakamura, S. Keller, and U. K. Mishra, "Demonstration of ultra-small ($<$10 μm) 632 nm red InGaN micro-LEDs with useful on-wafer external quantum efficiency ($>$0.2%) for mini-displays," *Appl. Phys. Express*, vol. 14, no. 1, p. 011 004, 2021. DOI: 10.35848/1882-0786/abd06f.

[9]   A. Kobayashi, J. Ohta, and H. Fujioka, "Low temperature epitaxial growth of In0.25Ga0.75N on lattice-matched ZnO by pulsed laser deposition," *J. Appl. Phys.*, vol. 99, no. 12, pp. 1–5, 2006. DOI: 10.1063/1.2206883.

[10] Y. Lei, J. Xu, K. Zhu, M. He, J. Zhou, Y. Gao, L. Zhang, and Y. Chen, "A GaN-based LED with perpendicular structure fabricated on a ZnO substrate by MOCVD," *IEEE/OSA J. Disp. Technol.*, vol. 9, no. 5, pp. 377–381, 2013. DOI: 10.1109/JDT.2012.2236300.

[11] S. J. Wang, N. Li, E. H. Park, Z. C. Feng, A. Valencia, J. Nause, M. Kane, C. Summers, and I. Ferguson, "MOCVD growth of GaN-based materials on ZnO sub-

strates," *Phys. Status Solidi C*, vol. 5, no. 6, pp. 1736–1739, 2008. DOI: `10.1002/pssc.200778614`.

[12] T. Ozaki, Y. Takagi, J. Nishinaka, M. Funato, and Y. Kawakami, "Metalorganic vapor phase epitaxy of GaN and lattice-matched InGaN on ScAlMgO4(0001) substrates," *Appl. Phys. Express*, vol. 7, no. 9, pp. 4–7, 2014. DOI: `10.7567/APEX.7.091001`.

[13] T. Ozaki, M. Funato, and Y. Kawakami, "InGaN-based visible light-emitting diodes on ScAlMgO4(0001) substrates," *Appl. Phys. Express*, vol. 4, no. 0001, 2015.

[14] S. Keller, C. Lund, T. Whyland, Y. Hu, C. Neufeld, S. Chan, S. Wienecke, F. Wu, S. Nakamura, J. S. Speck, S. P. Denbaars, and U. K. Mishra, "InGaN lattice constant engineering via growth on (In,Ga)N/GaN nanostripe arrays," *Semicond. Sci. Technol.*, vol. 30, no. 10, p. 105 020, 2015. DOI: `10.1088/0268-1242/30/10/105020`.

[15] S. S. Pasayat, C. Gupta, D. Acker-James, D. A. Cohen, S. P. Denbaars, S. Nakamura, S. Keller, and U. K. Mishra, "Fabrication of relaxed InGaN pseudo-substrates composed of micron-sized pattern arrays with high fill factors using porous GaN," *Semicond. Sci. Technol.*, vol. 34, no. 11, p. 115 020, 2019. DOI: `10.1088/1361-6641/ab4372`.

[16] S. S. Pasayat, C. Gupta, M. S. Wong, Y. Wang, S. Nakamura, S. P. Denbaars, S. Keller, and U. K. Mishra, "Growth of strain-relaxed InGaN on micrometer-sized

patterned compliant GaN pseudo-substrates," *Appl. Phys. Lett.*, vol. 116, no. 11, p. 111 101, 2020. DOI: `10.1063/5.0001480`.

[17] R. C. White, M. Khoury, F. Wu, S. Keller, M. Rozhavskaia, D. Sotta, S. Nakamura, and S. P. Denbaars, "MOCVD growth of thick V-pit-free InGaN films on semi-relaxed InGaN substrates," *Semicond. Sci. Technol.*, vol. 36, no. 1, 2020. DOI: `10.1088/1361-6641/abc51c`.

[18] R. C. White, H. Li, M. Khoury, C. Lynsky, M. Iza, S. Keller, D. Sotta, S. Nakamura, and S. P. DenBaars, "Ingan-based microled devices approaching 1% eqe with red 609 nm electroluminescence on semi-relaxed substrates," *Crystals*, vol. 11, no. 11, 2021. DOI: `10.3390/cryst11111364`.

[19] K. Hestroffer, F. Wu, H. Li, C. Lund, S. Keller, J. S. Speck, and U. K. Mishra, "Relaxed c-plane InGaN layers for the growth of strain-reduced InGaN quantum wells," *Semicond. Sci. Technol.*, vol. 30, no. 10, 2015. DOI: `10.1088/0268-1242/30/10/105015`.

[20] K. Ohkawa, T. Watanabe, M. Sakamoto, A. Hirako, and M. Deura, "740-nm emission from InGaN-based LEDs on c-plane sapphire substrates by MOVPE," *J. Cryst. Growth*, vol. 343, no. 1, pp. 13–16, 2012. DOI: `10.1016/j.jcrysgro.2011.12.075`.

[21] K. Kishino, A. Yanagihara, K. Ikeda, and K. Yamano, "Monolithic integration of four-colour ingan-based nanocolumn leds," *Electron. Lett.*, vol. 51, no. 11, pp. 852–854, 2015. DOI: `https://doi.org/10.1049/el.2015.0770`.

[22] K. Chung, J. Sui, T. Sarwar, and P.-C. Ku, "Feasibility study of nanopillar led array for color-tunable lighting and beyond," *Opt. Express*, vol. 27, no. 26, pp. 38 229–38 235, 2019. DOI: `10.1364/OE.382287`.

[23] K. Kishino, N. Sakakibara, K. Narita, and T. Oto, "Two-dimensional multicolor (RGBY) integrated nanocolumn micro-LEDs as a fundamental technology of micro-LED display," *Appl. Phys. Express*, vol. 13, no. 1, p. 014 003, 2019. DOI: `10.7567/1882-0786/ab5ad3`.

Chapter 3

Relaxed buffers by thermal decomposition of an underlayer

In this chapter, a novel method for relaxing an InGaN buffer layer across a planar 2-inch substrate is explored. A high degree of relaxation is achieved in a single MOCVD growth using thermal decomposition of an InGaN underlayer, the decomposition layer (DL).

The temperature sensitivity and thermal degradation of InGaN has been rigorously studied.[1]–[5] At the extreme end, InN capping temperature was studied by Ku et al. where higher temperatures were shown to severely degrade the InN.[6] However, high temperatures will degrade lower composition InGaN as well. In one particularly interesting study, Smalc-Koziorowska et al. showed that InGaN layers will thermally decompose.[5] To start, metal vacancies present in annealed quantum wells agglomerate to form a small void. The quantum wells then segregate with indium diffusing to the void walls, forming
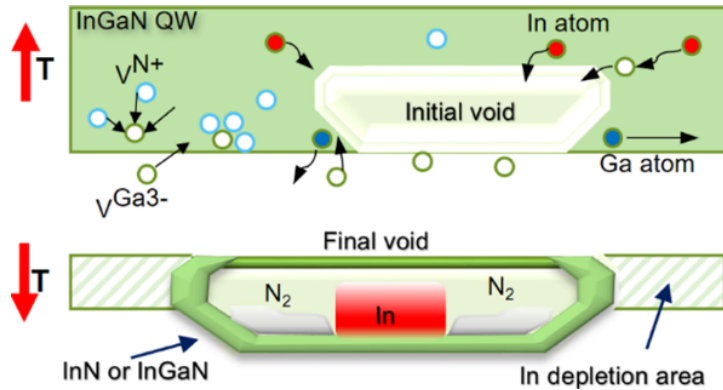
30

Figure 3.1: Mechanism of void formation in annealed InGaN layers. Reproduced from Koziorowska et al. with permission.[5] Copyright 2021 American Chemical Society

In-rich regions around the void and leaving In-depleted regions elsewhere. The In-rich regions thermally decompose into metallic In and nitrogen to expand the void. This process is shown generally in figure 3.1.

Our goal was to explore this void-forming mechanism in InGaN. Particularly, we were interested in whether this mechanism could be used to strain relax an InGaN layer by healing of crystal growth around the 3D structures, formation of dislocation half-loops or complete delamination/dissociation of the crystal above the decomposed layer to the substrate below.

3.1 First demonstration

This initial PL experiment consisted of two samples, the experimental sample and the reference sample. The epitaxial structure of the two samples is shown in figure 3.2. Both samples were grown by MOCVD on (0001) single-side polished (SSP) sapphire. The experimental sample consisted of a UID-GaN template, thermally decomposed In-
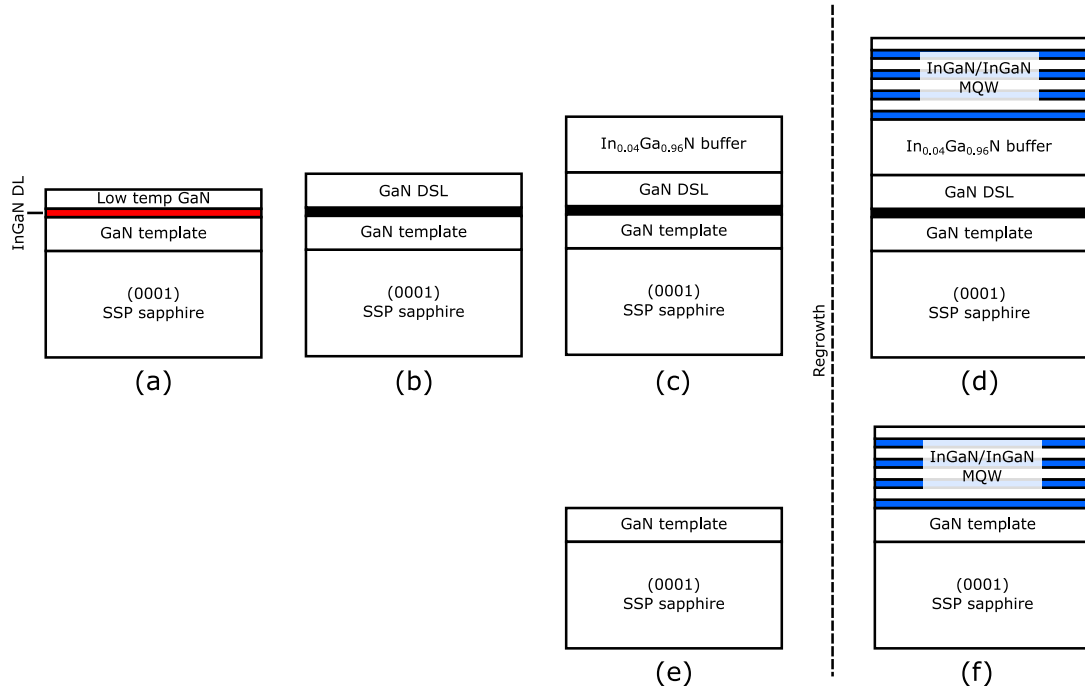
Figure 3.2: Experimental (top row) and reference growths (bottom row) performed in this study. (a)-(c) depict the first growth of the InGaN buffer. In (a), a UID-GaN template and high indium composition DL are grown and capped with low-temperature GaN. Then, in (b), the temperature is increased and high-temperature GaN is grown to thermally decompose the DL. In (c), the InGaN buffer layer is grown. In a second growth, a reference sample (e) was grown with a simple GaN template. The experimental sample and reference sample with structures given by (c) and (e) respectively were then co-loaded for a MQW regrowth. The final experimental and reference sample structures are shown in (d) and (f) respectively.

GaN underlayer, UID-GaN layer, InGaN buffer and InGaN/InGaN MQW. The reference sample consisted only of a GaN template and InGaN/InGaN MQW.

3.1.1 Relaxed InGaN buffer

For the experimental sample, first a 5.5 µm UID-GaN template was grown at 1200 °C in TMG. Next, a 3 nm, high-composition InGaN layer was grown at 750 °C with a TEG flow of 30 sccm and a TMI flow of 90 sccm, corresponding to 7.6 and 7.7 µmol min^{-1} respectively. While no calibration was done for InGaN composition, the flows and temperature are similar to those used to grow red InGaN QWs with indium composition over 30%. This InGaN underlayer is referred to as the decomposition layer (DL). Next, 100 nm of GaN was grown, referred to as the decomposition stop layer (DSL). The first 30 nm was grown at a low temperature of 750 °C to preserve the InGaN DL. This structure is shown in figure 3.2(a). The next 70 nm was grown at a temperature of 1000 °C in order to decompose the DL and provide higher quality crystal growth, shown in figure 3.2(b). Finally, 200 nm of In$_{0.04}$Ga$_{0.96}$N was grown at 920 °C with the same precursor flows as used in the DL. The structure is shown in figure 3.2(c). At this point the sample was unloaded and characterized.

Figure 3.3 shows a high resolution x-ray diffraction (HRXRD) reciprocal space map (RSM) taken around the $(\bar{1}\,\bar{1}\,2\,4)$ reciprocal lattice point. An RSM around an off-axis peak allows for the determination of both InGaN composition from the peak spacing as well as the strain state of the InGaN from the misalignment of the two peaks in
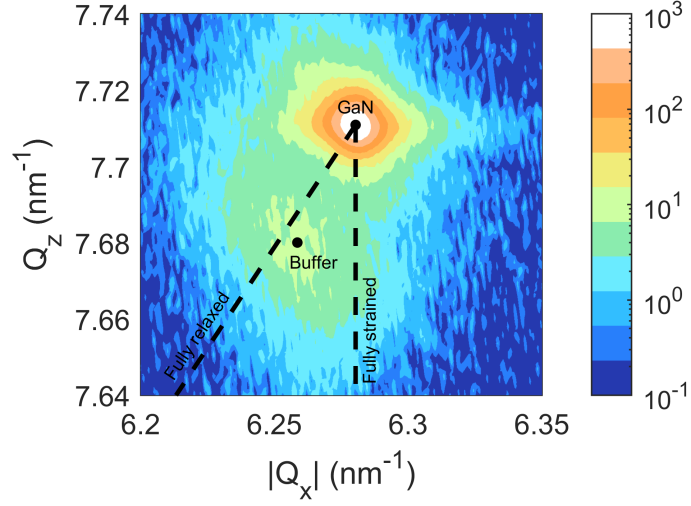
Figure 3.3: X-ray diffraction reciprocal space map around the $(\bar{1}\,\bar{1}\,2\,4)$ of the experimental sample after InGaN buffer growth. Marked points show the GaN template and InGaN buffer peaks. Dashed lines show positions of fully strained and fully relaxed InGaN of arbitrary composition. Reproduced from Chan et al. with permission.[7]

Q_x. This misalignment stems from a difference in the in-plane lattice constant between the two films, indicating some amount of relaxation. The method used throughout this dissertation to calculate both InGaN composition and degree of relaxation is detailed as follows:

From the (Q_x, Q_z) coordinates of the two films, a and c lattice constants can be determined.

$$a_{\text{InGaN}} = \frac{Q_{x,\text{GaN}}}{Q_{x,\text{InGaN}}} a_{\text{GaN}}$$

$$c_{\text{InGaN}} = \frac{Q_{z,\text{GaN}}}{Q_{z,\text{InGaN}}} c_{\text{GaN}}$$

An indium composition, x, can then be guessed and fully relaxed lattice constants

can be found using Vegard's law.

$$a_{\text{relaxed}} = xa_{\text{InN}} + (1 - x)a_{\text{GaN}}$$

$$c_{\text{relaxed}} = xc_{\text{InN}} + (1 - x)c_{\text{GaN}}$$

The relevant elastic constants for an $\text{In}_x\text{Ga}_{1-x}\text{N}$ film may also be determined by Vegard's law.

$$C_{13,\text{InGaN}} = xC_{13,\text{InN}} + (1 - x)C_{13,\text{GaN}}$$

$$C_{33,\text{InGaN}} = xC_{33,\text{InN}} + (1 - x)C_{33,\text{GaN}}$$

Next, the in-plane and out-of-plane strain in the film, assuming indium composition x, can be calculated using the Poisson ration, C_{13}/C_{33}.

$$\epsilon_{\|} = \frac{a_{\text{InGaN}}}{a_{\text{relaxed}}}$$

$$\epsilon_{\perp} = -2\left(\frac{C_{13,\text{InGaN}}}{C_{33,\text{InGaN}}}\right)\epsilon_{\|}$$

Finally, the expected lattice constant c for $\text{In}_x\text{Ga}_{1-x}\text{N}$ with the calculated out-of-plane strain can be calculated.

$$c_{\text{expected}} = c_{\text{relaxed}}(\epsilon_{\perp} + 1)$$

If this expected lattice constant does not match the one calculated for the film, then the guessed indium composition is incorrect. This process is iterated through until $c_{\text{expected}} = c_{\text{InGaN}}$ to find the composition corresponding to the RSM peak. The degree of relaxation can then be calculated.

$$\text{relaxation } [\%] = \frac{a_{\text{InGaN}} - a_{GaN}}{a_{\text{relaxed}} - a_{GaN}} \times 100$$

Using the points plotted in figure 3.3 and the method described above determines the buffer to be 85% relaxed $In_{0.04}Ga_{0.96}N$. The peak appears fairly spread out compared to the GaN peak, indicating relatively poor crystal quality. As shown in figure 3.4, the surface shows poor morphology and large amounts of pitting. The experimental sample had a full 30 nm of low-temperature GaN grown at 750 °C. This low-temperature GaN was grown continuously at a rate of $0.33\,\text{Å}\,\text{s}^{-1}$ with no special consideration for crystal quality or morphology other than the reduced growth rate. Biaxial relaxation was confirmed with a second off-axis $(1\,0\,\bar{1}\,5)$ RSM.

3.1.2 Quantum well regrowth

The reference sample, depicted in 3.2(e) consisted of a simple UID-GaN template grown with the same conditions as that of the experimental sample. The reference sample was
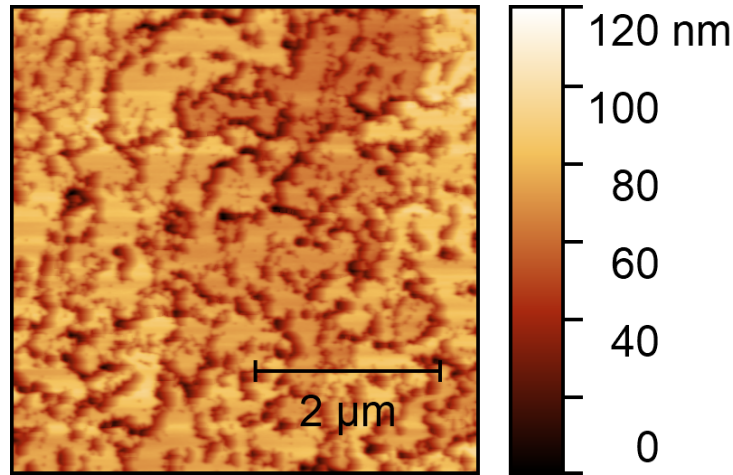
Figure 3.4: $5 \times 5 \, \mu m^2$ atomic force micrograph of the InGaN buffer surface. Reproduced from Chan et al. with permission.[7]

then unloaded.

Both the experimental and reference samples were cleaned in acetone, isopropyl alcohol and deionized water, and then treated with a 5 min UV ozone exposure and 5 min buffered HF dip. They were then co-loaded into the MOCVD reactor for the MQW regrowth. The two samples are depicted in figures 3.2(d) and 3.2(f). The MQW consisted of four periods of 2.5 nm InGaN QWs with 2.5 nm GaN capping layers grown at 865 °C. The group-III precursor flows were identical to those used in the DL. Additional 8.3 nm InGaN barriers were grown at 900 °C and the TMI flow was reduced to 10 sccm to reduce the InGaN composition and improve crystal quality. Both samples were then unloaded and characterized.

As shown in figure 3.5 the reference and experimental samples are visibly different. The reference sample appeared similar to a standard blue LED, i.e. uniform and mostly transparent with a slight yellow tint from the InGaN layers. The experimental sample
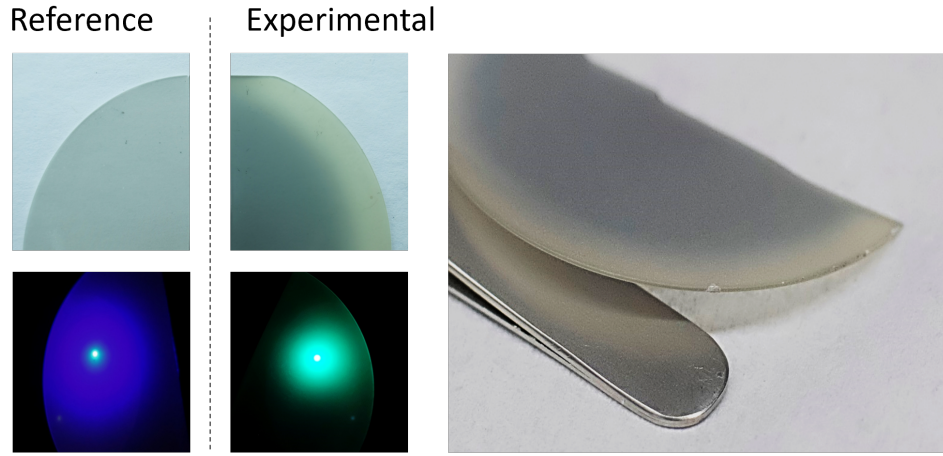
Figure 3.5: Photographs of reference (left column) and experimental samples (right) under white light as well as excited by a 325 nm HeCd laser.

appeared dark at the center with a distinct yellow tinge, indicative of higher indium content. The dark center is from the decomposed InGaN DL and appears dark due to the formation of voids, metallic indium and defects. The outside area appears lighter and small indium droplets can be observed on the edge of the sample.

Figure 3.6 shows room temperature photoluminescence (RT-PL) from the two samples excited by a 325 nm HeCd laser. PL from the reference sample is shown at the half-radius of the half-2-inch sample, while PL from the center, half-radius and edge is shown for the experimental sample. Between the two half-radius points, a 75 nm red-shift is observed in peak wavelength, from 440 nm to 515 nm. This wavelength shift can be attributed to higher indium incorporation in the experimental sample on the relaxed template. This may be due to a reduction in strain in the quantum wells and compositional pulling. Similar, albeit lower magnitude red-shifting of emission has been observed with co-loaded MQW regrowths on other relaxed InGaN templates.[8], [9] Since the InGaN MQW on
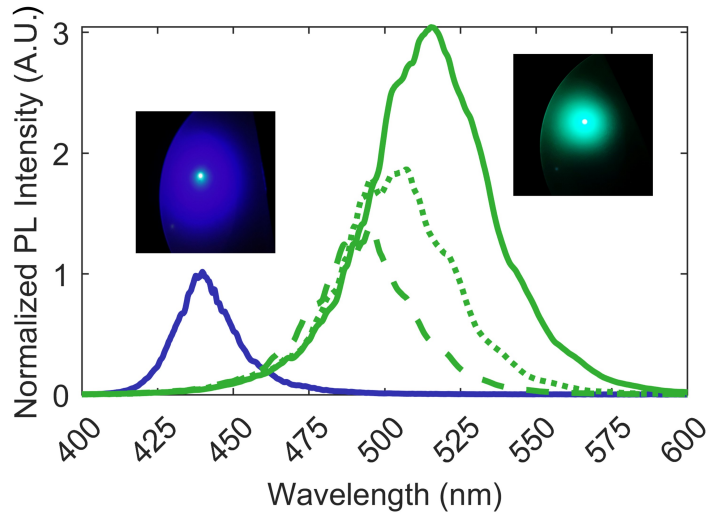
38

Figure 3.6: Room temperature PL taken with 325 nm HeCd laser of the experimental sample (green) and the reference sample (blue). Solid lines were taken at the half-radius, the dotted line was taken at the center and the dashed line was taken at the edge. Reproduced from Chan et al. with permission.[7]

the experimental sample was grown on a largely relaxed $In_{0.04}Ga_{0.96}N$ buffer, the strain during the QW growth was reduced, allowing for additional indium uptake during growth of the thin QW layers.

The green PL emission from the experimental sample showed about three-fold higher peak intensity. The two samples were co-loaded during the same MQW regrowth, so the active volume remains constant. This leaves an increase in IQE or light extraction as the culprit. Based off of the increased FWHM and poor surface morphology, indicative of high dislocation density, the IQE of the experimental sample is most likely lower than that of the reference. The greatly roughened surface, however, will increase the light extraction efficiency, especially given that both samples were grown on SSP sapphire rather than a patterned sapphire substrate (PSS).

3.2 Morphological improvements

The poor surface morphology shown in figure 3.4 is of great concern. Not only is it indicative of high dislocation densities since pits nucleate at threading dislocations, but it can also cause issues in the subsequent layers. Optimizing growth conditions of the the InGaN DL, GaN DSL and InGaN buffer have profound effect on the final morphology of the relaxed buffer. Additionally, moving growth from SSP sapphire substrates to PSS yields better starting templates.

Firstly, increasing the temperature of the GaN DSL growth and introducing hydrogen to the carrier gas greatly improves the morphology. Three samples were grown starting with an n-GaN template, 3 nm InGaN DL grown at 720 °C, 2 nm of GaN cap grown at 720 °C and 2 nm of GaN grown at 835 °C, all with a nitrogen carrier gas. The three samples had an additional 70 nm GaN DSL grown at varying conditions. The first was grown at 930 °C in all nitrogen carrier gas. The second sample had a DSL grown at 975 °C in nitrogen carrier gas. The final sample had the DSL grown at 975 °C with the first 10 nm being in nitrogen and the last 60 nm being in hydrogen.

Figure 3.7 shows AFM scans of the surface after GaN DSL growth for these three samples. The first sample with a maximum temperature of 930 °C grown in all nitrogen shows a 3D, small island-like growth mode. Increasing the temperature of the GaN DSL to 975 °C greatly improves the morphology and moves to a highly pitted, step morphology. The steps are very short due to the pitting and dislocations pinning the step edges. Switching the carrier gas to hydrogen in the final 60 nm further decreases
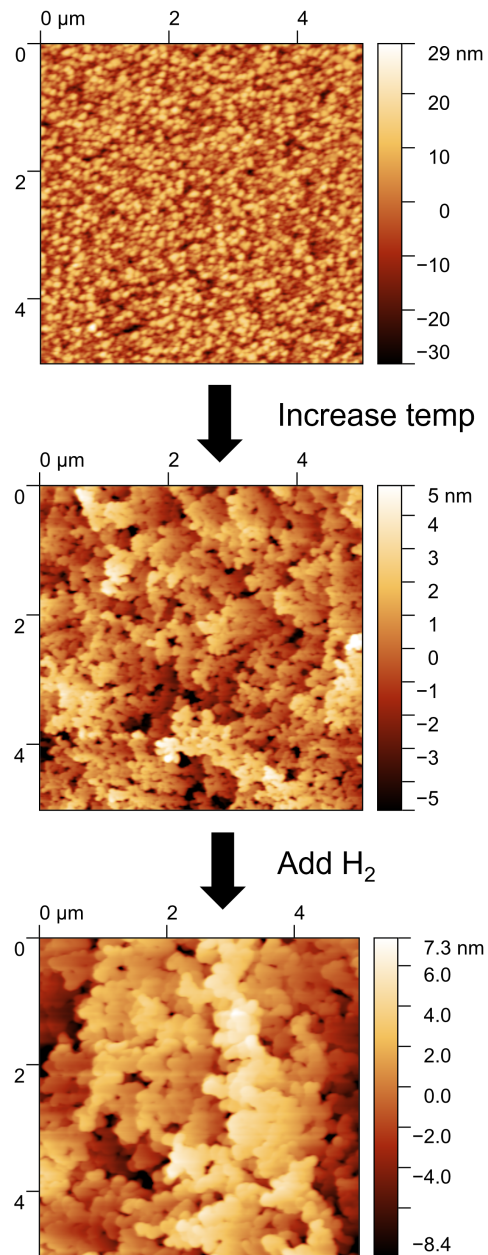
Figure 3.7: 5×5 µm² atomic force micrograph of the GaN DSL surface showing the effect of increasing GaN DSL growth temperature and introducing hydrogen to the carrier gas
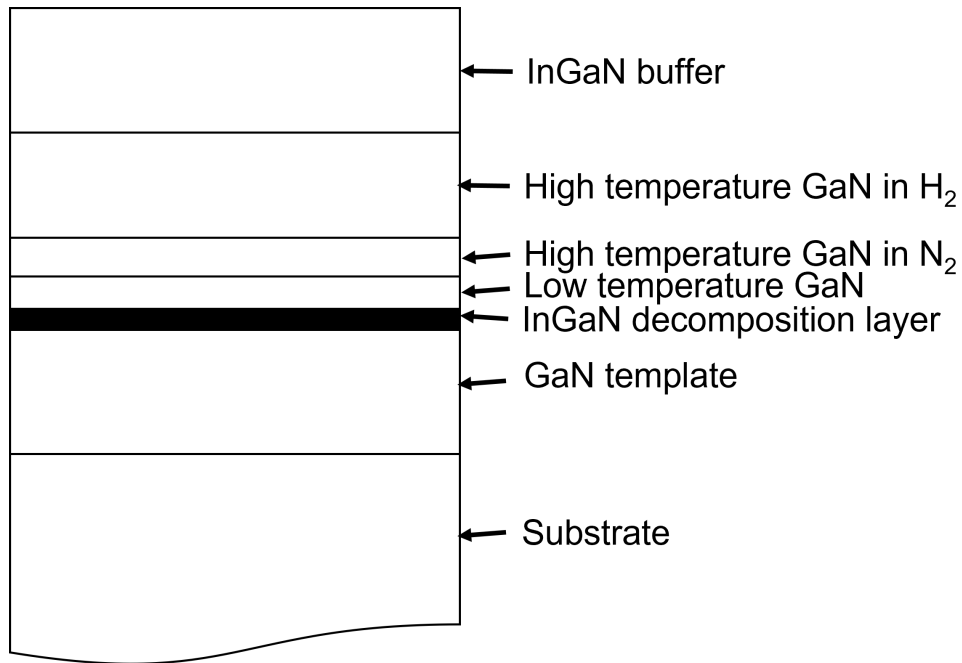
Figure 3.8: General layer structure of the strain-relaxed InGaN template

the pitting and smooths the surface. This growth showed a RMS surface roughness of 2.8 nm. Further increasing the growth temperature of the high temperature portion of the DSL shows morphology improvements.

Figure 3.8 shows the general structure of the improved strain-relaxed InGaN template. The template consists of a thin, InGaN decomposition layer grown between 700 °C and 800 °C for high indium content. This layer is capped with low temperature GaN. The temperature is ramped up and additional high temperature GaN is grown in nitrogen before switching the carrier gas to hydrogen. Finally, the InGaN buffer is grown.

The thickness of the GaN DSL is limited by the strain of the layer. The decomposed InGaN layer determines the lattice constant of the subsequent layers, placing the GaN in tensile strain. With a 3 nm DL grown at 750 °C, the GaN DSL is increased to 1 µm, 2 µm
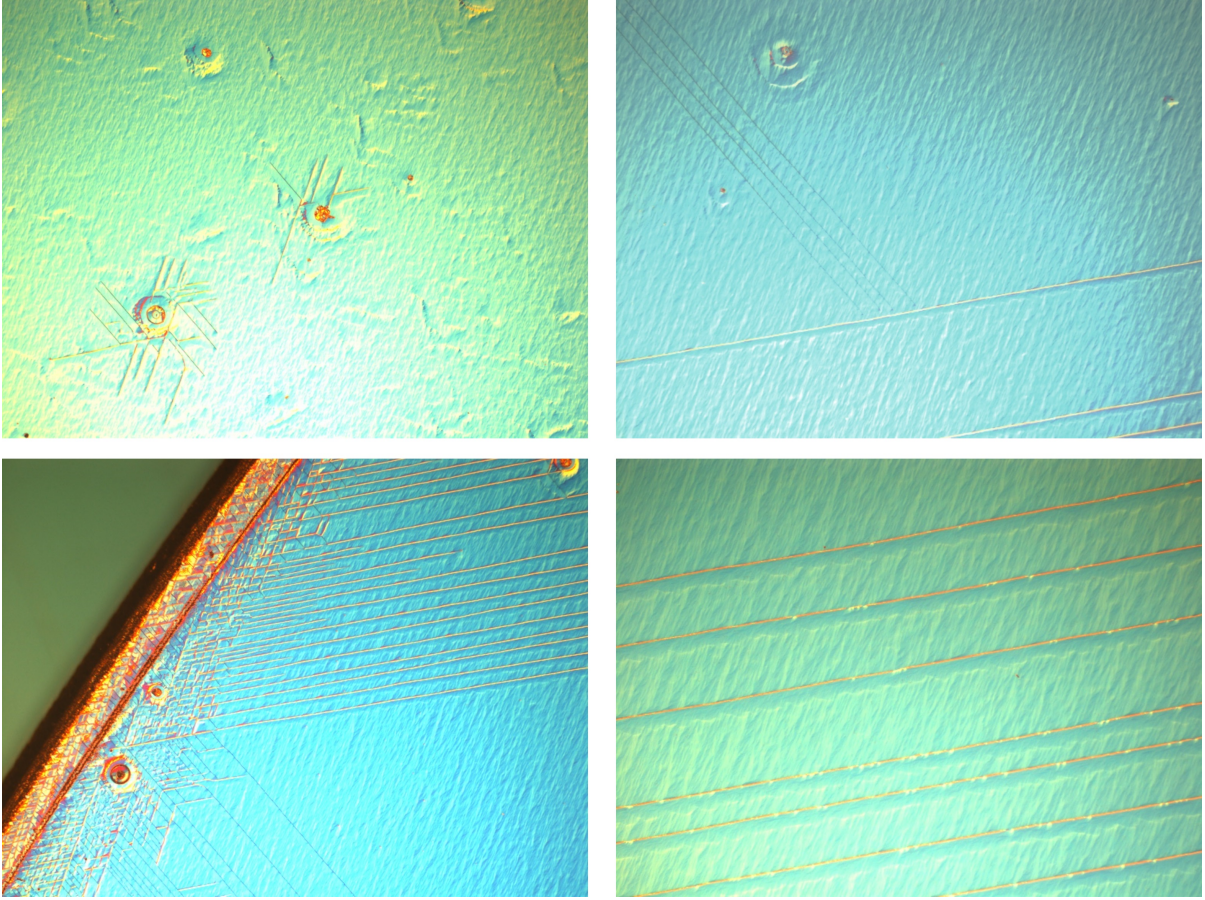
Figure 3.9: Differential interference contrast micrographs of cracked, 3 µm GaN DSLs and 3 µm. A 10x 5 nm/5 nm InGaN/GaN buffer was included with an average composition around 2%. While the samples with 1 and 2 µm GaN DSLs were unremarkable, the sample with 3 µm GaN showed signs of cracking under a Nomarski microscope as shown in figure 3.9.

The structure of the InGaN buffer also plays a large roll in surface morphology. White et al. showed that the surface morphology of relaxed InGaN is greatly impacted by choice of V/III ratio, temperature and carrier gas as well as the inclusion of GaN interlayers.[10] In this work, White et al. find conditions to grow thick, relaxed InGaN

Figure 3.10: General layer structure of a single period of strain-relaxed InGaN buffer

with smooth surface morphologies without the presence of v-pits. These changes of increased temperature in interlayers, lower V/III ratio and inclusion of hydrogen all work to increase adatom mobility and lateral diffusion across the surface, allowing the growth to fill in voids and pits.

The general structure of the InGaN buffer with interlayers is shown in figure 3.10. For our case, we chose to use a modest increase in temperature, from a T_1 determined by the desired composition of InGaN, from $920\,°C$ to $950\,°C$, to a T_2 of $1000\,°C$. The InGaN thickness was $16\,nm$ and the GaN interlayer was $4\,nm$, split equally between the two growth conditions. During the second portion of the GaN interlayer growth, the carrier gas was switched from 100% nitrogen to 95/5% nitrogen/hydrogen. The ammonia flow was lowered to 1 slm with TEG and TMI flows being $15.2\,\mu mol\,min^{-1}$ to lower the V/III ratio.

Using these buffer growth conditions in conjunction with further increase in temperature of the GaN DSL, we were able to achieve smooth, highly relaxed InGaN buffer layers. Two samples were grown to demonstrate these optimized conditions with two different buffer compositions. These samples had InGaN DLs grown at $750\,°C$ and $200\,nm$ GaN
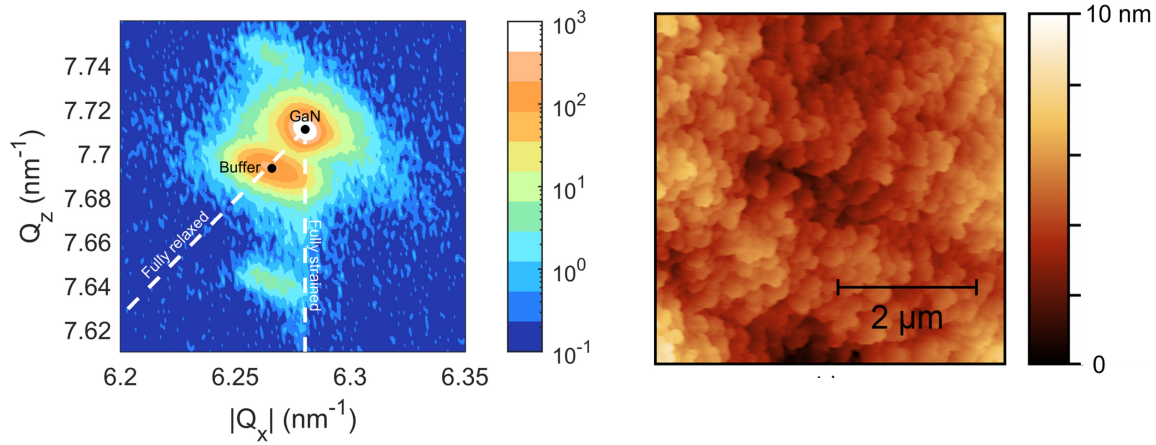
Figure 3.11: Reciprocal space map and 5×5 µm^2 atomic force micrograph of a 90% relaxed In$_{0.025}$Ga$_{0.975}$N buffer with 1.1 nm RMS surface roughness. Reproduced from Chan et al. with permission.[7]

DSLs grown following the layer structure in figure 3.8. The low temperature GaN was a total of 10 nm thick, with the remainder being grown at 1150 °C. The last 150 nm were grown completely in hydrogen carrier gas.

The first sample is characterized in figure 3.11. The InGaN buffer was comprised of 50 periods of InGaN/GaN superlattice with the conditions listed previously. To achieve an average of In$_{0.025}$Ga$_{0.975}$N, the InGaN buffer layers were grown with a T_1 of 950 °C. As shown in the RSM, the buffer layer appears near the fully relaxed line, with the center of the peak showing 90% relaxed In$_{0.025}$Ga$_{0.975}$N. Superlattice fringing is also seen corresponding to the 20 nm period of the buffer. The AFM scan shows a much smoother surface than previously seen, with an RMS surface roughness of just 1.1 nm. The InGaN is now has a stepped surface morphology, but short steps are still seen due to the increased dislocation density causing pinning of the step edges.

The second sample is characterized in figure 3.12. This sample had an InGaN buffer
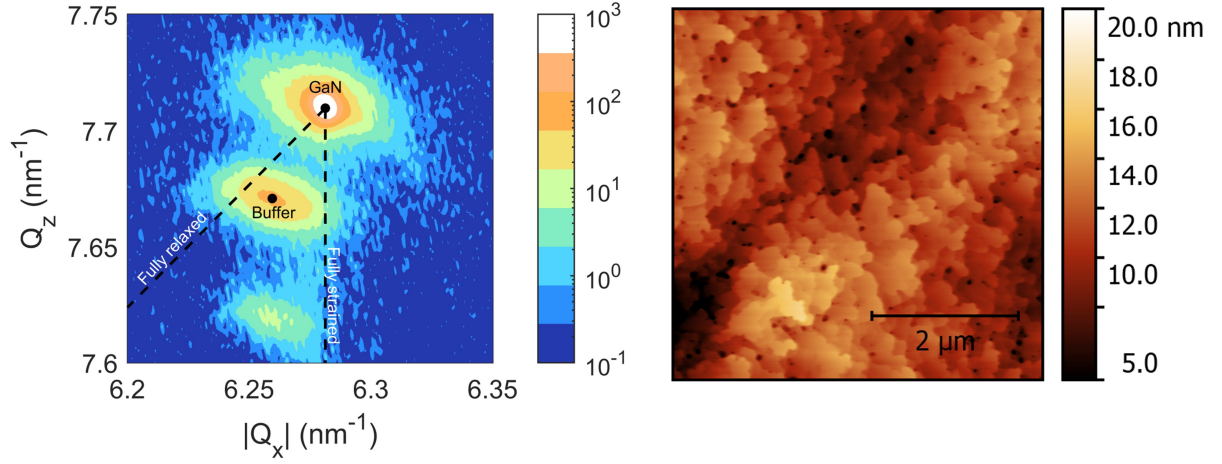
45

Figure 3.12: Reciprocal space map and 5×5 µm^2 atomic force micrograph of a 70% relaxed In$_{0.046}$Ga$_{0.954}$N buffer with 2.0 nm RMS surface roughness

layer grown with a T_1 of 920 °C but was otherwise identical. Since the composition of the DL was not increased, the in-plane lattice constant remains similar to that of the previous sample. The RSM shows 70% relaxation of the In$_{0.046}$Ga$_{0.954}$N average buffer layer. This means that the growth of the InGaN buffer layer is strained, potentially degrading the surface morphology. The surface morphology appears similar to that of the lower composition buffer shown in figure 3.11, but some pitting is seen and a higher RMS roughness of 2 nm is observed. Increased strain in the layer as well as the higher composition InGaN and only partially optimized buffer conditions all contribute to this.

3.3 Further characterization

From the previous section, it is clear that we can grow relatively smooth relaxed InGaN buffer layers. Figure 3.11 shows a highly relaxed buffer layer with an RMS surface roughness of 1.1 nm and an in-plane lattice constant of 3.197 Å. Similarly, 3.12 shows a
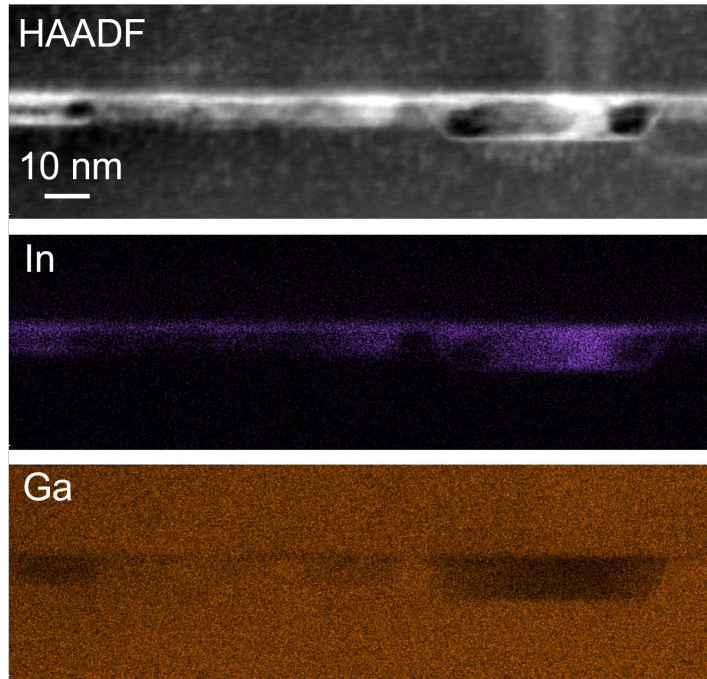
Figure 3.13: High angle annular dark field image (top) and energy-dispersive x-ray maps of In (middle) and Ga (bottom) of a decomposed InGaN layer. Reproduced from Chan et al. with permission.[7]

partially relaxed buffer layer with an RMS surface roughness of 2.0 nm and an in-plane lattice constant of 3.201 Å.

However, the relaxation mechanism remains unclear. A high angle annular dark field (HAADF) transmission electron micrograph (TEM) of a decomposed InGaN DL is shown in figure 3.13. The TEM distinctly shows void formation similar to that described by Smalc-Koziorowska et al. in figure 3.1.[5] From the energy-dispersive x-ray (EDX) maps, the voids are shown to be In-rich, as expected.

The sample characterized in figure 3.11 was further characterized by TEM. A two-beam contrast TEM and HAADF TEM image of the sample is shown in figure 3.14. The InGaN DL is seen to be largely decomposed into void regions. From the DL, dislocations
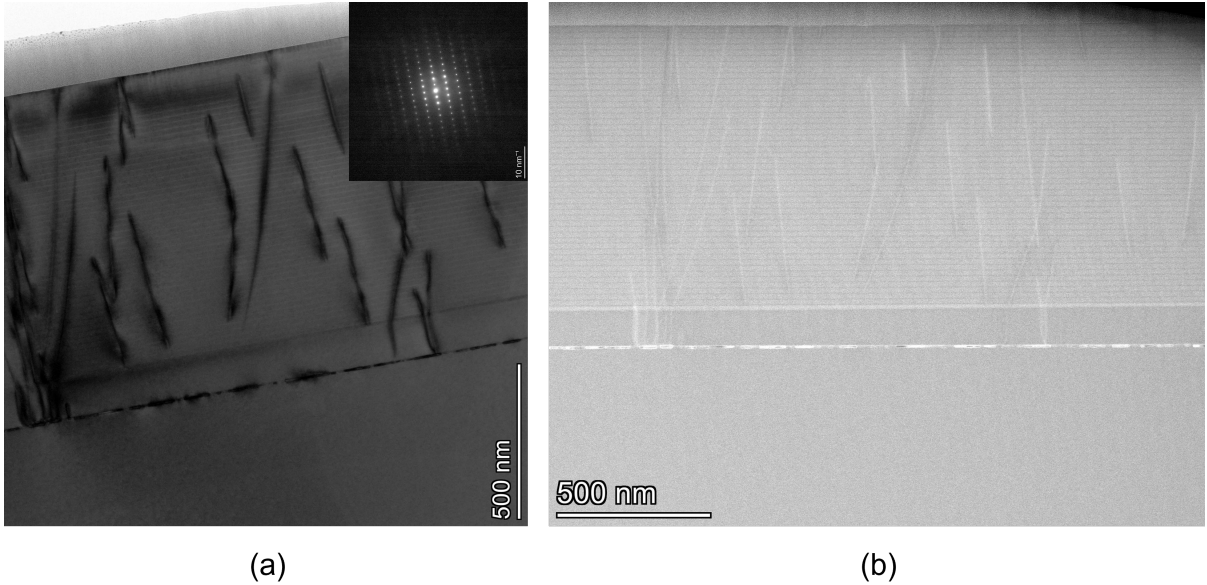
(a)   (b)

Figure 3.14: Transmission electron micrographs of sample characterized in figure 3.11. (a) Multiple electron beam diffraction contrast image in zone axis B=$[11\bar{2}0]$ and (b) high angle annular dark field image.

are formed, some of which thread upward and incline at the InGaN superlattice.

The threading dislocation density in the layers above the DL is orders of magnitude higher than that in the GaN-on-PSS substrate. This would indicate that the relaxation seen is, at least in part, plastic relaxation from dislocation formation. Despite this, we will show in the following chapter that these relaxed buffer layers can yield competitive or better device results as compared to other relaxed buffer methods. The increased dislocation density and large amount of InGaN can nucleate v-defects which can lead to increased hole injection to the active region and act as a barrier to the dislocation.

3.4 Chapter summary

A first demonstration of a biaxially strain-relaxed InGaN buffer by thermal decomposition of an InGaN underlayer was presented in this chapter. This $In_{0.04}Ga_{0.96}N$ buffer layer showed 85% biaxial relaxation across an entire 2-inch SSP sapphire substrate achieved in a single MOCVD growth. Quantum wells regrown on the relaxed buffer red-shifted 75 nm by PL as compared to a co-loaded reference GaN template.

While the first demonstration was very rough and showed a large amount of pitting, morphological improvements were shown to be possible. Using a higher growth temperature and hydrogen in the carrier gas during GaN DSL growth, the surface showed significant smoothing. Further improvements were made by the addition of high temperature GaN interlayers in the InGaN buffer. With these improvements, we demonstrated a 70% biaxially relaxed $In_{0.046}Ga_{0.954}N$ buffer with an RMS surface roughness of 2 nm.

TEM confirmed that the InGaN DL was being thermally decomposed as expected. However, it is clear that the dislocation density has increased and the relaxation is, at least partially, due to this dislocation formation. In the following chapter we will show that, despite the increased dislocation density, these relaxed buffer layers can be used to produce red micro-LEDs competitive or better than other relaxed InGaN techniques.

References

[1] Y. T. Moon, D. J. Kim, K. M. Song, C. J. Choi, S. H. Han, T. Y. Seong, and S. J. Park, "Effects of thermal and hydrogen treatment on indium segregation in InGaN/GaN multiple quantum wells," *J. Appl. Phys.*, vol. 89, no. 11, pp. 6514–6518, 2001. DOI: 10.1063/1.1370368.

[2] Z. Li, J. Liu, M. Feng, K. Zhou, S. Zhang, H. Wang, D. Li, L. Zhang, D. Zhao, D. Jiang, H. Wang, and H. Yang, "Suppression of thermal degradation of InGaN/GaN quantum wells in green laser diode structures during the epitaxial growth," *Appl. Phys. Lett.*, vol. 103, p. 152 109, 2013. DOI: 10.1063/1.4824850.

[3] D. Queren, M. Schillgalies, A. Avramescu, G. Brüderl, A. Laubsch, S. Lutgen, and U. Strauß, "Quality and thermal stability of thin InGaN films," *J. Cryst. Growth*, vol. 311, no. 10, pp. 2933–2936, 2009. DOI: 10.1016/j.jcrysgro.2009.01.066.

[4] J. Kim, H. Kim, and S. N. Lee, "Thermal degradation in InGaN quantum wells in violet and blue GaN-based laser diodes," *Curr. Appl. Phys.*, vol. 11, S167–S170, 2011. DOI: 10.1016/j.cap.2011.07.024.

[5] J. Smalc-Koziorowska, E. Grzanka, A. Lachowski, R. Hrytsak, M. Grabowski, S. Grzanka, S. Kret, R. Czernecki, H. Turski, L. Marona, T. Markurt, T. Schulz, M. Albrecht, and M. Leszczynski, "Role of Metal Vacancies in the Mechanism of Thermal Degradation of InGaN Quantum Wells," *ACS Appl. Mater. Interfaces*, vol. 13, no. 6, pp. 7476–7484, 2021. DOI: 10.1021/acsami.0c21293.

[6]   C. S. Ku, W. C. Chou, and M. C. Lee, "Optical investigations of InN nanodots capped by GaN at different temperatures," *Appl. Phys. Lett.*, vol. 90, p. 132 116, 2007. DOI: 10.1063/1.2716347.

[7]   P. Chan, S. P. DenBaars, and S. Nakamura, "Growth of highly relaxed InGaN pseudo-substrates over full 2-in. wafers," *Appl. Phys. Lett.*, vol. 119, no. 13, 2021. DOI: 10.1063/5.0064755.

[8]   S. S. Pasayat, C. Gupta, D. Acker-James, D. A. Cohen, S. P. Denbaars, S. Nakamura, S. Keller, and U. K. Mishra, "Fabrication of relaxed InGaN pseudo-substrates composed of micron-sized pattern arrays with high fill factors using porous GaN," *Semicond. Sci. Technol.*, vol. 34, no. 11, p. 115 020, 2019. DOI: 10.1088/1361-6641/ab4372.

[9]   A. Even, G. Laval, O. Ledoux, P. Ferret, D. Sotta, E. Guiot, F. Levy, I. C. Robin, and A. Dussaigne, "Enhanced in incorporation in full InGaN heterostructure grown on relaxed InGaN pseudo-substrate," *Appl. Phys. Lett.*, vol. 110, no. 26, p. 262 103, 2017. DOI: 10.1063/1.4989998.

[10]   R. C. White, M. Khoury, F. Wu, S. Keller, M. Rozhavskaia, D. Sotta, S. Nakamura, and S. P. Denbaars, "MOCVD growth of thick V-pit-free InGaN films on semi-relaxed InGaN substrates," *Semicond. Sci. Technol.*, vol. 36, no. 1, 2020. DOI: 10.1088/1361-6641/abc51c.

Chapter 4

Red LEDs on strain-relaxed InGaN buffers

The next step is to fabricate LEDs on the relaxed InGaN buffers presented in the previous chapter. Initially, red LEDs were targeted because of their highly strained active regions benefiting the most from a relaxed InGaN buffer. After the first demonstration of red LEDs on these relaxed buffers. Red micro-LEDs competitive or better than those reported on other relaxed InGaN buffers are then demonstrated. Work on integrated RGB micro-LEDs as well as far-red LEDs is presented in appendix A.

While morphological improvements were presented in the previously in section 3.2, these experiments were not done at the time of the first red LED device growths. Additionally, the most successful devices in red wavelengths used relatively high composition buffer layers with high degrees of relaxation compared to those reported in figures 3.11

and 3.12.

# 4.1 Red LEDs with high active region growth temperature

To begin, a red LED is demonstrated on a fully relaxed $In_{0.07}Ga_{0.93}N$ layer. Because of the high degree of relaxation in the structure, and perhaps in part due to the surface morphology, the red MQW was grown at an exceedingly high temperature of 870 °C, a temperature typical of blue emission. The InGaN layer was relaxed by thermal decomposition of an InGaN underlayer as described in the previous chapter. As previously shown in figure 3.6, a 75 nm red shift from blue to green was seen by RT-PL of QWs grown at 865 °C on an 85% relaxed $In_{0.04}Ga_{0.96}N$ buffer layer.

4.1.1 Growth and structure

Figure 4.1(a) shows the device and epitaxial structure and (b) shows a photograph of a completed LED in operation at $100\,A\,cm^{-2}$. The structure was grown on top of a 5 µm uid-GaN template on PSS. First, an additional 5 µm of uid-GaN was grown to bury the regrowth interface. The 3 nm InGaN DL was then grown at 720 °C and capped with 4 nm of low temperature GaN. In this device, an InGaN/GaN superlattice was used in place of both the GaN DSL and InGaN buffer presented previously. The first InGaN/GaN superlattice consisted of five periods of 18 nm n-InGaN and 2 nm n-GaN grown at 930 °C.
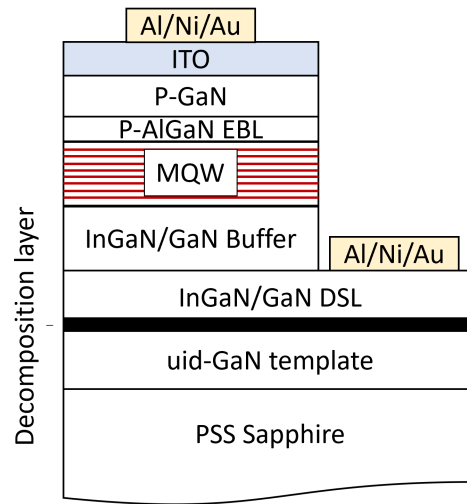
(a)
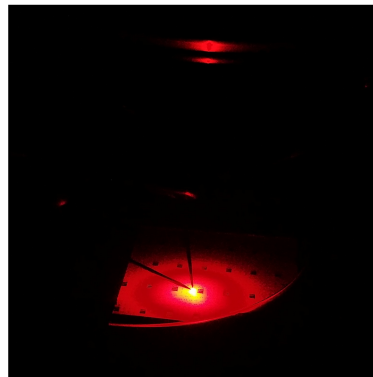
(b)

Figure 4.1: Device and epitaxial structure (a) and photograph during operation at $100\,\mathrm{A\,cm^{-2}}$ (b) of a red LED on relaxed InGaN buffer. Reproduced from Chan et al. with permission.[1]
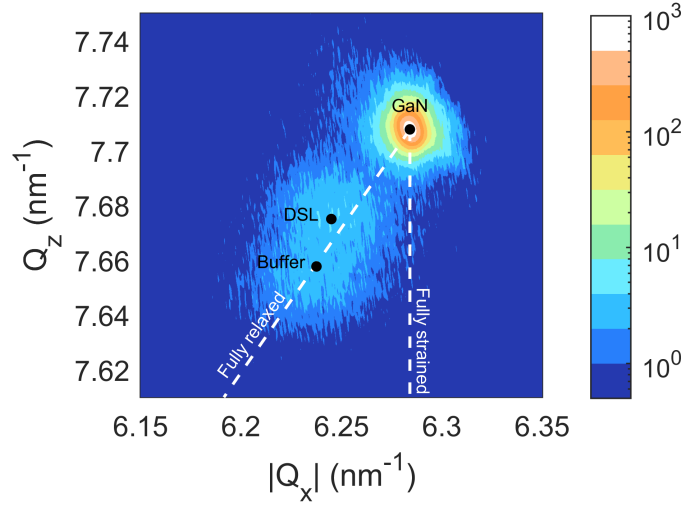
Figure 4.2: Reciprocal space map of the InGaN DSL and buffer layers taken around the $(\bar{1}\,\bar{1}\,2\,4)$ peak. Reproduced from Chan et al. with permission.[1]

The second InGaN/GaN superlattice consisted of five periods of 20 nm n-InGaN and 2 nm n-GaN grown at 900 °C. At this point, the structure was unloaded for characterization.

As before, the purpose of the higher temperature growth was to decompose the InGaN DL and form voids to partially relax the layer and those above. For the red LEDs, more aggressive conditions were chosen to obtain a large increase in the in-plane lattice constant for subsequent growth of the highly strained active region. The DL was grown at the low temperature of 720 °C and the buffer was grown at 900 °C. Using these conditions along with an InGaN/GaN superlattice DSL, we achieved relaxed $In_{0.07}Ga_{0.93}N$.

The RSM of the layers taken around the $(\bar{1}\,\bar{1}\,2\,4)$ peak is shown in figure 4.2, showing the strain state of both the DSL and buffer clearly. The marked DSL peak corresponds to $In_{0.05}Ga_{0.95}N$ in tensile strain with the marked buffer peak corresponding to 100% relaxed $In_{0.07}Ga_{0.93}N$. The peaks appear somewhat broad and low-intensity, indicating that the crystal quality and surface morphology is likely quite poor.
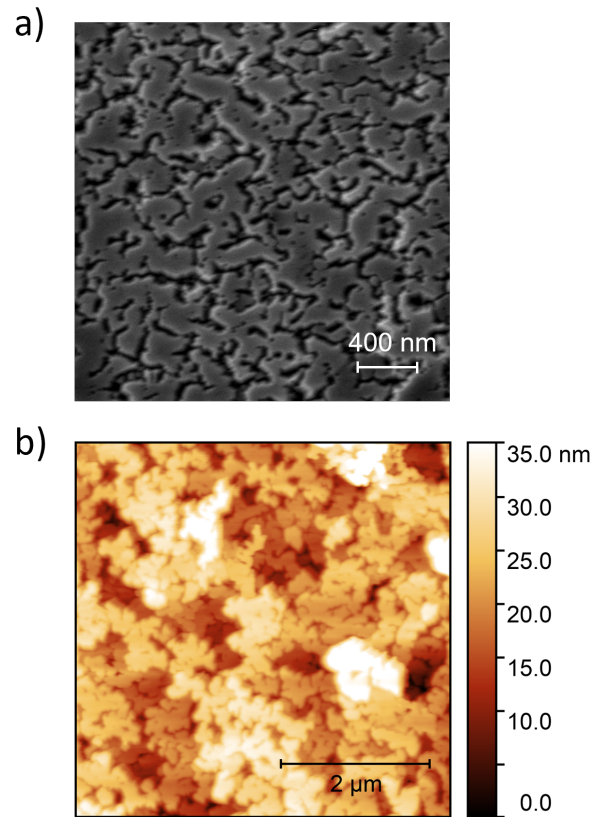
Figure 4.3: Scanning electron micrograph (a) and $5 \times 5\,\mu m^2$ atomic force micrograph of the InGaN buffer layer. Reproduced from Chan et al. with permission.[1]

The sample was then co-loaded with an identical structure grown with no indium precursor flow during the DL growth. This sample was meant to act as a wavelength reference to gauge the effect of the relaxation on electroluminescence. A simple 8-period $2.5\,nm/6\,nm$ InGaN/GaN MQW was grown at $870\,°C$, a temperature typical of blue or blue-green emission. Next, a $5\,nm$ p-AlGaN EBL, $30\,nm$ p-GaN and $20\,nm$ p^{++}GaN contact layer were grown.

Figure 4.3 shows the surface morphology as characterized by both SEM and AFM of the completed device on relaxed InGaN buffer. As expected from the previous samples

and the wide RSM peaks, the SEM and AFM show a high amount of pitting. This morphology is indicative of high dislocation density in the DSL and buffer layers, since pits will typically nucleate at threading dislocations.

4.1.2 Device results

Devices were then fabricated. First, 150 nm of ITO was deposited by electron-beam evaporation. The samples were then patterned by photolithography with $0.1\,mm^2$ mesas and the ITO was etched in $CH_4/H_2/Ar$ (MHA) reactive ion etch using AZ nLOF 2020 photoresist as a mask. Because polymer deposition occurs simultaneously to etching, the MHA etch was interleaved with O_2 descum steps to remove polymer buildup. The mesas were then formed with $SiCl_4$ reactive ion etching of the (AlIn)GaN layers to allows for low resistivity n-contacts to be formed in the etched field. The mesa depth was targeted to be around 280 nm to land in the middle of the Si-doped $In_{0.05}\,Ga_{0.95}\,N$ DSL and allow for good current spreading, while not etching through the thermally decomposed layer. This etch depth, however, fell short and landed between 30 and 50 nm into the InGaN buffer. Finally, 700 nm of Al, 100 nm of Ni and 700 nm of Au were deposited by electron beam evaporation and lifted off to form an n-contact and p-pad.

Final device performance parameters are depicted in figure 4.4. Spectra at current densities from 20 to $200\,A\,cm^{-2}$ are plotted in 4.4(a). Single peak emission is seen at all current densities below $200\,A\,cm^{-2}$. The peak wavelength and FWHM are plotted against current density in figure 4.4(b). The wavelength is very long at low current
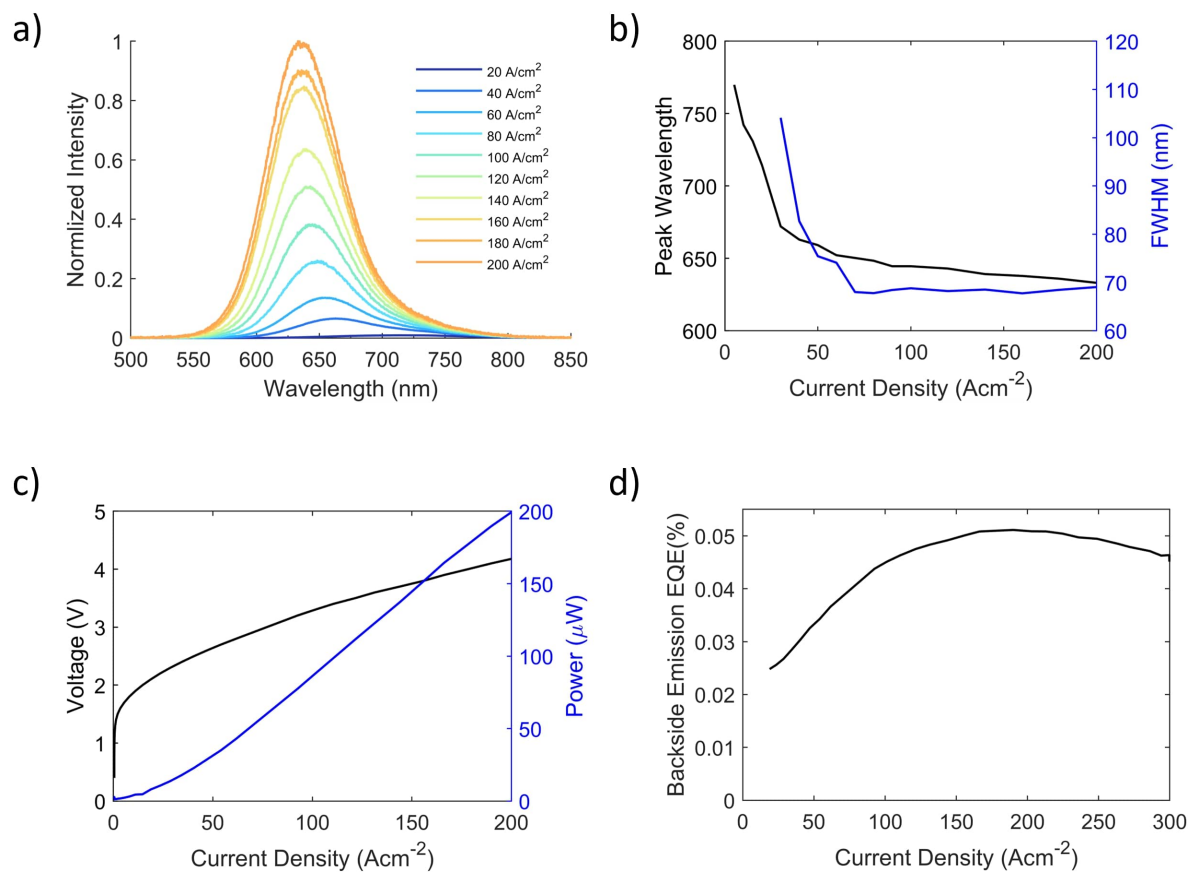
Figure 4.4: Fabricated LED performance: (a) electroluminescence spectra at various current densities, (b) peak wavelength and FWHM vs. current density, (c) light-current density-voltage curves, and (d) current dependent EQE as measured from the backside emission of the device. Reproduced from Chan et al. with permission.[1]

Figure 4.5: Photograph of device under operation at $50\,\mathrm{A\,cm^{-2}}$.

densities, well over $700\,\mathrm{nm}$ at $20\,\mathrm{A\,cm^{-2}}$. The emission quickly blueshifts and stabilizes

to a wavelength of $660\,\mathrm{nm}$ at $200\,\mathrm{A\,cm^{-2}}$ due to state filling effects and charge screening of

the polarization field in the quantum wells. The FWHM stabilizes at $69\,\mathrm{nm}$ from around

75 to $200\,\mathrm{A\,cm^{-2}}$. While this FWHM is not altogether unusual for long wavelength InGaN

LEDs, the width is at least in part due to poor current spreading. As mentioned before,

the mesa isolation etch landed shallow in the n-side of the device, leading to inadequate

current spreading on the n-side. This is readily apparent by photographing the device

under operating current as seen in figure 4.5. The area close to the n-contact (top and

center) appears significantly brighter and more yellow than the area farther away due to

increased current injection, leading to a broadening of the emission spectrum.

The LIV plotted in 4.4(c) shows very low turn-on voltage, near the photon energy.

The power increase is super-linear for the first $30\,\mathrm{A\,cm^{-2}}$ which is partially be accounted

for by the large blue-shifting of emission. The pitted surface morphology may be partially

responsible for both the low voltage and the non-linear increase in power. V-pits have
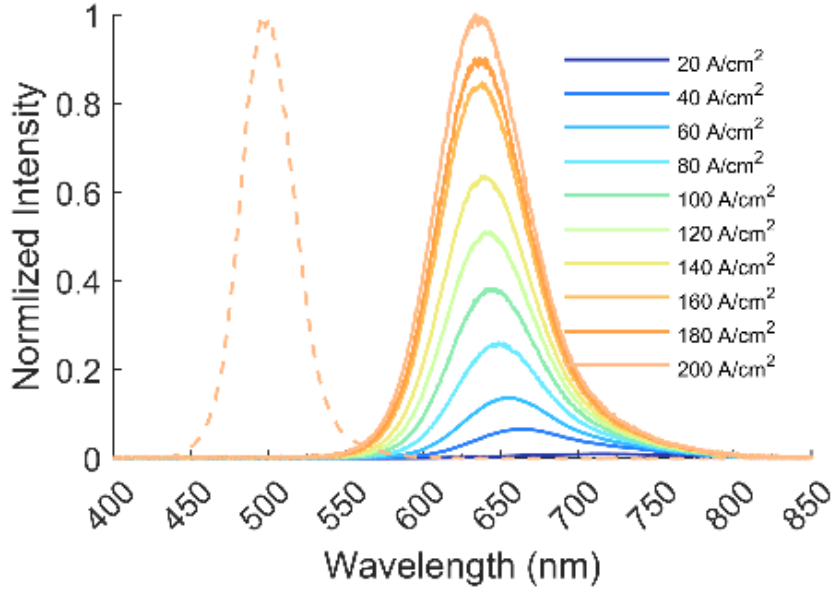
59

Figure 4.6: Spectra of fabricated LED without InGaN DL at $200\,\mathrm{A\,cm^{-2}}$ (dashed) and with decomposed InGaN DL at several current densities (solid).

been shown to actually aid in carrier injection to the quantum well while leading to an increased barrier for carriers to "see" the threading dislocations at which they nucleated.

Figure 4.4(d) shows a plot of the EQE as measured from a photodetector underneath the sample versus current density. The peak EQE of 0.05% occurred at $190\,\mathrm{A\,cm^{-2}}$. Packaging the device and measuring in the integrating sphere would lead to an increase in the EQE by at least a factor of 2-3×, but this number remains quite low. The regrowth interface was placed just below the quantum wells which can lead to additional defects in the active region which may explain the poor EQE of the devices.

The spectra of the fabricated LED is overlaid with the reference LED spectrum at $200\,\mathrm{A\,cm^{-2}}$ in figure 4.6. The reference LED was co-loaded for the quantum well and p-GaN regrowth and had an identical structure except for the omission of In precursor flow during the DL growth. The LED with the decomposed InGaN DL showed EL emission

a full 140 nm red-shifted as compared to the reference LED. As discussed in the prior chapter, this red-shift is likely due to a reduction in strain in the active region.

In this section, we demonstrated a true-red LED with exceptionally high active region growth temperature of 870 °C, a temperature that is typical of blue emission on our MOCVD reactors. This growth was enabled by the thermal decomposition of an InGaN underlayer allowing a $In_{0.07}Ga_{0.93}N$ buffer to 100% relax. While the 0.05% EQE as measured by backside emission was low due to the regrowth interface just below the active region and the very poor surface morphology, the 140 nm red-shift as compared to the reference sample is a compelling reason to pursue this growth technique.

4.2 Red micro-LEDs

Perhaps the most compelling application for high composition InGaN is for use in micro-LED displays. Because of this, red micro-LEDs were explored next using the technique of decomposing an InGaN underlayer to obtain a relaxed InGaN buffer layer.

4.2.1 Growth and structure

The epitaxial structure of the red micro-LED is shown in figure 4.7. This structure is similar to the red LED shown in the previous section with several changes. First, on top of a 5 μm GaN template, an additional 2.5 μm of GaN was grown to bury the regrowth interface. The InGaN DL was grown at at 720 °C and then capped with 4 nm of low temperature GaN. In this device, two InGaN/GaN superlattices were grown. The first one,
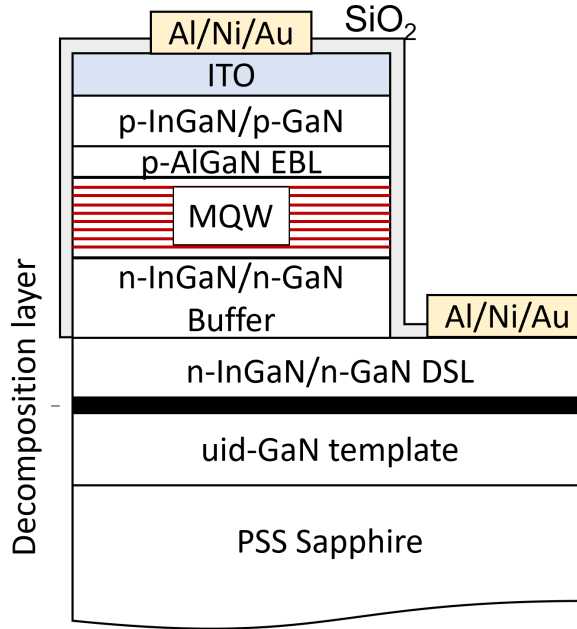
Figure 4.7: Spectra of fabricated LED without InGaN DL at $200\,\mathrm{A\,cm^{-2}}$ (dashed) and with decomposed InGaN DL at several current densities (solid).

acting in place of the previously discussed DSL, was a $7\,\mathrm{nm}/3\,\mathrm{nm}$ InGaN/GaN super-lattice grown at $950\,^{\circ}\mathrm{C}$ with an average composition around $\mathrm{In_{0.024}Ga_{0.976}N}$. The second superlattice was $20\,\mathrm{nm}/2\,\mathrm{nm}$ InGaN/GaN grown at $920\,^{\circ}\mathrm{C}$ with an average composition of $\mathrm{In_{0.049}Ga_{0.951}N}$. These layers form the strain relaxed template.

The active region consisted of an 8x MQW with $2.5\,\mathrm{nm}$ InGaN QWs and $7\,\mathrm{nm}$ GaN barriers grown at $820\,^{\circ}\mathrm{C}$. Compared to the LED presented in the previous section, this structure had a lower composition InGaN buffer layer. Because of this, a significantly lower active region growth temperature is needed to achieve red emission, $820\,^{\circ}\mathrm{C}$ as compared to $870\,^{\circ}\mathrm{C}$. The p-type layers consisted of a $10\,\mathrm{nm}$ p-AlGaN EBL followed by four periods of $20\,\mathrm{nm}/2\,\mathrm{nm}$ p-InGaN/p-GaN grown at $920\,^{\circ}\mathrm{C}$ that was nominally lattice-matched to the buffer. Finally, a $12\,\mathrm{nm}$ p^{++}-InGaN contact layer was grown. The p-type
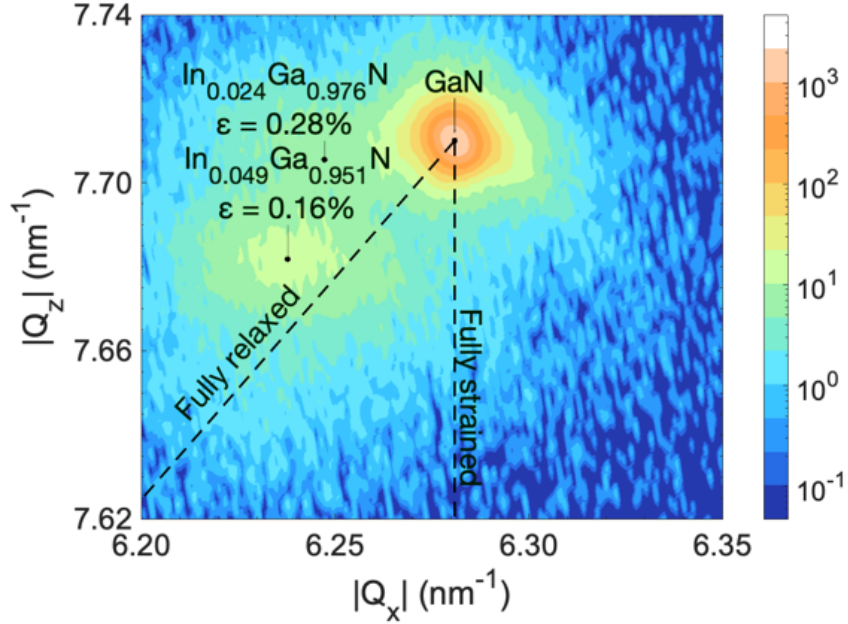
Figure 4.8: Reciprocal space map of the InGaN DSL and buffer layers taken around the $(\bar{1}\,\bar{1}\,2\,4)$ peak.

layers were primarily InGaN to address the concerns of possible p-GaN layer relaxation.

The epitaxial sample was then unloaded and characterized by HRXRD. An RSM taken around the off-axis $(\bar{1}\,\bar{1}\,2\,4)$ peak to characterize the strain-state of the InGaN/GaN DSL and buffer layers. As shown in figure 4.8, the both the InGaN/GaN DSL and buffer are in tensile strain and have extended past (to the left) of the fully relaxed line. Calculating the composition yields $In_{0.024}Ga_{0.976}N$ and $In_{0.049}Ga_{0.951}N$. Since the buffer is now in tensile strain, the term "degree of relaxation" no longer makes physical sense. The in-plane lattice constant, a, of the buffer is measured from the RSM to be $3.211\,\text{Å}$.

The surface of the sample was then characterized by SEM. The surface shows significant inverted pyramidal pits, but a significantly different morphology than displayed in the previous device. While pitted, the surface does not display the distinct trenches
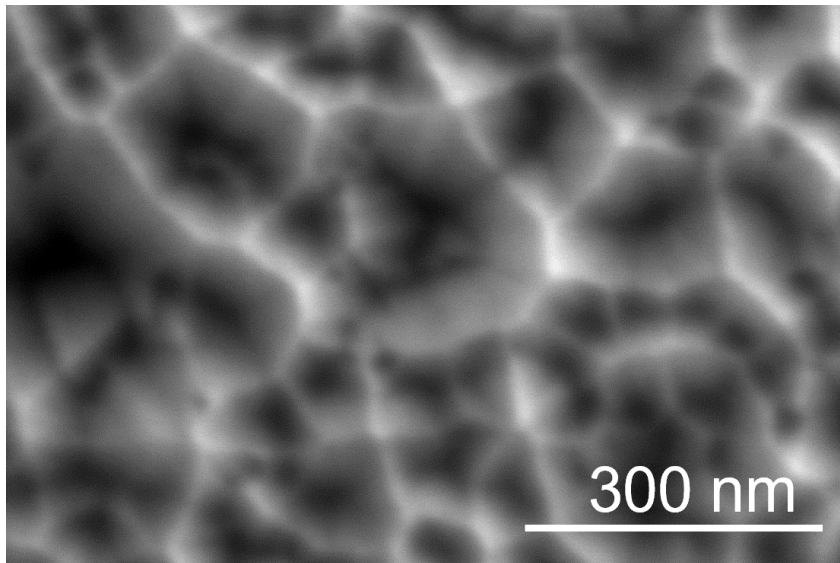
Figure 4.9: Scanning electron micrograph of the surface of the sample.

shown in figure 4.3(a). This may be due to the lower composition used in the DSL and Buffer as well as the InGaN p-layers.

4.2.2 Device fabrication

I have to thank Norleakvisoth Lim for much of the device fabrication and testing presented in this section.

LEDs were then fabricated from these epi-layers. A similar process flow as described before was used. However, to form micro-LEDs, pad metal had to be deposited off-mesa. This, as well as the increasing perimeter-to-area ratio necessitated two extra dielectric steps: one for pad metal isolation and one for sidewall passivation. First, 150 nm of ITO was deposited by electron beam evaporation. The sample was then patterned and ITO etched using an MHA reactive-ion etch. The mesas were etched self-aligned to the ITO

through the p-InGaN to land in the n-InGaN/GaN DSL layer.

To address the increased perimeter-to-area ratio of the small micro-LEDs, the sidewalls must be passivated. This was achieved with 25 nm of SiO_2 deposited by atomic layer deposition. This process has been shown to significantly decrease sidewall recombination leakage current.[2] Ideally, an additional wet surface treatment of UV-ozone, phosphoric acid and buffered HF would be done to remove sidewall etch damage before the passivation dielectric is deposited, however these processes are incompatible with ITO.

Next, a thicker, 225 nm pad-isolation dielectric is deposited and patterned by lift-off to allow for off-mesa pads. No omni-directional reflector (ODR) was used in this study. Typically, these are broad-band bragg reflectors used to prevent the light from interacting with the lossy metal pad metal. In a small micro-LED, the metal pad wrapping around the mesa covers a significant portion of the sidewall, leading to a large amound of light loss. However, this feature was omitted to simplify processing and allow for quicker device turn-around. Finally, a pad metal lithography with a buffered HF dip to remove the passivation dielectric was performed before lifting off 700/100/700 nm Al/Ni/Au pad and n-contact metals.

A fully fabricated device can be seen in figure 4.10(a). Both probe pads sit on top of the 225 nm isolation SiO_2 in the mesa etch field. This dielectric wraps onto the mesa underneath the p-pad to electrically isolate it and prevent shorting.

The devices suffered from a fabrication error with a very distinct burn-in behavior.

65
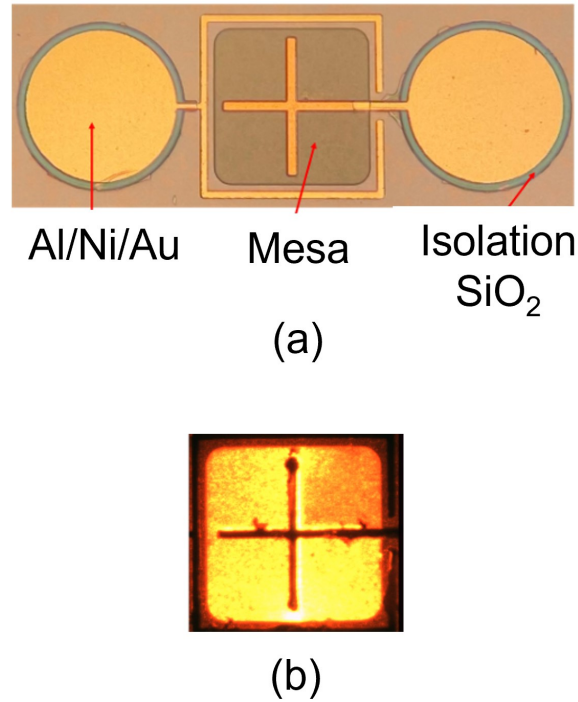
Figure 4.10: Microscope image of 100×100 µm^2 micro-LED (a) and device under operation (b).

The root cause remains unknown but this was potentially due to inadequate cleaning before ITO deposition or incomplete removal of the passivation oxide before pad deposition. Before burn-in, devices showed extremely poor p-side current spreading. After burning in, the smaller micro-LEDs sizes 40×40 µm^2 and under showed uniform emission while the larger devices still showed inadequate current spreading. The poor current spreading can be seen in a 100×100 µm^2 micro-LED shown in 4.10(b).

4.2.3 Device results

Several sizes of LEDs were fabricated. "Standard-sized" 0.1 mm^2 were included along with 100×100, 40×40, 20×20, 10×10 and 5×5 µm^2 micro-LEDs. Images of these
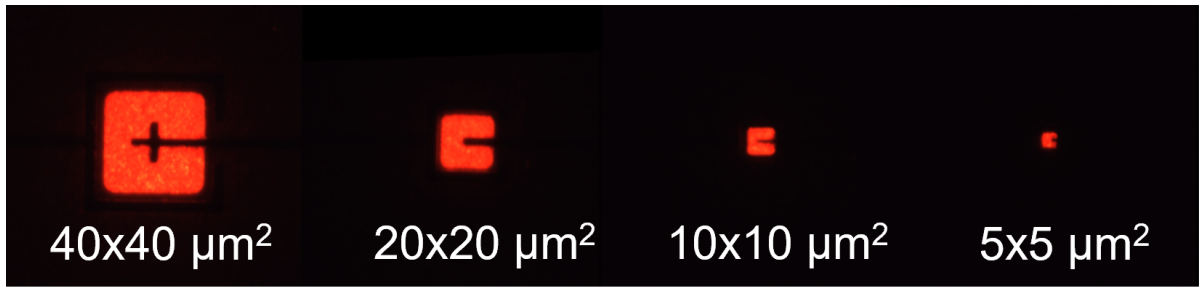
Figure 4.11: Microscope image of 40×40, 20×20, 10×10 and 5×5 µm^2 micro-LEDs in operation.

devices in operation are shown in figure 4.11. These sizes under 40×40 µm^2 showed very good uniformity and current spreading.

Current-voltage curves are shown for devices of various sizes in figure 4.12. Because of the fabrication issue described above, voltage curves were inconsistent across devices and device sizes. Some devices showed low voltage, just above those seen in the previous round of devices in figure 4.4, while others showed very high voltage with turn-ons well above $3\,\text{V}$.

Device performance parameters are plotted in figures 4.14 and 4.13. Figure 4.13 shows peak wavelength versus current density of the smallest and largest devices fabricated, 5×5 µm^2 and $0.1\,\text{mm}^2$ respectively. The wavelengths, as expected, are stable across device size with peak EQE in the 5×5 µm^2 LED occurring at $643\,\text{nm}$. Once again, a large blue-shifting of emission is observed at higher current densities. This is from state filling and polarization field screening as carriers are injected into the quantum wells.

The micro-LED measurement was courtesy of Norleakvisoth Lim using Professor Michael Gordon's lab. EQE versus current density of various micro-LED sizes are plotted
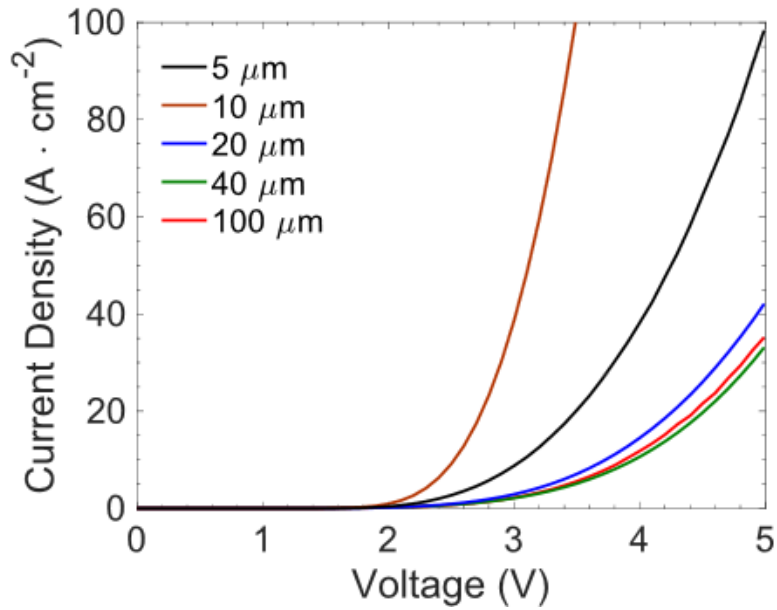
Figure 4.12: IV curves of several device with various sizes. Because of a fabrication issue, voltage spread was quite wide and did not follow a consistent trend.
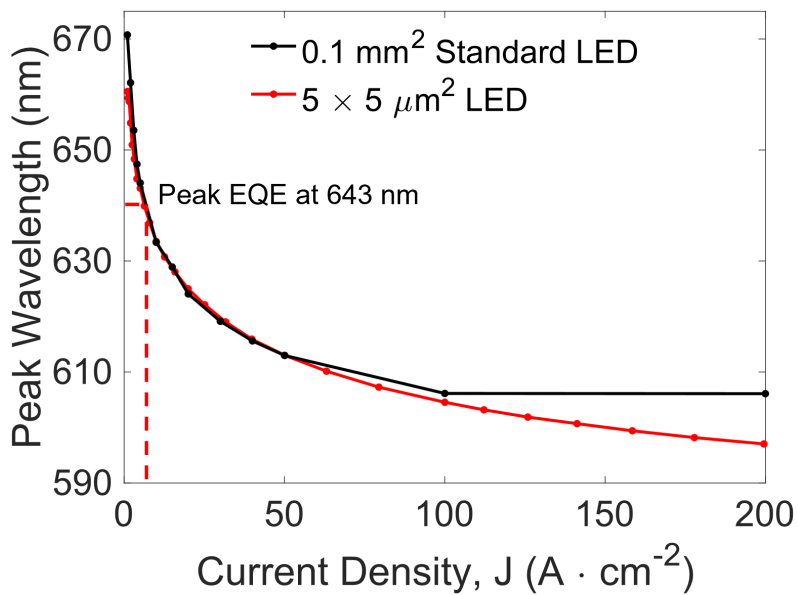

Figure 4.13: Wavelength versus current density of $5 \times 5\mu m^2$ and 0.1 mm LEDs.

in figure 4.14. This EQE measurement was performed on-wafer by measuring top-side emission. The sample was placed on a stage an integrating sphere placed over the top. Probes feeding into the integrating sphere were used to inject current. The devices were not packaged or fully encapsulated by the integrating sphere, reducing the measured EQE significantly.

Typically, peak EQE drops with size due to increasing perimeter-to-area ratio due to a relative increase in sidewall recombination.[3]–[5] However, with proper ALD-deposited passivation, size independence down to sizes less than 5×5 µm^2 have been demonstrated in both blue and green wavelengths. [2], [6] More recently, size independence has also been shown in red. [7] As the InGaN composition of the quantum wells increases to the red regime, the surface recombination velocity decreases meaning the need for high quality passivation and the size dependence of devices decreases. The reason for an increase in efficiency needs more investigation, but may be due, in part, to an increase in light extraction efficiency for smaller sized devices. It may also be partially due to a measurement artifact with better color uniformity in the smaller LEDs allowing more light to be captured in the spectrometer's bandwidth.

The peak EQE of the 5×5 µm^2 was over 0.45%. This number is quite high considering the measurement geometry (top-side emission only) and lack of ODR under the p-pad metal. Previously, one of the highest reported EQE of a red micro-LED on relaxed InGaN was by Pasayat et al. using an InGaN buffer relaxed using the nanoporous technique. [8] Their 6×6 µm^2 LED showed a peak of 0.2% EQE measured on-wafer at a wavelength of
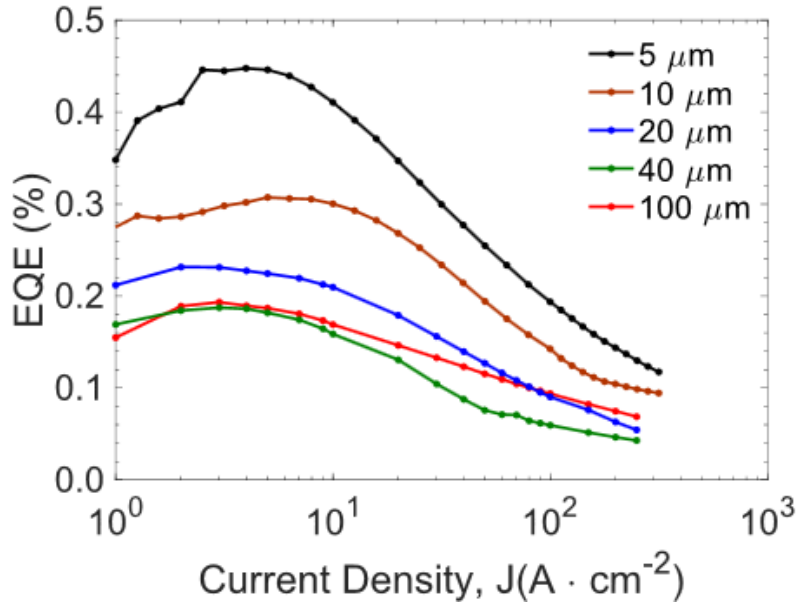
Figure 4.14: Size-dependent EQE measured on-wafer from top-side emission versus current density of fabricated micro-LEDs. Measurement courtesy of N. Lim.

632 nm with an ODR to reduce metal absorption. White et al. showed an EQE of 0.83% of an 80×80 µm² fully packaged LED at 610 nm grown on the InGaNOS substrate by Soitec.[9]

The 5×5 µm² LED reported here showed a forward voltage at $50 \, \text{A cm}^{-2}$ of 4.1 V, over a volt higher than the 10×10 µm² LED and almost 1.5 V higher than the $0.1 \, \text{mm}^2$ device shown in figure 4.4. As discussed earlier, fabrication issues with the p-side contact lead to a large burn-in dependence of IV curves, as well as highly non-uniform IV characteristics device-to-device across the sample. Despite this, the voltage of the 5×5 µm² device remains in-line with the report of White et al. at around 4 V at $50 \, \text{A cm}^{-2}$.[9] The 10×10 µm² LED, with under 3 V at $50 \, \text{A cm}^{-2}$, shows significantly lower voltage than the micro-LED reported by Pasayat et al. (3.5 V) and is on par with the report by Iida

et al. of low forward voltage red LEDs (3 V). [8], [10]

4.3 Chapter summary

Red LEDs are demonstrated on the InGaN buffers relaxed with an InGaN DL as presented last chapter. The resulting LEDs show very low forward voltage and a 140 nm red-shift as compared to a co-loaded reference with no DL. The EQE remained was quite low, partly due to a regrowth interface just below the quantum wells in order to co-load a reference sample.

Finally, red micro-LEDs were grown and fabricated with similar or better performance as compared to other relaxation methods. Recent reports of red InGaN-based LEDs are tabulated in table 4.1.

The reports are sorted by those using relaxed InGaN buffer layers (rows 1-7) and those conventionally grown strained to GaN (rows 8-11). Looking at the peak EQE column it is apparent that, even accounting for the lack of packaging by a several-fold factor, devices on relaxed buffers are lagging those grown conventionally. This is not necessarily unexpected, given that the reported relaxed buffers (by decomposition layer, nanoporous layer, or InGaNOS substrate) are very recent developments.

Looking at the devices on relaxed InGaN buffers, the first four are relaxed with an InGaN DL. The top two are results first reported here with the next two being initial results focused on the low forward voltage and high growth temperatures using this method. The 5×5 and 10×10 µm^2 micro-LEDs reported here show higher peak EQE

Authors	Report	λ (nm)	Peak EQE (%)	Device size (µm²)	V_F at 50 A cm^{-2}	Relaxed InGaN	a (Å)
Chan et al.	–	643	0.46 (W)	5×5	4.1	Yes*	3.211
Chan et al.	–	643	0.31 (W)	10×10	3.0	Yes*	3.211
Wong et al.	2022[11]	637	0.25 (P)	20×20	2.2	Yes*	3.211
Chan et al.	2021[1]	633	0.05 (W)	10^5	2.6	Yes*	3.213
Pasayat et al.	2021[8]	632	0.2 (W)	6×6	3.5	Yes†	3.197
White et al.	2021[9]	610	0.83 (P)	80×80	3.8	Yes‡	3.205
Dussaigne et al.	2021[12]	625	0.14 (W)	25π	6.8	Yes‡	3.205
Dussaigne et al.	2020[13]	616	0.09 (W)	50×50	–	Yes‡	3.207
Li et al.	2022[14]	620	4.5 (P)	60×60	5.0	No	3.189
Li et al.	2021[7]	611	2.6 (P)	20×20	3.9	No	3.189
Iida et al.	2020[10]	665	0.19 (P)	650×250	3.0	No	3.189
Hwang et al.	2014[15]	629	2.9 (P)	460×460	5.0	No	3.189

(W) EQE measured on wafer

(P) EQE measured from packaged LED

* Buffer relaxed using decomposition layer

† Buffer relaxed using a nanoporous layer

‡ Device grown on Soitec InGaNOS substrate

Table 4.1: Reports presented here and other recent reports of red InGaN-based LEDs.

than all but the report by White et al. using the InGaNOS substrate.[9] White et al. reported data from a packaged LED with and omnidirectional reflector under the pad to prevent absorption by in the metal. Packaging of a small micro-LED results in a conservative 3x improvement in measured EQE. [8]

The forward voltage at $50\,\text{A cm}^{-2}$ is also tabulated. As mentioned before, a processing error unfortunately left the micro-LEDs reported here with somewhat higher and inconsistent voltage. The other two reports by Wong et al. and Chan et al. using an InGaN DL show extremely low forward voltage in comparison, likely due to injection from v-defects nucleated in the InGaN buffer and lack of AlGaN in the active region.[1], [11] The results using an InGaN DL show much lower voltage than the other red LEDs, including those that were conventionally grown.

References

[1] P. Chan, V. Rienzi, N. Lim, H. M. Chang, M. Gordon, S. P. DenBaars, and S. Nakamura, "Demonstration of relaxed InGaN-based red LEDs grown with high active region temperature," *Appl. Phys. Express*, vol. 14, no. 10, pp. 3–7, 2021. DOI: `10.35848/1882-0786/ac251d`.

[2] M. S. Wong, C. Lee, D. J. Myers, D. Hwang, J. A. Kearns, T. Li, J. S. Speck, S. Nakamura, and S. P. Denbaars, "Size-independent peak efficiency of III-nitride micro-light-emitting-diodes using chemical treatment and sidewall passivation," *Appl. Phys. Express*, vol. 12, no. 9, p. 097 004, 2019. DOI: `10.7567/1882-0786/ab3949`.

[3] P. Tian, J. J. D. McKendry, Z. Gong, B. Guilhabert, I. M. Watson, E. Gu, Z. Chen, G. Zhang, and M. D. Dawson, "Size-dependent efficiency and efficiency droop of blue ingan micro-light emitting diodes," *Appl. Phys. Lett.*, vol. 101, no. 23, p. 231 110, 2012. DOI: `10.1063/1.4769835`.

[4] D. Hwang, A. Mughal, C. D. Pynn, S. Nakamura, and S. P. DenBaars, "Sustained high external quantum efficiency in ultrasmall blue III–nitride micro-LEDs," *Appl. Phys. Express*, vol. 10, no. 3, p. 032 101, 2017. DOI: `10.7567/apex.10.032101`.

[5] F. Olivier, S. Tirano, L. Dupré, B. Aventurier, C. Largeron, and F. Templier, "Influence of size-reduction on the performances of gan-based micro-leds for display

application," *J. Lumin.*, vol. 191, pp. 112–116, 2017. DOI: https://doi.org/10.1016/j.jlumin.2016.09.052.

[6] J. M. Smith, R. Ley, M. S. Wong, Y. H. Baek, J. H. Kang, C. H. Kim, M. J. Gordon, S. Nakamura, J. S. Speck, and S. P. Denbaars, "Comparison of size-dependent characteristics of blue and green InGaN microLEDs down to 1 μ m in diameter," *Appl. Phys. Lett.*, vol. 116, no. 7, p. 071102, 2020. DOI: 10.1063/1.5144819.

[7] P. Li, H. Li, H. Zhang, C. Lynsky, M. Iza, J. S. Speck, S. Nakamura, and S. P. Denbaars, "Size-independent peak external quantum efficiency (¿2%) of InGaN red micro-light-emitting diodes with an emission wavelength over 600 nm," *Appl. Phys. Lett.*, vol. 119, no. 8, 2021. DOI: 10.1063/5.0061940.

[8] S. S. Pasayat, C. Gupta, M. S. Wong, R. Ley, M. J. Gordon, S. P. Denbaars, S. Nakamura, S. Keller, and U. K. Mishra, "Demonstration of ultra-small (<10 μm) 632 nm red InGaN micro-LEDs with useful on-wafer external quantum efficiency (>0.2%) for mini-displays," *Appl. Phys. Express*, vol. 14, no. 1, p. 011004, 2021. DOI: 10.35848/1882-0786/abd06f.

[9] R. C. White, H. Li, M. Khoury, C. Lynsky, M. Iza, S. Keller, D. Sotta, S. Nakamura, and S. P. DenBaars, "Ingan-based microled devices approaching 1% eqe with red 609 nm electroluminescence on semi-relaxed substrates," *Crystals*, vol. 11, no. 11, 2021. DOI: 10.3390/cryst11111364.

[10] D. Iida, Z. Zhuang, P. Kirilenko, M. Velazquez-Rizo, and K. Ohkawa, "Demonstration of low forward voltage InGaN-based red LEDs," *Appl. Phys. Express*, vol. 13, no. 3, p. 031 001, 2020. DOI: 10.35848/1882-0786/ab7168.

[11] M. S. Wong, P. Chan, N. Lim, H. Zhang, R. C. White, J. S. Speck, S. P. Denbaars, and S. Nakamura, "Low Forward Voltage III-Nitride Red Micro-Light-Emitting Decomposition Layer," *Crystals*, pp. 4–9, 2022.

[12] A. Dussaigne, P. Le Maitre, H. Haas, J. C. Pillet, F. Barbier, A. Grenier, N. Michit, A. Jannaud, R. Templier, D. Vaufrey, F. Rol, O. Ledoux, and D. Sotta, "Full InGaN red (625 nm) micro-LED (10 μm) demonstration on a relaxed pseudo-substrate," *Appl. Phys. Express*, vol. 14, no. 9, 2021. DOI: 10.35848/1882-0786/ac1b3e.

[13] A. Dussaigne, F. Barbier, B. Damilano, S. Chenot, A. Grenier, A. M. Papon, B. Samuel, B. Ben Bakir, D. Vaufrey, J. C. Pillet, A. Gasse, O. Ledoux, M. Rozhavskaya, and D. Sotta, "Full ingan red light emitting diodes," *J. Appl. Phys.*, vol. 128, no. 13, p. 135 704, 2020. DOI: 10.1063/5.0016217.

[14] P. Li, H. Li, H. Zhang, Y. Yang, M. S. Wong, C. Lynsky, M. Iza, M. J. Gordon, J. S. Speck, S. Nakamura, and S. P. DenBaars, " Red InGaN micro-light-emitting diodes (>620 nm) with a peak external quantum efficiency of 4.5% using an epitaxial tunnel junction contact," *Appl. Phys. Lett.*, vol. 120, no. 12, p. 121 102, 2022. DOI: 10.1063/5.0086912.

[15]   J. I. Hwang, R. Hashimoto, S. Saito, and S. Nunoue, "Development of InGaN-based red LED grown on (0001) polar surface," *Appl. Phys. Express*, vol. 7, no. 7, pp. 1–4, 2014. DOI: 10.7567/APEX.7.071003.

Chapter 5

Indium nitride: towards longer wavelengths

In this chapter we will move to wavelengths beyond red and explore InN quantum dot and dash growth on semi-polar $(20\bar{2}1)$ and $(20\bar{2}\bar{1})$ planes. After characterizing the InN layers, efforts are made to advance towards a first electrically injected, InN-based near-infrared LED. This project had many growth challenges. The thermal instability of InN necessitates a very unconventional device design as we will discuss. P-side down devices with buried tunnel junction p-contacts are demonstrated in blue, a first step towards an electrically injected InN-based devices.

Because of the high lattice mismatch between InN and GaN, high indium content films are challenging to grow. Additionally, the sublimation temperature of InN is around $550\,°\text{C}$. This temperature is much colder than typical GaN growth temperatures by

MOCVD, between 900 °C and 1200 °C. The discrepancy in growth temperature leads to a thermal budgeting issue when growing In-rich devices. After the growth of the high composition InGaN or InN layers, the remainder of the device must be grown relatively cold and kept to a relatively short growth time. Elevated temperatures with respect to the growth temperatures of the active layers can lead to indium segregation and interdiffusion of InGaN layers with neighboring layers as well as the propagation of formation of defects on certain crystal planes.[1]–[4] Typical Ga-rich InGaN devices also suffer from these issues, as even low-composition InGaN alloys must be grown at temperatures below those which are ideal for growth of GaN. As InGaN composition (or wavelength) increases, these problems worsen.

Additionally, the low temperature growth required to grow high composition InGaN or InN layers can lead to problems. At low temperatures, precursors suffer from poor cracking efficiencies. After cracking, adatoms on the surface have low mobilities which can lead to defect formation. Finally, films grown at low temperature show increased impurity concentrations, including carbon from the cracked precursors.[5]

The large lattice mismatch between InN and GaN naturally leads to the formation of quantum dots when InN or In-rich InGaN is grown on GaN. These quantum dots are of particular interest in the In-rich regime anyway, since they are less sensitive to defects formed when growing high strain In-rich alloys and during the subsequent low temperature growth required by the thermal budgeting problem. Once a carrier is injected into a quantum dot, the carrier is confined not only in the transverse direction as with a quan-

tum well, but also in the lateral direction in the plane of the growth. Injected carriers are not able to "see" defects or dislocations laterally removed in the active region. In the case of a quantum well, there is no barrier to lateral diffusion and carriers are free to distribute in-plane and recombine at these defects or dislocations. The decrease in defect sensitivity can lead to higher internal quantum efficiencies in defective materials than would otherwise be possible with quantum wells.

Quantum dot active regions have been used in laser diodes in other material systems. Devices with quantum dot active regions display higher peak gain leading to lower threshold current densities as well as lower temperature sensitivities.[6], [7]

5.1   InN in literature

InN quantum dots with near-infrared photoluminescence have been grown by MBE and MOCVD on c-plane GaN. Growth on both the metal-polar [8]–[12] and the N-polar [13]–[16] surfaces has been explored, here at UCSB's SSLEEC and elsewhere. There has been particular interest in the nitrogen polar plane here at UCSB. Owing to the p-down device design that will later discuss, growing an InN device on the N-polar plane maintains the polarization fields typically seen in Ga-polar c-plane devices. In addition to c-plane, InN quantum dots have been shown to grow on the m-plane side facets of nanowires.[17]

InGaN quantum dots are also well-studied with literature reports of emission ranging from the green to near-infrared wavelengths. These have also been explored on a variety of planes including c-plane[18], semipolar $(1\,1\,\bar{2}\,2)$[19] and non-polar a-plane[20].
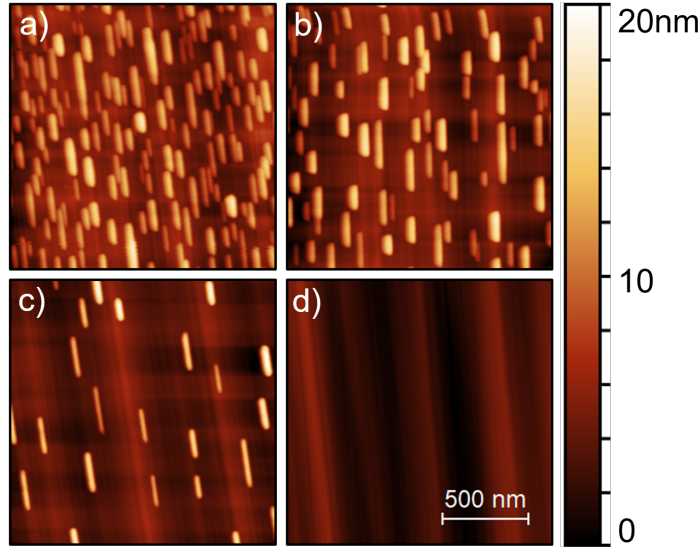
Figure 5.1: 1.5 μm × 1.5 μm Atomic force micrographs of uncapped $(20\bar{2}\bar{1})$ InN quantum dashes grown for 90 s on GaN at (a) 550 °C, (b) 575 °C, (c) 600 °C and (d) 625 °C. Reproduced from Chan et al. with permission.[21]

5.2 $(20\bar{2}\bar{1})$ InN quantum dashes

To begin, the $(20\bar{2}\bar{1})$ crystal plane was explored. All growths in these studies were done by MOCVD on bulk $(20\bar{2}\bar{1})$ GaN substrates. The initial studies consisted of varying the InN growth temperature and time to select optimal conditions and observe growth mechanisms. First, an InN temperature series was grown where InN layers were grown for 90 s from 550 °C to 625 °C in increments of 25 °C with all other conditions being the same. Then, additional samples were grown at 600 °C with InN growth times varied, with growth times of 30 s, 60 s, 150 s and 210 s.

The InN layers were grown with a trimethylindium flow-rate of 7 sccm and an ammonia flow-rate of 1.6 slm in nitrogen carrier gas. They were grown on 1.2 μm n-GaN layers doped with roughly 2×10^{18} cm^{-3} with trimethylgallium as the Ga precursor.
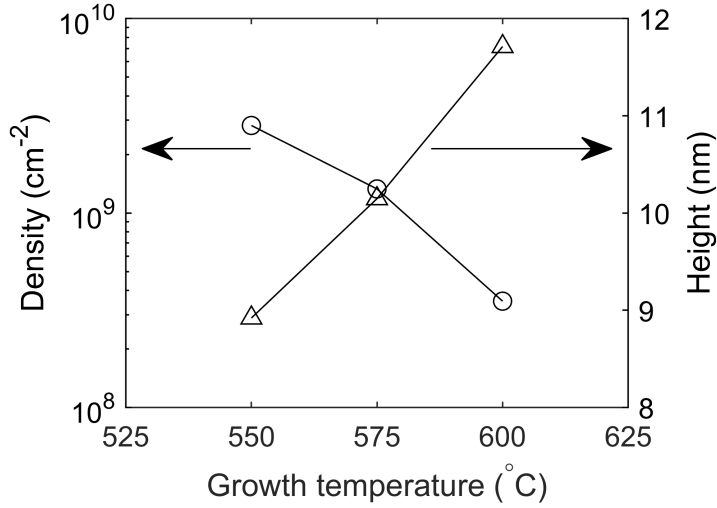
Figure 5.2: $(20\bar{2}\bar{1})$ InN quantum dash density and height as a function of growth temperature as measured by AFM

.

Using AFM, we can observe the surface morphology of the samples after InN growth. Figure 5.1 shows $1.5\,\mu m \times 1.5\,\mu m$ AFM scans of the uncapped InN from the growth temperature series in order of increasing growth temperature. As growth temperatures increase, the density of the dashes decreases. The increased temperature increases the In adatom desorption from the substrate, decreasing the nucleation rate of the InN dashes. At $625\,°C$, depicted in figure 5.1(d), no dash nucleation is seen and the AFM shows the underlying nanofaceted surface morphology of the $(20\bar{2}\bar{1})$ GaN template. The increasing temperature, while increasing desorption, also increases the adatom mobility. This means that adatoms have energy to travel farther across the surface and find the edge of a nucleated InN island. Because of this, higher temperature growth shows taller but sparser dashes. This trend is shown in figure 5.2. Because dashes were only observed at edges of defects at $626\,°C$, no data is plotted.
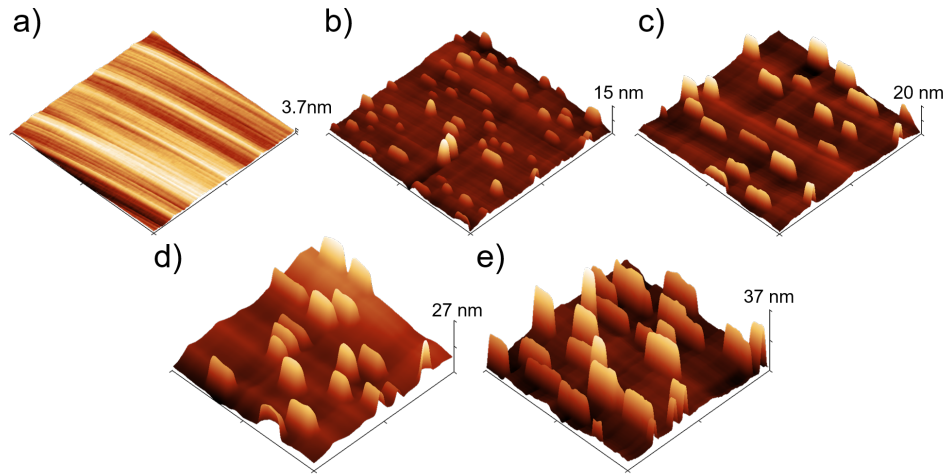
81

Figure 5.3: $1.5\,\mu m \times 1.5\,\mu m$ Atomic force micrographs of uncapped $(2\,0\,\overline{2}\,\overline{1})$ InN quantum dashes grown on GaN for (a) $30\,s$, (b) $60\,s$, (c) $90\,s$, (d) $150\,s$ and (e) $210\,s$. Reproduced from Chan et al. with permission.[21]

Next, the growth temperature was held constant at $600\,°C$ and the growth time was changed from $30\,s$ to $210\,s$. AFM scans of this series are plotted in figure 5.3. In figure 5.3(a) with $30\,s$ of growth time, no InN growth is seen and the underlying semipolar template morphology is visible. While no growth is observed, one cannot make the assumption that no growth occurs. After InN growth, no capping layer was deposited and significant desorption may occur during reactor cooldown. As the InN growth time increases, figure 5.3(b)-(e), the dashes increase significantly in length and height.

One additional sample was grown at $550\,°C$ for $10\,min$. This sample was included to show the effect of a long growth time on densely nucleated InN. An AFM scan of this sample is shown in figure 5.4(d). While AFM is a good measure of quantum dash height and density, the microstructure of the dashes is more readily visible using scanning electron microscopy (SEM). Plan view, 45 degree tilted and cross-sectional SEM
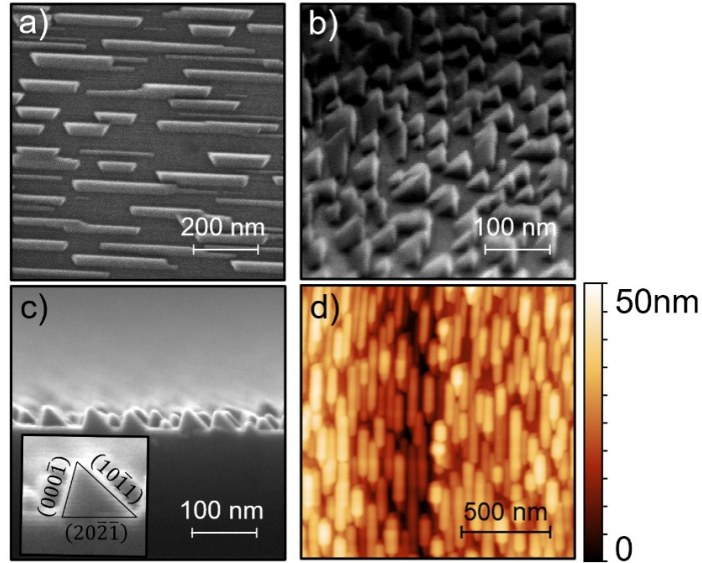
82

Figure 5.4: Plan view (a), 45 degree tilted (b), cross-sectional (c) SEM and 1.5 µm × 1.5 µm AFM of uncapped growth of 10 min of InN grown on $(2\,0\,\bar{2}\,\bar{1})$ GaN. Reproduced from Chan et al. with permission.[21]

are shown in 5.4(a)-(c). In the plan view, figure 5.4(a), faceting on the InN dashes is apparent showing single crystal growth. The cross-sectional SEM in figure 5.4(c) shows the triangular cross-section of the InN. By measuring the angle of the facets, we find the dashes to be formed by the $(2\,0\,\bar{2}\,\bar{1})$ substrate plane, $(0\,0\,0\,\bar{1})$ and $(1\,0\,\bar{1}\,1)$ crystal planes.

Room temperature photoluminescence (RT-PL) spectra of these samples were taken using a a liquid nitrogen cooled InGaAs detector. The pump was a 785 nm laser focused through a 10x microscope objective lens. The sample emission was collected thorugh the same lens. The spectra for the growth time series grown at 600 °C as well as the sample grown at 550 °C for 10 min is shown in figure 5.5. The notch at 1386 nm was present on all measured samples, as well as a much brighter InGaAsP reference sample, and is suspected to be an artifact of the detector. A laser harmonic was present at 1570 nm and
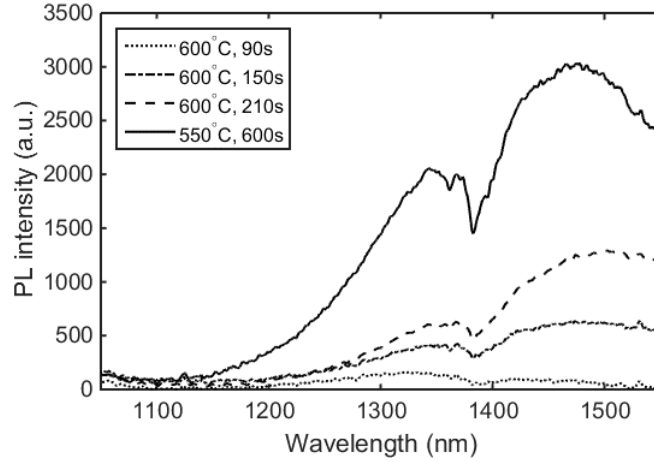
Figure 5.5: Room temperature photoluminescence of uncapped $(2\,0\,\overline{2}\,\overline{1})$ GaN InN quantum dashes. Reproduced from Chan et al. with permission.[21]

the cooled detector sensitivity rolled off above 1550 nm so no data is shown past 1550 nm.

Looking at the traces for samples grown at 600 °C in figure 5.5, increasing growth time yields both an increase in PL intensity as well as a red-shift of the peak wavelength. The increase in PL intensity is due to an increase in the emitting InN volume, while the red-shift is consistent with a decrease in confinement in the taller InN dashes. The sample grown at 550 °C for 10 min showed significantly stronger PL intensity with a peak wavelength of 1480 nm.

The PL intensities measured were quite weak. The integration times required for clear spectra were on the order of 10 s or 100 s (100 s plotted in figure 5.5). Because of this, the samples with InN growth times of 30 s and 60 s were omitted.

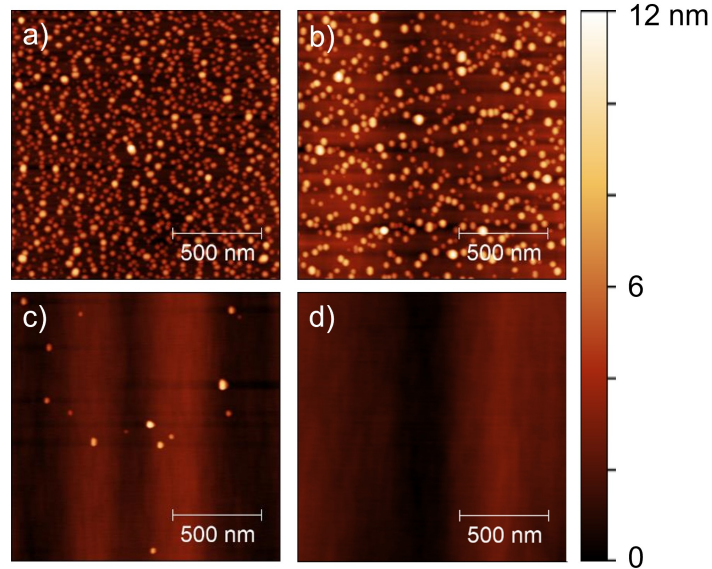Figure 5.6: $1.5\,\mu\text{m} \times 1.5\,\mu\text{m}$ Atomic force micrograph of uncapped $(20\bar{2}1)$ InN quantum dots grown for $90\,\text{s}$ on GaN at (a) $550\,°\text{C}$, (b) $575\,°\text{C}$, (c) $600\,°\text{C}$ and (d) $625\,°\text{C}$
.

5.3 $(20\bar{2}1)$ InN quantum dots

Next, the $(20\bar{2}1)$ semipolar plane was briefly explored. The temperature series was repeated with the same InN growth conditions and temperatures of $550\,°\text{C}$, $575\,°\text{C}$, $600\,°\text{C}$ and $625\,°\text{C}$. AFM scans of the resulting structures are shown in 5.6. On this crystal plane, the InN forms dots rather than dashes. While more data is needed, this likely has to do with the morphology of the underlying GaN template. In the case of $(20\bar{2}\bar{1})$, the template showed sharp nanofaceting as seen in figure 5.1(d). In contrast, the template of $(20\bar{2}1)$ shows longer order undulations as shown in figure 5.6(d).

The quantum dot density and average height is plotted in figure 5.7. As before on $(20\bar{2}\bar{1})$, the density decreases while the height increases with growth temperature. Again, this is a result of the higher In adatom desorption rate and increased mobility as

85
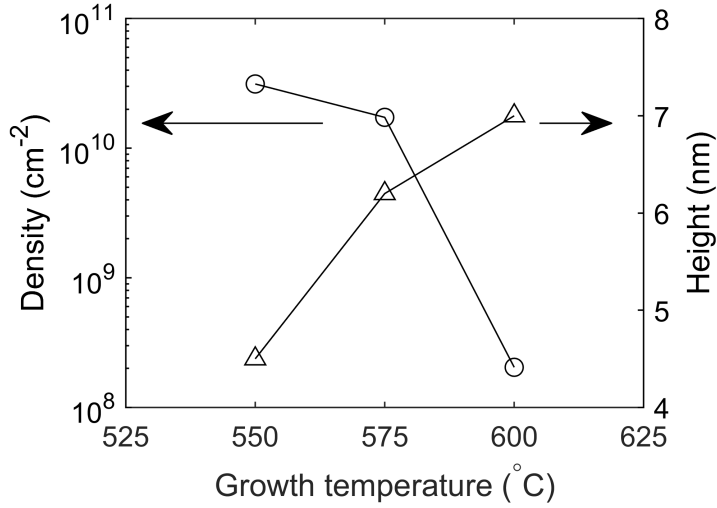
Figure 5.7: $(20\bar{2}1)$ InN quantum dot density and height as a function of growth temperature as measured by AFM

.

the growth temperature is increased.

5.4 Capping InN

As demonstrated in the previously shown $(20\bar{2}\bar{1})$ and $(20\bar{2}1)$ temperature series in figures 5.1 and 5.6 respectively, the InN is quite sensitive to growth temperature. Capping the $(20\bar{2}\bar{1})$ dashes makes this even more apparent: Three samples were grown consisting of 10 min of InN growth at 550 °C, the same growth conditions as shown in figure 5.4, and a 30 nm GaN cap. One sample was capped with a continuously grown layer with a growth rate of $0.33\,\text{Å}\,\text{s}^{-1}$ and one with a flow modulated epitaxy (FME) growth scheme at 550 °C. The third sample was capped by FME with 15 nm grown at 550 °C and an additional 15 nm grown at 650 °C. A final reference sample was left un-capped.

FME is a growth technique where the group-III precursor, in this case triethylgallium,
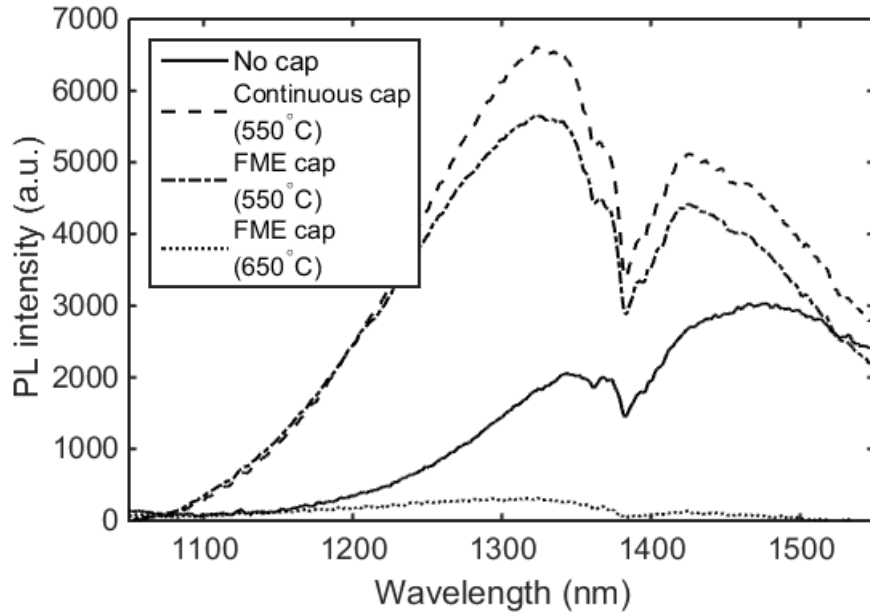
Figure 5.8: Photoluminescence spectra of $(2\,0\,\overline{2}\,\overline{1})$ InN quantum dashes capped with 30 nm of GaN grown at various conditions. Reproduced from Chan et al. with permission.[21]

is pulsed. This pulse introduces Ga adatoms to the surface and allows extra time for the adatoms to migrate across the surface. FME was used to address concerns of the low growth temperature lowering adatom mobility leading to to poor morphology and high impurity incorporation. The growth rate of the FME GaN was calibrated by high-resolution x-ray diffraction (HR-XRD) to be 0.2 Å per cycle. Each cycle consisted of a 5 s group-III pulse with 5 s flow ramp at both ends and a 9 s wait for a total of 24 s.

Figure 5.8 shows the PL spectra results from these growths. As expected, the uncapped sample shows similar emission as the 550 °C, 600 s trace in figure 5.5 since it shares the same growth conditions. The peak emission intensity occurred at 1480 nm. Both samples capped at 550 °C showed a significant increase in peak intensity and blue-

shifting of emission spectra. The increase in intensity is likely attributed to a removal of lossy InN-air surface states as well as an increase in carrier concentration in the InN layers from impurities incorporated in the cold, GaN cap growth. The sample with the FME-grown cap shows slightly weaker PL intensity. This could be due to the significantly increased growth time as well as fewer impurities in the GaN cap. The blue-shift is consistent with an increase in confinement and increase in compressive strain induced from the GaN capping layers. The sample grown partially at 650 °C shows almost no PL, underlining the temperature sensitivity of InN.

5.5   Towards electrically injected InN devices

Moving towards an electrically injected InN device presents many challenges. The temperature sensitivity of the InN requires a strict thermal budget be observed during the growth of the active layers and all subsequent layers. This informs a very non-traditional device design of p-side down. High conductivity Mg-doped p-GaN is already challenging to grow in normal temperature regimes. At the low temperatures required to preserve the InN layers, however, it is practically impossible due to the increased impurity incorporation, particularly carbon which can act as a donor to compensate the Mg.

Figure 5.9 shows the proposed p-down InN device design. Starting with the $\{2\,0\,\overline{2}\,\overline{1}\}$ substrate, an n-GaN template is grown to bury the regrowth interface. An n^{++} and p^{++} layers are then growth to form a tunnel junction. The tunnel junction is used in order to more easily form a good electrical contact to the p-side of the device. Since p-GaN

is not very conductive, it is important to make contact to the p^{++} layer. In the p-down device design, it would be difficult to control the etch in order to make contact to this layer. Additionally, while low-resistivity contacts to plasma-etched n-GaN are possible with a $SiCl_4$ pretreatment, this is not possible in p-type layers. Because of the p-down design, this tunnel junction is grown opposite of the typical p-n configuration meaning there is not an issue with magnesium memory effect blurring the junction. Further work optimizing this backward tunnel-junction configuration would be interesting but in this work a best-attempt at doping and growth conditions were made and not explored further.

One alternative to a tunnel junction would be to flip-chip bond the device and use a photoelectrochemical etch to etch through a sacrificial quantum well just below the p^{++} layer. This design would be more ideal as it would expose the p^{++}GaN using a wet etch for subsequent activation and contact formation. However, this complicates the processing significantly on top of an already complicated epitaxial growth, so was not attempted in this work and left for the future.

The bulk p-GaN is then grown along with a p-AlGaN electron blocking layer. This is followed by the active region consisting of either a single or several layers of InN and GaN. Finally, the bulk n-type and n^{++}GaN contact layers are grown.

Every layer after the EBL was grown cold, at temperatures under 600 °C. The need for cold growth immediately after the EBL and p-layers, rather than after the InN active region, is to prevent magnesium from making it to the active region. Because of the
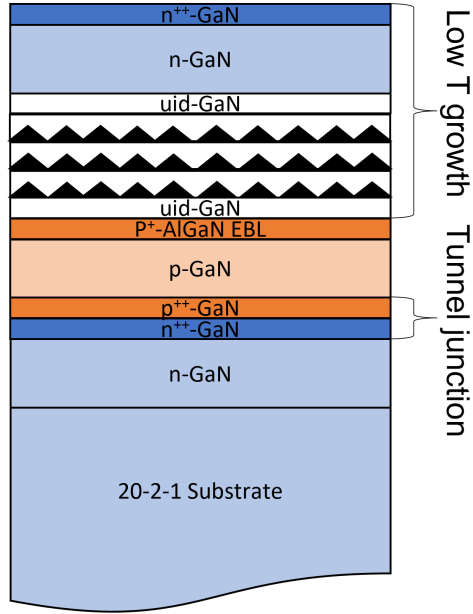
n^{++}-GaN

n-GaN

uid-GaN

uid-GaN

P$^+$-AlGaN EBL

p-GaN

p^{++}-GaN

n^{++}-GaN

n-GaN

20-2-1 Substrate

Low T growth   Tunnel junction

Figure 5.9: Schematic of proposed p-down InN LED

.

memory effect, magnesium continues to incorporate into the growth after the precursor

flow has been shut off. This effect can be greatly mitigated with a surface treatment to

remove surface-riding magnesium and regrowth or by reducing growth temperature.[22],

[23]

To illustrate this, several LEDs with the general p-down structure shown in figure

5.9 were grown with a couple modifications. In all devices, the InN active layers were

replaced with single 3.5 nm blue quantum wells grown at 880 °C. In the first sample, the

15 nm uid-GaN spacer between the EBL and the quantum well was grown by FME at

575 °C, and the 80 nm n-GaN and 20 nm n^{++}GaN top layers were grown continuously

at 575 °C. In the second sample, the 15 nm uid-GaN spacer between the EBL and the

quantum well was grown at 575 °C with FME but the n-GaN layers were grown hot, at
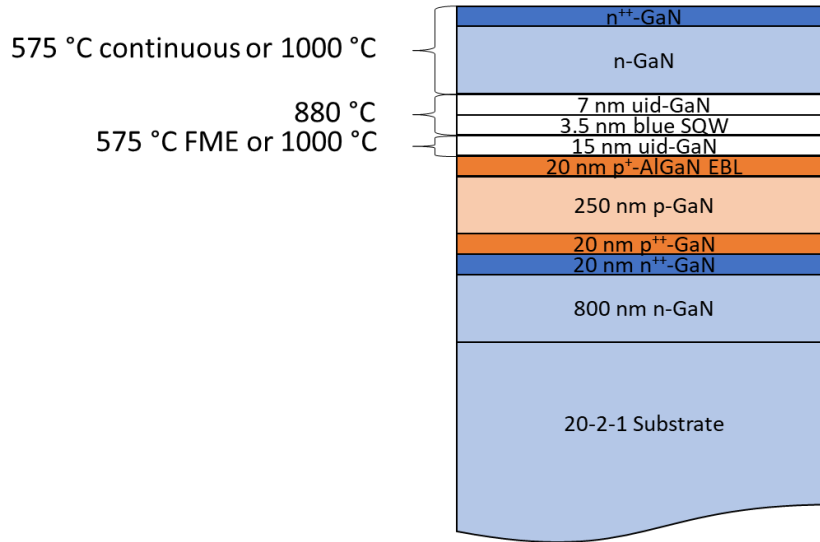
Figure 5.10: Schematic of blue p-down devices in p-side spacer and n-GaN growth temperature experiment

.

1000 °C. In the final sample, both the uid-GaN spacer and the n-GaN layers were grown hot at 1000 °C. The device structures are shown in figure 5.10.

LEDs were then fabricated from the three samples. The LEDs consisted of perforated 0.1 mm mesas etched by $SiCl_4$ RIE. The vias were 1.5 µm wide and spaced 3.5 µm apart in order to replicate the result by Li et al. for buried p-type activation.[24] In order to remove etch damage and allow for activation of the buried p-type from the vias and sidewalls, the samples were treated with 5 min UV-ozone, 5 min heated H_3PO_4 and 5 min buffered HF repeated three times. This surface treatment has been shown by Wong et al. to remove etch damage and allow for activation through the etched surface.[25] The buried p-layers were then activated at 700 °C for 30 min. IV curves were measured and optical micrographs of the LEDs were captured to show current spreading and relative intensity.
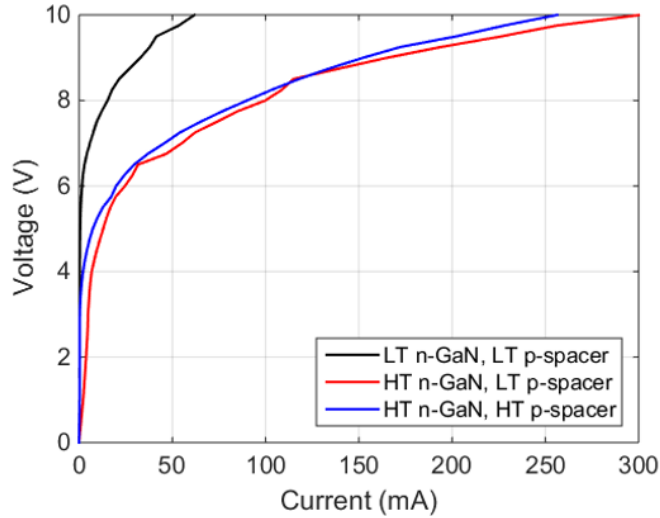
Figure 5.11: Current-voltage curves of three p-down blue LEDs: one grown with low temperature n-GaN and low temperature p-side spacer, one grown with high temperature n-GaN and low temperature p-side spacer, and one grown with high temperature n-GaN and high temperature p-side spacer

.

From the IV curves in 5.11, it is immediately clear that the low temperature n-GaN adds over a volt to the operating voltage. The voltage of the other two devices remains quite high, with typical blue device turn on in the 3 V range. The high voltage of the two devices with high temperature n-type layers is likely from a combination of the unoptimized buried tunnel junction and incomplete activation of the buried p-type layers.

Micrographs were taken with a 20x objective lens under $50\,A\,cm^{-2}$ operation and are shown in figure 5.12. Both samples with the low temperature p-side uid-GaN spacer are relatively bright with several mW output measured from the backside of the devices. The third sample, with the high temperature p-side uid-GaN spacer, was extremely dim and the camera exposure time had to be boosted by a factor of 100x to capture the emission.
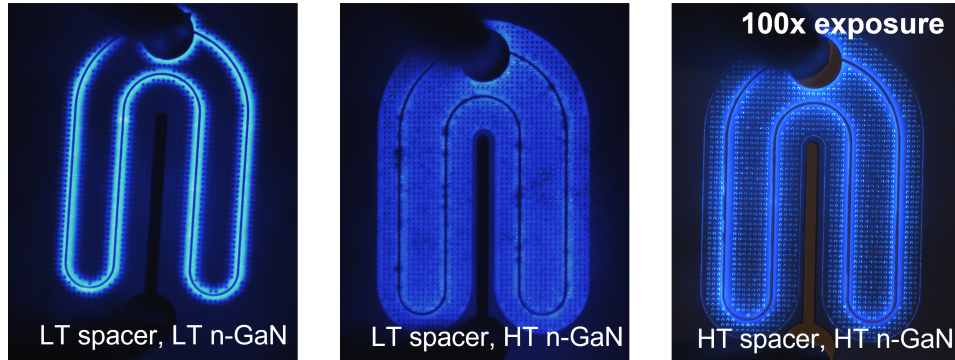
Figure 5.12: Micrographs of three p-down blue LEDs grown with various temperature conditions in the p-side uid spacer and n-GaN layers. Micrographs were taken with LEDs operating at $50\,\mathrm{A\,cm^{-2}}$

.

With the high temperature p-side GaN spacer, magnesium from the highly-doped EBL rides the surface and continue incorporating in the active region. Magnesium in the active region forms a non-radiative Shockley-Reed-Hall recombination center, reducing the blue emission intensity. With the cold growth of the p-side spacer, the memory effect is suppressed as shown by Agrawal et al., reducing the amount of magnesium that makes it to the active layers.[22], [23]

While it was bright, the sample with the low temperature n-GaN layers showed extremely poor current spreading and high voltage compared with the samples with n-GaN grown at $1000\,^{\circ}\mathrm{C}$. The poor current spreading and high voltage is a sign that the low temperature n-GaN layers have poor conductivity, likely due to compensating defects.

To investigate, a calibration sample with several n-GaN growth conditions was grown and secondary ion mass spectroscopy (SIMS) was used to evaluate the doping and contaminant concentrations. This sample consisted of three $50\,\mathrm{nm}$ n-GaN layers with different low temperature growth conditions separated by $180\,\mathrm{nm}$ of high temperature uid-GaN
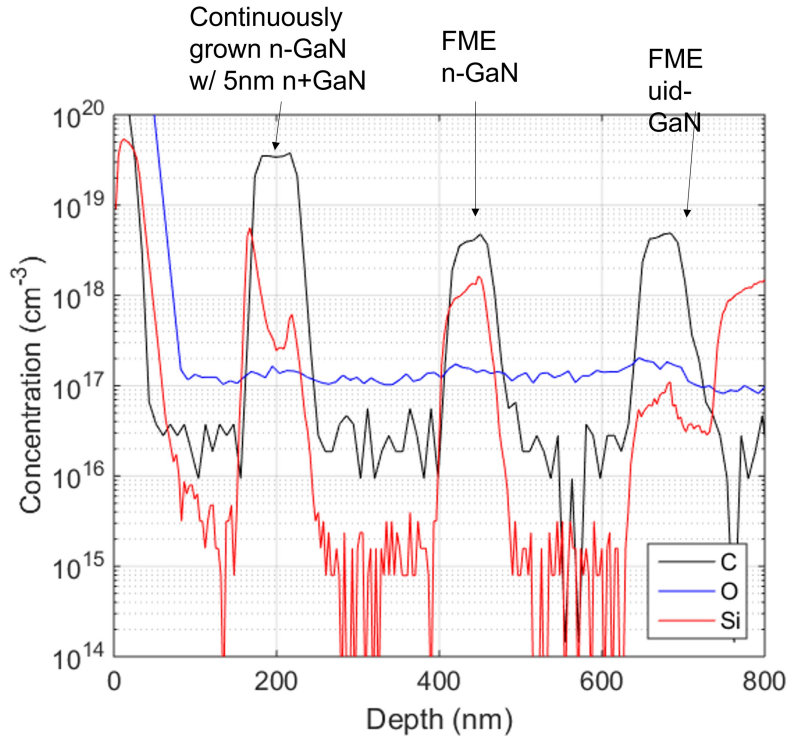
Figure 5.13: SIMS scans for silicon, oxygen and carbon in n-GaN layers grown at $575\,°C$
.

to smooth out the surface. The first layer was nominally uid-GaN grown at $575\,°C$ with an FME growth rate of $0.2\,Å$ per cycle. The second layer was the same but doped n-type with a disilane precursor flow of 0.2 sccm throughout the FME cycle. The final layer was consisted of $45\,nm$ of continuously grown n-GaN with a growth rate of $0.2\,Å\,s^{-1}$ capped with a $5\,nm$ n^{++} layer.

Figure 5.13 shows the result of this SIMS sample. The silicon doping was lower than expected, reaching into the 10^{18}s which can likely be solved by simply increasing the precursor flow. More concerning, the carbon concentration for the continuously grown layer was around $3 - 4 \times 10^{19}$ cm^{-3}, far higher than the silicon doping concentration. With this in mind, it is unsurprising that the p-down blue LED with n-GaN grown with

this condition showed such poor current spreading and voltage since the silicon doping was likely contributing very little to the layers' electrical properties.

As expected, the carbon concentration can be lowered by moving to a FME growth regime with slower growth rates and a lag time to allow for the group-III adatoms to migrate across the surface. However, the carbon concentration dropped only an order of magnitude and was still higher than the intentional doping. While the FME conditions used here were beneficial, either moving to even slower growth rates or hotter temperatures is required.

Finally, a p-down LED was grown with an InN active region on $(20\,\overline{2}\,\overline{1})$ bulk GaN. The layer structure is generally given in 5.9 and the active region consisted of 6x periods of 100 s of InN with 12 nm barriers grown by FME at 550 °C. Annealing to activate the buried p-layers presented an additional difficulty.

As shown in 5.14, annealing at a temperature of 600 °C showed degradation in the PL signal. The degradation in the PL intensity is indicative of thermal damage to the InN emitting layers. Typical activation conditions for surface p-GaN is 600-650 °C for 20 min. Activation of buried p-type layers is typically done at higher temperature and for longer, to allow the hydrogen to diffuse to the sidewalls and through any remaining surface damage. [25]
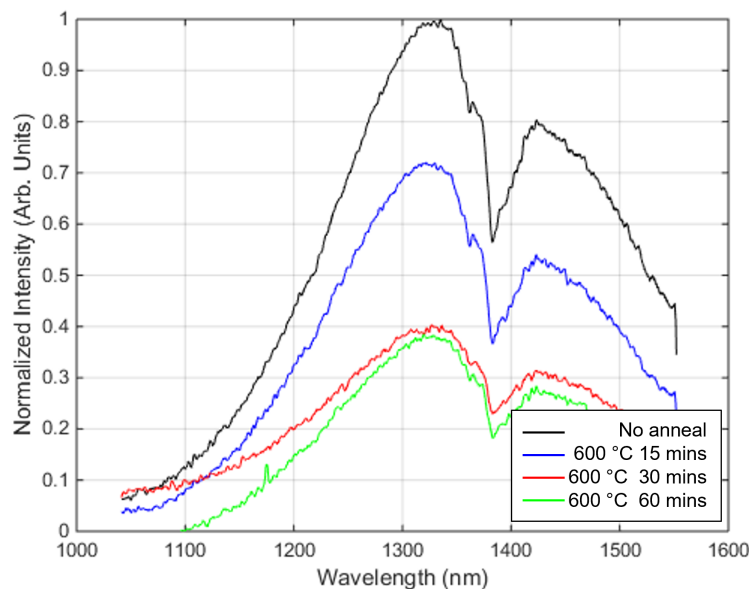
Figure 5.14: Room temperature photoluminescence spectra of p-down InN device after annealing at 600 °C for activation

.

5.6 Chapter Summary

In this chapter, we discussed InN and In-rich devices in literature. Growth of InN on a couple of semipolar crystal planes, $(20\,\overline{2}\,\overline{1})$ and $(20\,\overline{2}\,1)$, were explored. It was found that, at our presented growth conditions and template surface morphology, the InN nanostructures formed dashes on the $(20\,\overline{2}\,\overline{1})$ plane and dots on the $(20\,\overline{2}\,1)$ plane.

Efforts were made to progress towards an electrically injected InN-based device with a p-down structure. Several experimental LEDs with the proposed structure were grown and fabricated with a blue QW in place of the InN active layers. With these LEDs, the growth temperature of both the p-side uid-GaN spacer and n-GaN layers were determined to be critical.

Finally, a first attempt at a full electrically-injected InN LED was grown and fabricated. The activation anneal was additionally found to have a measureable effect on the InN layer PL intensity. The device was measured with a TEC-cooled InGaAs detector and lock-in amplifier but no emission was observed. While no infrared electroluminescence was seen, advancements were made towards a first electrically-injected InN-based emitter.

References

[1] J. Kim, H. Kim, and S. N. Lee, "Thermal degradation in InGaN quantum wells in violet and blue GaN-based laser diodes," *Curr. Appl. Phys.*, vol. 11, S167–S170, 2011. DOI: `10.1016/j.cap.2011.07.024`.

[2] D. Queren, M. Schillgalies, A. Avramescu, G. Brüderl, A. Laubsch, S. Lutgen, and U. Strauß, "Quality and thermal stability of thin InGaN films," *J. Cryst. Growth*, vol. 311, no. 10, pp. 2933–2936, 2009. DOI: `10.1016/j.jcrysgro.2009.01.066`.

[3] Z. Li, J. Liu, M. Feng, K. Zhou, S. Zhang, H. Wang, D. Li, L. Zhang, D. Zhao, D. Jiang, H. Wang, and H. Yang, "Suppression of thermal degradation of InGaN/GaN quantum wells in green laser diode structures during the epitaxial growth," *Appl. Phys. Lett.*, vol. 103, p. 152 109, 2013. DOI: `10.1063/1.4824850`.

[4] Y. T. Moon, D. J. Kim, K. M. Song, C. J. Choi, S. H. Han, T. Y. Seong, and S. J. Park, "Effects of thermal and hydrogen treatment on indium segregation in InGaN/GaN multiple quantum wells," *J. Appl. Phys.*, vol. 89, no. 11, pp. 6514–6518, 2001. DOI: `10.1063/1.1370368`.

[5] C. Lund, S. Nakamura, S. P. DenBaars, U. K. Mishra, and S. Keller, "Growth of high purity N-polar (In,Ga)N films," *J. Cryst. Growth*, vol. 464, pp. 127–131, 2017. DOI: `10.1016/j.jcrysgro.2016.11.039`.

[6] Y. Arakawa and H. Sakaki, "Multidimensional quantum well laser and temperature dependence of its threshold current," *Appl. Phys. Lett.*, vol. 40, no. 11, pp. 939–941, 1982. DOI: 10.1063/1.92959.

[7] M. Asada, Y. Miyamoto, and Y. Suematsu, "Gain and the Threshold of Three-Dimensional Quantum-Box Lasers," *IEEE J. Quantum Electron.*, vol. 22, no. 9, pp. 1915–1921, 1986. DOI: 10.1109/JQE.1986.1073149.

[8] J. G. Lozano, A. M. Sánchez, R. García, D. González, D. Araújo, S. Ruffenach, and O. Briot, "Nucleation of InN quantum dots on GaN by metalorganic vapor phase epitaxy," *Appl. Phys. Lett.*, vol. 87, p. 263 104, 2005. DOI: 10.1063/1.2152110.

[9] C. Meissner, S. Ploch, M. Leyer, M. Pristovsek, and M. Kneissl, "Indium nitride quantum dot growth modes in metalorganic vapour phase epitaxy," *J. Cryst. Growth*, vol. 310, no. 23, pp. 4959–4962, 2008. DOI: 10.1016/j.jcrysgro.2008. 07.066.

[10] N. U. H. Alvi, P. E. Rodriguez, V. J. Gómez, P. Kumar, M. Willander, and R. Nötzel, "Highly sensitive and fast anion-selective InN quantum dot electrochemical sensors," *Appl. Phys. Express*, vol. 6, p. 115 201, 2013. DOI: 10.7567/APEX.6. 115201.

[11] S. Ruffenach, B. Maleyre, O. Briot, and B. Gil, "Growth of InN quantum dots by MOVPE," *Phys. Status Solidi C*, vol. 2, no. 2, pp. 826–832, 2005. DOI: 10.1002/ pssc.200460319.

[12]   C. S. Ku, W. C. Chou, and M. C. Lee, "Optical investigations of InN nanodots capped by GaN at different temperatures," *Appl. Phys. Lett.*, vol. 90, p. 132 116, 2007. DOI: 10.1063/1.2716347.

[13]   A. Yoshikawa, N. Hashimoto, N. Kikukawa, S. B. Che, and Y. Ishitani, "Growth of InN quantum dots on N-polarity GaN by molecular-beam epitaxy," *Appl. Phys. Lett.*, vol. 86, p. 153 115, 2005. DOI: 10.1063/1.1900948.

[14]   C. Lund, M. Catalano, L. Wang, C. Wurm, T. Mates, M. Kim, S. Nakamura, S. P. DenBaars, U. K. Mishra, and S. Keller, "Metal-organic chemical vapor deposition of N-polar InN quantum dots and thin films on vicinal GaN," *J. Appl. Phys.*, vol. 123, p. 055 702, 2018. DOI: 10.1063/1.5009904.

[15]   C. E. Reilly, S. Nakamura, S. P. DenBaars, and S. Keller, "MOCVD Growth and Characterization of InN Quantum Dots," *Phys. Status Solidi B*, vol. 257, p. 1 900 508, 2019. DOI: 10.1002/pssb.201900508.

[16]   C. E. Reilly, C. Lund, S. Nakamura, U. K. Mishra, S. P. Denbaars, and S. Keller, "Infrared luminescence from N-polar InN quantum dots and thin films grown by metal organic chemical vapor deposition," *Appl. Phys. Lett.*, vol. 114, p. 241 103, 2019. DOI: 10.1063/1.5109734.

[17]   Z. Bi, M. Ek, T. Stankevic, J. Colvin, M. Hjort, D. Lindgren, F. Lenrick, J. Johansson, L. R. Wallenberg, R. Timm, R. Feidenhans'L, A. Mikkelsen, M. T. Borgström, A. Gustafsson, B. J. Ohlsson, B. Monemar, and L. Samuelson, "Self-assembled InN

quantum dots on side facets of GaN nanowires," *J. Appl. Phys.*, vol. 123, p. 164 302, 2018. DOI: 10.1063/1.5022756.

[18] C. E. Reilly, B. Bonef, S. Nakamura, J. S. Speck, S. P. Denbaars, and S. Keller, "Characterization of InGaN quantum dots grown by metalorganic chemical vapor deposition," *Semicond. Sci. Technol.*, vol. 34, p. 125 002, 2019. DOI: 10.1088/1361-6641/ab4b93.

[19] A. Das, G. P. Dimitrakopulos, Y. Kotsar, A. Lotsari, T. Kehagias, P. Komninou, and E. Monroy, "Improved luminescence and thermal stability of semipolar (11-22) InGaN quantum dots," *Appl. Phys. Lett.*, vol. 98, p. 201 911, 2011. DOI: 10.1063/1.3588335.

[20] J. T. Griffiths, T. Zhu, F. Oehler, R. M. Emery, W. Y. Fu, B. P. Reid, R. A. Taylor, M. J. Kappers, C. J. Humphreys, and R. A. Oliver, "Growth of non-polar (11-20) InGaN quantum dots by metal organic vapour phase epitaxy using a two temperature method," *APL Mater.*, vol. 2, p. 126 101, 2014. DOI: 10.1063/1.4904068.

[21] P. Chan, C. E. Reilly, S. Keller, S. P. DenBaars, and S. Nakamura, "Growth by MOCVD and photoluminescence of semipolar (20-2-1) InN quantum dashes," *J. Cryst. Growth*, vol. 563, p. 126 093, 2021. DOI: 10.1016/j.jcrysgro.2021.126093.

[22] A. Agarwal, M. Tahhan, T. Mates, S. Keller, and U. Mishra, "Suppression of Mg propagation into subsequent layers grown by MOCVD," *J. Appl. Phys.*, vol. 121, no. 2, 2017. DOI: 10.1063/1.4972031.

[23] A. Agarwal, C. Gupta, A. Alhassan, T. Mates, S. Keller, and U. Mishra, "Abrupt GaN/p-GaN:Mg junctions grown via metalorganic chemical vapor deposition," *Appl. Phys. Express*, vol. 10, no. 11, 2017. DOI: 10.7567/APEX.10.111002.

[24] P. Li, H. Zhang, H. Li, M. Iza, Y. Yao, M. S. Wong, N. Palmquist, J. S. Speck, S. Nakamura, and S. P. DenBaars, "Size-independent low voltage of InGaN micro-light-emitting diodes with epitaxial tunnel junctions using selective area growth by metalorganic chemical vapor deposition," *Opt. Express*, vol. 28, no. 13, p. 18 707, 2020. DOI: 10.1364/oe.394664.

[25] M. S. Wong, J. Back, D. Hwang, C. Lee, J. Wang, S. Gandrothula, T. Margalith, J. S. Speck, S. Nakamura, and S. P. Denbaars, "Demonstration of high wall-plug efficiency III-nitride micro-light-emitting diodes with MOCVD-grown tunnel junction contacts using chemical treatments," *Appl. Phys. Express*, vol. 14, no. 8, 2021. DOI: 10.35848/1882-0786/ac1230.

Chapter 6

Summary and future work

In chapters 1 and 2, we introduced the III-nitride material system as well as motivated
and explored literature on relaxed InGaN buffer layers. We then demonstrate a novel
method to relax an InGaN buffer over a full substrate by decomposing a high composition
InGaN underlayer in chapter 3. Using this method, we show a 85% relaxed $In_{0.04}Ga_{0.96}N$
buffer layer and a 75 nm red-shift in PL of quantum wells grown on it as compared to
a reference GaN template. We further show morphological improvements to the buffer
layers to achieve smooth, relaxed InGaN buffers.

In chapter 4, we focus on red LEDs grown on these buffer layers. We show red-
shifting of an LED on a relaxed buffer by 140 nm as compared to a co-loaded LED
without a decomposition layer. Finally, red micro-LEDs are fabricated with 0.46% peak
EQE measured on-wafer at a peak emission wavelength of 643 nm.

Lastly, in chapter 5, progress is shown towards an InN-based near-infrared emit-

ter. MOCVD growth of semipolar InN quantum dots is explored and a p-down device structure is proposed. While PL was seen from the complete device structure, no EL was measured. The key challenges are identified as the InN temperature sensitivity and subsequent cold growth temperatures leading to poor crystal quality and high impurity incorporation on the n-side.

6.1 Potential LED improvement paths

All the red LEDs presented thus far have had simple InGaN/GaN active regions grown at a single temperature. In long-wavelength InGaN devices, the use of AlGaN in the active region has proven beneficial. AlGaN layers help to suppress phase separation of the high composition InGaN QWs, narrowing FWHM and reducing carrier loss to undesired secondary emission peaks.[1] Additionally, red QWs are under high compressive strain even when grown coherent to a relaxed 7% InGaN buffer as previously shown. AlGaN layers may help to compensate the compressive strain in the InGaN QWs.[2]

The following experiments were carried out in the green wavelengths between 500 and 550 nm. This was to achieve more stable growths and because these active region improvements were carried out with the goal of achieving a partially-relaxed green laser diode. The growths therefore included waveguiding and cladding structures on both the n- and p-side as well as thick GaN DSL layers to prevent the optical mode from overlapping with the largely metallic DL.

On top of a 5 µm n-GaN template on PSS sapphire, an additional 2.5 µm of n-GaN

was grown. The 2.5 nm DL was grown at 720 °C and capped with 6 nm of uid-GaN between 720 and 1000 °C. Next, 1 μm of n-GaN was grown at 1100 °C in hydrogen as discussed in section 3.2. The InGaN buffer was fully relaxed and consisted of 20 periods of 5/5 nm InGaN/GaN grown at 930 °C corresponding with roughly $In_{0.03}Ga_{0.97}N$ average composition.

The n-SCH was 3 periods of 16/4 nm of InGaN/GaN grown at 880 °C averaging around $In_{0.12}Ga_{0.88}N$. This layer was grown with hot GaN interlayers as discussed in section 3.2 to maintain smooth surface morphology. The active region consisted of 4 periods of 2.5 nm InGaN QWs grown at 830 °C and 11 nm barriers at various conditions. A 10 nm p-AlGaN EBL was included along with a symmetric p-SCH InGaN/GaN superlattice. Finally, 150 nm p-GaN was grown and capped with a 15 nm p^{++}-GaN contact layer.

The first comparison was between growing the GaN quantum barriers at the QW temperature of 830 °C or at a higher temperature of 920 °C. In the case of the hot barrier, 2 nm of GaN was first grown at 830 °C to cap the InGaN QW before ramping the temperature up to 930 °C to grow the remaining 9 nm.

As shown in figure 6.1, the light output power is significantly increased with the use of hot barriers, at least in green laser diode structures grown on relaxed InGaN buffers. The voltage increase is concerning, but these devices were tested using a "Quicktest" technique with manually placed indium contacts which can lead to inconsistent or high voltage.

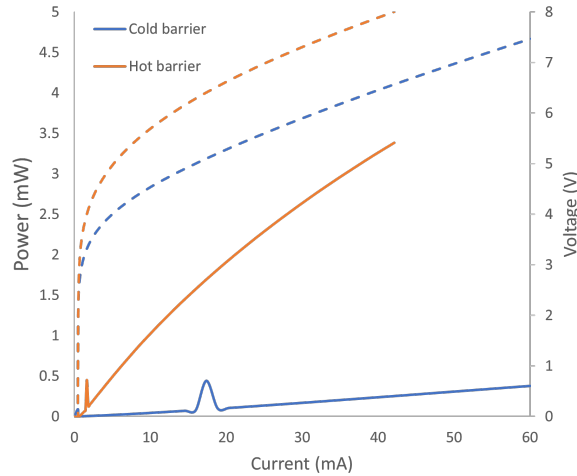The next variation included an AlGaN capping layer instead of a GaN capping layer

105

Figure 6.1: Light-current-voltage comparison of a green LD structure with barriers grown at $830\,°\text{C}$ and $920\,°\text{C}$.

in the active region. These two samples were grown in a separate growth campaign. In this case, both active regions consisted of $2.5\,\text{nm}$ InGaN quantum wells grown at $830\,°\text{C}$ and capped with $2\,\text{nm}$ of material. In one device, the capping layer was about $\text{Al}_{0.12}\text{Ga}_{0.88}\text{N}$ and in the other it was GaN. The temperature was ramped up to $920\,°\text{C}$ and an additional $9\,\text{nm}$ of GaN barrier was grown.

Results are shown in figure 6.2. Clearly, the light output power has again increased. While the emission peak blue-shifted by $15\,\text{nm}$, the FWHM tightened from about $45\,\text{nm}$ to $30\,\text{nm}$ with the inclusion of AlGaN caps.

The results are far from conclusive and continued optimization is needed to balance defects and relaxation benefit in green. Careful optimization and inclusion of improvements such as these into the previously shown red micro-LED structure could yield even better device performance.
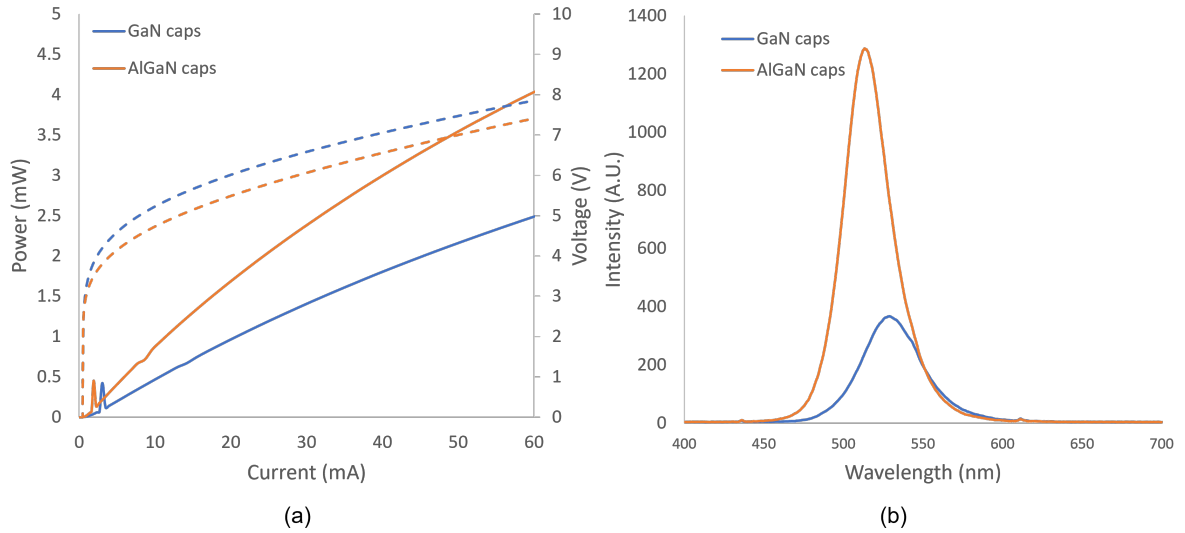
106

Figure 6.2: Light-current-voltage comparison of a green LD structure with and without AlGaN capping layers.

6.2 Conclusion

I will leave the reader, once again, with the summary table of recent red LED reports. As shown in table 6.1, our report stacks up favorably with other relaxed InGaN methods. However, red LEDs on relaxed InGaN as a whole are lagging conventionally grown red LEDs significantly. In this chapter, we have suggested a couple paths towards improving the red LEDs reported here by optimizing active region design and including AlGaN capping layers and high temperature GaN barriers. Additionally, the buffer and decomposition layer need to be carefully optimized for the complex trade-off between increased dislocation density leading to leakage and non-radiative recombination, increased v-pits leading to better hole injection and lower voltage, and decreased strain in the active region leading to higher indium uptake.

Authors	Report	λ (nm)	Peak EQE (%)	Device size (µm²)	V_F at 50 A cm⁻²	Relaxed InGaN	a (Å)
Chan et al.	–	643	0.46 (W)	5×5	4.1	Yes*	3.211
Chan et al.	–	643	0.31 (W)	10×10	3.0	Yes*	3.211
Wong et al.	2022[3]	637	0.25 (P)	20×20	2.2	Yes*	3.211
Chan et al.	2021[4]	633	0.05 (W)	10^5	2.6	Yes*	3.213
Pasayat et al.	2021[5]	632	0.2 (W)	6×6	3.5	Yes†	3.197
White et al.	2021[6]	610	0.83 (P)	80×80	3.8	Yes‡	3.205
Dussaigne et al.	2021[7]	625	0.14 (W)	25π	6.8	Yes‡	3.205
Dussaigne et al.	2020[8]	616	0.09 (W)	50×50	–	Yes‡	3.207
Li et al.	2022[9]	620	4.5 (P)	60×60	5.0	No	3.189
Li et al.	2021[10]	611	2.6 (P)	20×20	3.9	No	3.189
Iida et al.	2020[11]	665	0.19 (P)	650×250	3.0	No	3.189
Hwang et al.	2014[1]	629	2.9 (P)	460×460	5.0	No	3.189

(W) EQE measured on wafer

(P) EQE measured from packaged LED

* Buffer relaxed using decomposition layer

† Buffer relaxed using a nanoporous layer

‡ Device grown on Soitec InGaNOS substrate

Table 6.1: Reports presented here and other recent reports of red InGaN-based LEDs.

References

[1] J. I. Hwang, R. Hashimoto, S. Saito, and S. Nunoue, "Development of InGaN-based red LED grown on (0001) polar surface," *Appl. Phys. Express*, vol. 7, no. 7, pp. 1–4, 2014. DOI: `10.7567/APEX.7.071003`.

[2] A. I. Alhassan, R. M. Farrell, B. Saifaddin, A. Mughal, F. Wu, S. P. DenBaars, S. Nakamura, and J. S. Speck, "High luminous efficacy green light-emitting diodes with AlGaN cap layer," *Opt. Express*, vol. 24, no. 16, p. 17 868, 2016. DOI: `10.1364/oe.24.017868`.

[3] M. S. Wong, P. Chan, N. Lim, H. Zhang, R. C. White, J. S. Speck, S. P. Denbaars, and S. Nakamura, "Low Forward Voltage III-Nitride Red Micro-Light-Emitting Decomposition Layer," *Crystals*, pp. 4–9, 2022.

[4] P. Chan, V. Rienzi, N. Lim, H. M. Chang, M. Gordon, S. P. DenBaars, and S. Nakamura, "Demonstration of relaxed InGaN-based red LEDs grown with high active region temperature," *Appl. Phys. Express*, vol. 14, no. 10, pp. 3–7, 2021. DOI: `10.35848/1882-0786/ac251d`.

[5] S. S. Pasayat, C. Gupta, M. S. Wong, R. Ley, M. J. Gordon, S. P. Denbaars, S. Nakamura, S. Keller, and U. K. Mishra, "Demonstration of ultra-small (<10 μm) 632 nm red InGaN micro-LEDs with useful on-wafer external quantum efficiency (>0.2%) for mini-displays," *Appl. Phys. Express*, vol. 14, no. 1, p. 011 004, 2021. DOI: `10.35848/1882-0786/abd06f`.

[6] R. C. White, H. Li, M. Khoury, C. Lynsky, M. Iza, S. Keller, D. Sotta, S. Nakamura, and S. P. DenBaars, "Ingan-based microled devices approaching 1% eqe with red 609 nm electroluminescence on semi-relaxed substrates," *Crystals*, vol. 11, no. 11, 2021. DOI: `10.3390/cryst11111364`.

[7] A. Dussaigne, P. Le Maitre, H. Haas, J. C. Pillet, F. Barbier, A. Grenier, N. Michit, A. Jannaud, R. Templier, D. Vaufrey, F. Rol, O. Ledoux, and D. Sotta, "Full InGaN red (625 nm) micro-LED (10 μm) demonstration on a relaxed pseudo-substrate," *Appl. Phys. Express*, vol. 14, no. 9, 2021. DOI: `10.35848/1882-0786/ac1b3e`.

[8] A. Dussaigne, F. Barbier, B. Damilano, S. Chenot, A. Grenier, A. M. Papon, B. Samuel, B. Ben Bakir, D. Vaufrey, J. C. Pillet, A. Gasse, O. Ledoux, M. Rozhavskaya, and D. Sotta, "Full ingan red light emitting diodes," *J. Appl. Phys.*, vol. 128, no. 13, p. 135 704, 2020. DOI: `10.1063/5.0016217`.

[9] P. Li, H. Li, H. Zhang, Y. Yang, M. S. Wong, C. Lynsky, M. Iza, M. J. Gordon, J. S. Speck, S. Nakamura, and S. P. DenBaars, " Red InGaN micro-light-emitting diodes (>620 nm) with a peak external quantum efficiency of 4.5% using an epitaxial tunnel junction contact," *Appl. Phys. Lett.*, vol. 120, no. 12, p. 121 102, 2022. DOI: `10.1063/5.0086912`.

[10] P. Li, H. Li, H. Zhang, C. Lynsky, M. Iza, J. S. Speck, S. Nakamura, and S. P. Denbaars, "Size-independent peak external quantum efficiency (¿2%) of InGaN red micro-light-emitting diodes with an emission wavelength over 600 nm," *Appl. Phys. Lett.*, vol. 119, no. 8, 2021. DOI: `10.1063/5.0061940`.

[11] D. Iida, Z. Zhuang, P. Kirilenko, M. Velazquez-Rizo, and K. Ohkawa, "Demonstration of low forward voltage InGaN-based red LEDs," *Appl. Phys. Express*, vol. 13, no. 3, p. 031 001, 2020. DOI: 10.35848/1882-0786/ab7168.

Appendix A

Other applications for relaxed InGaN buffers with a decomposition layer

So far, we have discussed red LEDs as the main application for buffers relaxed with a decomposition layer. We have shown red micro-LEDs on these relaxed buffers with competitive performance compared to other relaxed InGaN methods. However, there are a couple other applications left unexplored in the main text.

A.1 Color tuneable micro LEDs

The main application for strain-relaxed InGaN buffers is for long wavelength devices. However, noticing the large red-shift of LEDs on the relaxed buffer layers opens up
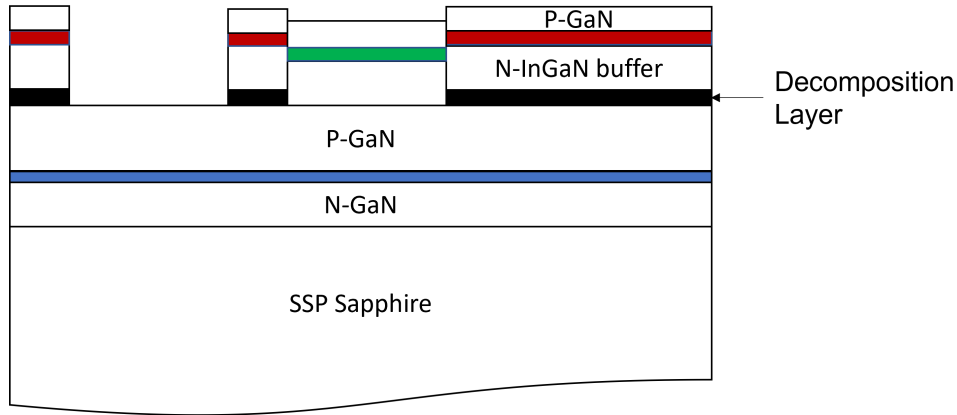
Figure A.1: Epitaxial structure of the monolithically integrated RGB devices.

applications for color-tuning LEDs by selectively patterning the decomposition layer. Similar to how LED color is tuned in nanopillar devices using strain of the active region,[1] we can tune the color of quantum wells grown at the same time by modifying their strain state, and thus indium uptake, during growth.

Figure A.1 shows the structure of the device incorporating integrated RGB devices. First, a blue LED was grown consisting of n-GaN, 8x MQW, p-AlGaN EBL and p-GaN layers grown on a SSP sapphire substrate. The starting blue epilayers were taken directly from our stock of blue LEDs grown after reactor maintenance to recover reactor performance. The DL was then selectively grown at $750\,°C$ with a $200\,nm$ DSL grown at $1000\,°C$. This growth was masked by $200\,nm$ of PECVD deposited SiO_2 patterned with a buffered HF wet etch. Finally, a $200\,nm$ n-InGaN buffer, 8x MQW and $50\,nm$ of p-GaN was selectively grown with a similarly deposited and patterned $200\,nm$ SiO_2 mask. Between each growth, the surface was treated with a $5\,min$ UV-ozone exposure and a $5\,min$ HCl dip.
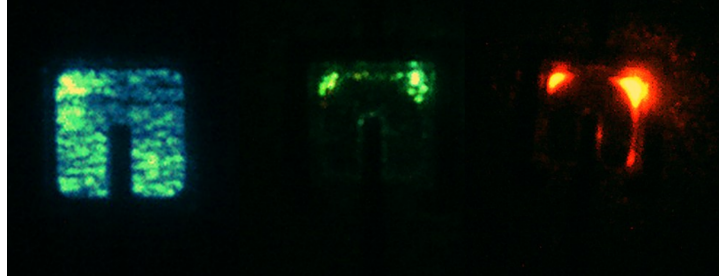
Figure A.2: Integrated red, green and blue 5×5 µm^2 LEDs in operation.

All three devices were processed at once. The structures for the blue, green and red had varying thicknesses of the n- and p-layers, which made the processed devices perform very poorly. Additionally, using reactor recovery epitaxy grown on SSP sapphire led to poor blue LED performance.

Three 10×10 µm^2 devices in operation at a nominal $20\,\text{A cm}^{-2}$ are shown in figure A.2. The green and red devices show poor n-side current spreading and light up only at the edges of the mesas. The blue LED shows non-uniform emission.

This was a proof of concept using poor-quality blue epitaxy and co-processing all LEDs, despite their different structures. The three LEDs have emission wavelengths falling in the blue, green and red ranges, roughly $450\,\text{nm}$, $530\,\text{nm}$ and $620\,\text{nm}$ respectively. The green and red LEDs were co-loaded for growth over a selectively-grown InGaN DL. In a second attempt, more care must be taken to match the epitaxy such that the mesa etch can be performed on all three devices at once with good results.

A.2 Far-red LEDs

Far-red LEDs have applications in horticulture. LEDs in the 700-800 nm range have been shown to affect plant photosynthesis, specifically stimulating growth and influencing flowering.[2], [3] Because of this, far-red LEDs are often included in artificial lighting for indoor horticulture.

As demonstrated, long wavelength active regions can be grown exceptionally hot by grown on relaxed template created by including a decomposition layer. In Chapter 4, a 630 nm LED was grown with the active region portion of the structure co-loaded with a reference showing electroluminescence under 500 nm.

The emission wavelength may be tuned well beyond 630 nm while maintaining relatively high growth temperatures throughout the structure. By increasing the composition or thickness of the InGaN buffer layers, the wavelength of the LED red shifts.

An LED was grown with a similar structure to that described previously in figure 4.1. The InGaN DL and InGaN/GaN DSL layers remained the same. The InGaN buffer layer was decreased slightly in composition and grown at 920 °C but increased significantly in thickness to 27 periods of 20/2 nm InGaN/GaN. The active region was 6x 2.5/6 nm InGaN/GaN MQW grown at 820 °C.

The resulting LED was tested on-wafer using a "quicktest" technique where indium is pressed onto the surface to form a p-contact and soldered onto a scribe-mark to form an n-contact.

The LIV and spectrum of the LED is plotted in figure A.3. The power is low and
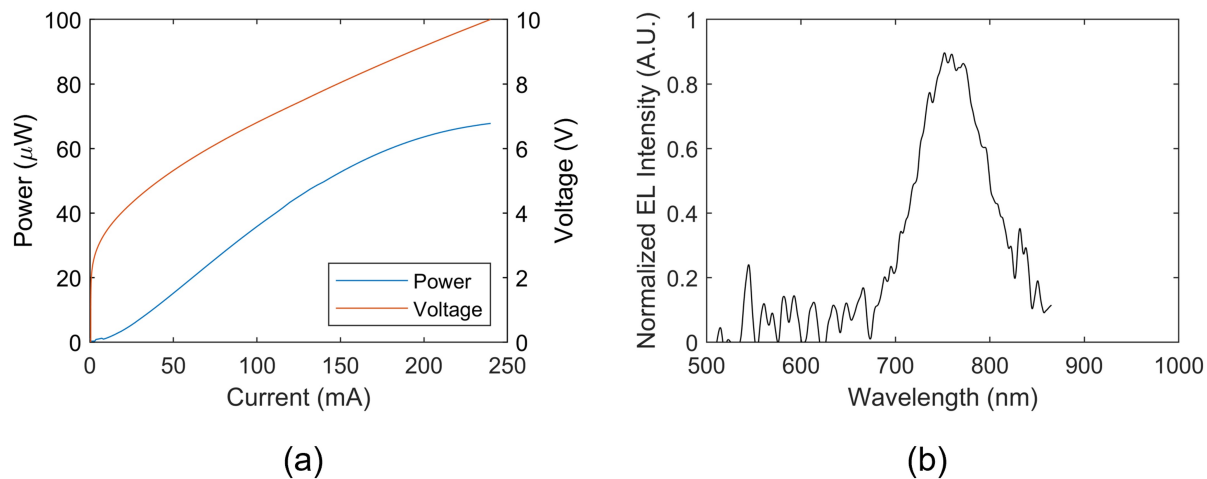
(a)   (b)

Figure A.3: Light-current-voltage curve (a) and spectrum (b) of far-red LED on relaxed InGaN buffer.

increases sub-linearly. The voltage is somewhat high for the wavelength, but is influenced greatly by the In-dot and solder placement. The peak wavelength at $20\,\mathrm{A\,cm^{-2}}$ is $760\,\mathrm{nm}$, one of the longest InGaN-based LEDs reported to-date.

The presented LED was a first attempt at far-red and needs significant optimization of the layers, particularly the DL, buffer and active region. However, it is promising that a first attempt of simply increasing the buffer thickness and lowering the active region temperature showed measurable emission in that wavelength regime.

References

[1]   K. Kishino, N. Sakakibara, K. Narita, and T. Oto, "Two-dimensional multicolor (RGBY) integrated nanocolumn micro-LEDs as a fundamental technology of micro-

LED display," *Appl. Phys. Express*, vol. 13, no. 1, p. 014 003, 2019. DOI: `10.7567/1882-0786/ab5ad3`.

[2] C. Fankhauser, "The Phytochromes, a Family of Red/Far-red Absorbing Photoreceptors," *J. Biol. Chem.*, vol. 276, no. 15, pp. 11 453–11 456, 2001. DOI: `10.1074/jbc.R100006200`.

[3] R. Legendre and M. W. van Iersel, "Supplemental far-red light stimulates lettuce growth: Disentangling morphological and physiological effects," *Plants*, vol. 10, no. 1, pp. 1–21, 2021. DOI: `10.3390/plants10010166`.